NORTHWESTERN UNIVERSITY

Reduced-order Homogenization of Heterogeneous Material Systems: from Viscoelasticity to Nonlinear Elasto-plastic Softening Material

A DISSERTATION

SUBMITTED TO THE GRADUATE SCHOOL
IN PARTIAL FULFILLMENT OF THE REQUIREMENTS

for the degree

DOCTOR OF PHILOSOPHY

Field of Theoretical and Applied Mechanics

By

Zeliang Liu

EVANSTON, ILLINOIS

December 2017

ABSTRACT

Reduced-order Homogenization of Heterogeneous Material Systems: from Viscoelasticity to Nonlinear Elasto-plastic Softening Material

Zeliang Liu

The discovery of efficient and accurate descriptions for the macroscopic constitutive behavior of heterogeneous materials with complex microstructure remains an outstanding challenge in mechanics. On the one hand, great accuracy can be achieved by modeling small domains of a material including all the details in the microstructure, however, at the expense of a large computational cost. On the other hand, efficient descriptions of the macroscopic material behavior can be obtained by empirical constitutive laws, at the expense of a tedious calibration process and limited accuracy. The challenge is in finding an optimal balance between preserving enough small-scale detail and keeping the computational expense low, without the need for empirically calibrated models. Based on the Lippmann-Schwinger integral equation, two novel reduced-order homogenization methods have been developed in this dissertation.

An analytical reduced-order micromechanics method is first proposed for linear elastic and viscoelastic heterogeneous material with overlapping geometries. Weighted-mean and additive overlapping conditions are introduced to consider various physical phenomena in the overlapping regions. The corresponding inclusion-wise strain definitions and integral equations under these two overlapping conditions are also derived. Using a Boolean-Poisson model and micromechanics mean-field theory, this analytical homogenization method is applied to a viscoelastic polymer nanocomposite with interphase regions and

estimates the properties and thickness of the interphase region based on experimental data for carbon-black filled styrene butadiene rubbers.

To consider complex microstructural morphologies and nonlinear history-dependent material behavior, a data-driven reduced-order homogenization method called self-consistent clustering analysis (SCA) is developed. Based on data clustering algorithm in the offline/training stage and self-consistent schemes for solving the Lippmann-Schwinger equation in the online/predicting stage, SCA provides an effective way of developing a microstructural database, which enables an efficient and accurate prediction of nonlinear material properties. Other than generic von Mises elasto-plastic material, it has been applied to 3-Dimensional polycrystal materials with crystal plasticity (CP). Through numerical validations, this data-driven method is believed to open new avenues in homogenization of irreversible processes and parameter-free concurrent multi-scale modeling of heterogeneous material systems.

To address the challenges in multiscale modeling of softening materials, a stable three-step homogenization scheme is further presented which removes the material instability issues in the microstructure, and the homogenized stress-strain responses of the representative volume element (RVE) are not sensitive to the RVE size. Combined with SCA, concurrent multiscale simulations with damage are performed. The predicted macroscale strain localization are observed to be sensitive to the combinations of microscale constituents, showing the capability of the microstructural database created by SCA. Finally, the concurrent framework enabled by the three-step scheme and SCA method is applied to a unidirectional (UD) fiber polymer matrix composite, and the predicted macroscale nonlinear anisotropic responses and crack patterns are validated against experiments.

Acknowledgements

Foremost, I want to thank my parents and my wife, Xinying. My accomplishment through this adventure is impossible without your sacrifices and unconditional love. I would also like to express my deepest gratitude to my PhD advisor, Professor Wing Kam Liu, for his invaluable guidance and considerable freedom afforded to me over the past years. My PhD research work really benefits from his profound insights in the areas of mechanics, numerical analysis and material science.

In additional to my advisor, I would like to thank my committee members: Professor Cate Brinson for her deep understanding in the mechanics of polymer nanocomposite; Professor Wei Chen for introducing me to engineering optimization; Professor Daniel Apley for sharing his expertise on data mining techniques. All of them have offered me great guidance and strong support. I am also indebted to Professors Gregory Wagner, Mark Flemming, Jian Cao, Horacio Espinosa, Shaoqiang Tang for all the discussions between us, which truly help to improve my work and broaden my thinking.

I would like to thank my colleagues and friends at Northwestern: Ying Li for introducing me to molecular dynamics and polymer viscoelasticity; John Moore for his inspiring lecture on micromechanics and working with me on the analytical reduced-order methods; Miguel Bessa for believing in my ideas and working with me on exploring data-driven approaches in mechanics; Ramin Bostanabad for sharing his knowledge on statistics and machine learning; Cheng Yu, Jiaying Gao and Modesar Shakoor for helping me extend the data-driven method to a broad range of applications; Gino Domel for proofreading the dissertation. I also owe my gratitude to Hongyu Chen, Wentao Yan, Jinhui Yan, Jia Zheng, Yanping Lian, Orion Kafka, Stephen Lin, Puikei Cheng and Ben Sonin.

I am grateful to all who have made my PhD life at Northwestern University an unforgettable journey.

Preface

This dissertation includes research work on the exploration of reduced-order material homogenization during the author's doctoral study. The following articles form the basis of the dissertation and will be appropriately referenced:

(1) Z. Liu, J. A. Moore, S. M. Aldousari, H. S. Hedia, S. A. Asiri, and W. K. Liu. A statistical descriptor based volume-integral micromechanics model of heterogeneous material with arbitrary inclusion shape. Computational Mechanics: 1-19, 2015.

(2) Z. Liu, J. A. Moore, and W. K. Liu. An extended micromechanics method for probing interphase properties in polymer nanocomposites. Journal of Mechanics and Physics of Solids 95: 663-680, 2016.

(3) Z. Liu, M. A. Bessa, and W. K. Liu. Self-consistent clustering analysis: an efficient multi-scale scheme for inelastic heterogeneous materials. Computer Methods in Applied Mechanics and Engineering 306: 319-341, 2016.

(4) Z. Liu, O. L. Kafka, C. Yu, and W. K. Liu. Data-driven self-consistent clustering analysis of heterogeneous materials with crystal plasticity. Advances in Computational Plasticity, 2017.

(5) Z. Liu, M. Fleming, W. K. Liu. Microstructural material database for self-consistent clustering analysis of elastoplastic strain softening materials. In preparation, 2017.

I dedicate this thesis to
my parents and my wife, Xinying,
for their constant support and unconditional love.
I love you all dearly.

Table of Contents

List of Tables

List of Figures

CHAPTER 1

Introduction

Materials are hierarchical in nature; hence, they involve an inter-play between simple small-scale constituents that together form elaborate compounds that can span multiple time- and length-scales. On the other hand, advanced manufacturing techniques, such as 3D printing [**49, 84, 85**], allow us to make hierarchically structured composites from nano- to macro-scale, which exhibit advantageous thermal, electrical or mechanical properties [**3, 102, 8, 120**]. This multi-scale nature of heterogeneous materials poses a continuing challenge in computational modeling of macroscopic structures. Ideally, efficient and accurate predictions of the macroscopic behavior of heterogeneous materials should be uniquely obtained from the material behavior of each separate constituent (material phase) and from the information about the material microstructure.

Traditional phenomenological constitutive relations [**44, 25, 16, 121**] characterize the average behaviors of the material, i.e. the contributions from all the material phases are not accounted for as an individual interaction of separate constituents. These laws regard materials as "black boxes", implying the need for burdensome experimental characterization and tedious calibration. In addition, they are problem-dependent and tend to fail when capturing highly localized microstructure-induced nonlinear material behavior, such as plasticity, damage and fatigue. Generalized continuum mechanics, also known as higher-gradient theories, have been proposed to incorporate the microscopic information by introducing higher order gradient of deformation [**40**]. The first known generation is micromorphic continuum developed by Toupin [**111**], Mindlin [**90**] and Eringen [**31**], and it is further generalized with arbitrary number of extra strain gradients by Liu and co-workers [**113, 114, 78, 109**]. A current challenge of high-gradient theories is the determination of the large number of coefficients associated with higher-order tensors [**112**].

The strain gradient is usually not directly informed by the microstructure, making the model phenomenological and requiring extra effort to calibrate those coefficients.

1.1. Homogenization of heterogeneous material systems

Concurrent multiscale [**35, 57, 34**] methods avoid the calibration process in the phenomenological models by directly establishing the connection between the microstructure and the macro-response of materials using the so-called homogenization method. In the homogenization process, these concurrent methods link every macroscopic point of a structure to a Representative Volume Element (RVE) [**2, 117**] of the microstructure, and the macroscopic response (e.g. stress) is obtained through averaging inside the RVE. For a material with random microstructure, its true macroscopic properties are obtained as converged values only if the size of the RVE becomes sufficiently large, or the RVE should be a statistically representative sample of the material.

First-order homogenization, which will be mainly used in this dissertation, can be defined by assuming scale-separation and vanishing external body force inside the RVE. Let us introduce $\mathcal{U}$ as the space of admissible microscopic displacements $\mathbf{u}$ inside an RVE domain Ω with boundary Γ. It can be proved that under classical first-order boundary conditions, such as displacement boundary conditions (DBC), traction boundary condition (TBC) and periodic boundary conditions (PBC), the following equation is satisfied,

$$\langle \boldsymbol{\sigma} \rangle_\Omega : \langle \delta\boldsymbol{\varepsilon} \rangle_\Omega = \langle \boldsymbol{\sigma} : \delta\boldsymbol{\varepsilon} \rangle_\Omega, \quad \forall \delta\mathbf{u} \in \mathcal{U} \tag{1.1}$$

where $\langle \square \rangle_\Omega$ is defined as volume average inside the RVE,

$$\langle \square \rangle_\Omega = \frac{1}{|\Omega|} \int_\Omega \square d\Omega \tag{1.2}$$

Eq. 1.1 is the so-called Hill-Mandel macro-homogeneity condition [**47, 48**], which is equivalent to the statement that the virtual work density on the macroscale equals that of the microscale. It also ensures that the homogenized strain and stress are admissible variables in the macroscale constitutive relation.

Direct Numerical Simulation (DNS) is the most accurate and flexible homogenization method for solving the RVE problem, e.g. Finite Element Method [**9**] and Fast Fourier

Transformation (FFT)-based micromechanics method [**93, 61**]. However, due to a large number of degrees of freedom, DNS can be very time-consuming. Since each integration point in a concurrent multiscale method is associated with an RVE problem (necessary for nonlinear material), the total computational cost of this approach is tremendous.

Strain softening also poses computational challenges at the microscopic levels for concurrent multiscale methods. Direct application of a material damage model in the microscale RVE results in unstable and non-physical results. To date, multiscale modeling coupled with material damage is still not well explored [**41**]. Most multiscale methods require an additional microscale material length parameter to regularize the ill-posed boundary value problem in the microscale RVE. However, the relationship between the macroscale and microscale length parameters is usually not physically justified, and it is arguable that the microscale RVE model does not provide any information on how to determine the macroscale material length parameter. Instead, it merely moves the continuum localization problem one scale down [**5**]. Even if the microscale RVE model is regularized by a length parameter without justifying its physical basis, the homogenization problem with the localization effect is still not well defined. In the strain-softening region, the overall homogenized stress-strain response strongly depends on the size of the RVE, which is contradictory to the definition of an RVE. These issues will be discussed in detail, and solutions will be proposed in Chapter 5.

1.2. Reduced-order homogenization methods

A myriad of homogenization methods have been developed with the goal of finding an appropriate balance between cost and accuracy; these are generally referred to as reduced-order methods. Analytical micromechanical methods [**32, 46, 48, 71**], the Voronoi cell finite element method [**42**], spectral methods [**1**], the generalized method of cells [**97**], the transformation field analysis (TFA) [**28**], the nonuniform transformation field analysis (NTFA) [**86**], and the principal component analysis [**55, 74, 53**] or proper orthogonal decomposition (POD) [**11, 126**] are some of the most successful methods of this kind.

Analytical micromechanics methods [**32, 46, 48, 23, 71**] can be classified as one kind of reduced-order homogenization method because they describe the heterogeneous material by several microstructural descriptors. Based on analytical solutions and mean-field assumptions, micromechanics methods are very efficient [**95**]. An extended micromechanics method for overlapping geometries will be introduced in Chapter 3, which allows us to consider interacting inclusions. Nevertheless, the applicability of analytical micromechanics method is still limited when considering complex microstructure and localized nonlinear material behavior such as plasticity and damage [**19**].

Data-driven homogenization methods have recently attracted lots of attention. Data mining, as an interdisciplinary subfield of computer science and statistics, forms the basis of data-driven methods [**75**]. By automatically or semi-automatically sifting through the raw data in the database, previously unknown regularities or patterns can be extracted and generalized to make accurate predictions [**122, 107**]. As a start, a raw dataset for learning is usually generated from a prior numerical simulations or informed by experiments. Depending on the type of the raw dataset, current data-driven methods can be mainly divided into the macroscopic approaches and microscopic approaches.

In macroscopic approaches, the input data are usually material properties of each individual constituent, loading conditions and statistical descriptors that represent the geometry of the microstructure, while the output data are macroscopic mechanical properties from DNS simulations. Xu et al. [**124**] used design of experiment (DOE) to identify the key microstructural descriptors. A similar approach has been applied to the design of magneto-elastic Fe-Ga alloy by Liu et al. [**68**]. For hyperelastic materials, tensor decomposition (e.g. parallel factor decomposition) and neural networks have been used to interpolate the macroscopic effective strain energy density [**127, 60, 12**]. However, the accuracy and smoothness of the prediction of macroscopic approaches is limited by a lack of microscopic information. For example, the localized plastic strain field cannot be well represented by its field average.

To address this problem, microscopic approaches collect data at each discretization point in the DNS. POD uses linear combinations of all input variables to define the

principal components (modes) to make the predictions for general load cases. This is a fundamental issue when describing nonlinear irreversible plastic processes that is only mitigated by using many snapshots in the offline stage which increases the computational cost of the online stage to unreasonable values [**126, 56**]. The NTFA introduced by Michel and Suquet [**86, 36**], approaches the problem differently with the aim of compressing the nonlinear plastic strain field. The idea behind NTFA is to leverage the capabilities of analytical micromechanical methods to define a set of reduced variables that are then subjected to "evolution equations" [**86, 39**]. Consequently, the computational cost of NTFA is low, but the inclusion of empirical laws that require further calibration is a limitation. Furthermore, the RVEs need to be subjected to irreversible deformation to obtain the plastic modes (as in POD) which leads to an extensive exploration of the deformation space at the offline stage.

A new data-driven approach will be proposed in Chapter 4, where the above-mentioned limitations are addressed simultaneously by meeting three fundamental goals: 1) avoiding an extensive exploratory offline stage; 2) eliminating the need for extra calibration of the constitutive laws; 3) achieving a reduction in computational time without significantly compromising accuracy.

1.3. Outline of the dissertation

This dissertation is outlined as follows. In Chapter 2, the Lippmann-Schwinger equation will be derived, which will serve as the basis for all the proposed reduced-order homogenization methods. In Chapter 3, a new micromechanics method for overlapping geometries will be introduced as an analytical reduced-order homogenization method, and it will be applied for inverse modeling of interphase properties in polymer nanocomposite. In Chapter 4, the data-driven homogenization method called self-consistent clustering analysis (SCA) will be proposed and validated for nonlinear elasto-plastic materials. Chapter 5 will focus on homogenization of strain softening material, and several examples of concurrent simulation with multiscale material damage will be demonstrated. In Chapters 6, two realistic nonlinear material systems will be investigated. Finally, in Chapter 7, conclusions are drawn, and future research directions are discussed.

CHAPTER 2

Lippmann-Schwinger Integral Equation

2.1. Background

Although originated from the quantum mechanics community [**67**], the Lippmann-Schwinger integral equation has been widely used in continuum mechanics for analyzing heterogeneous material systems. In 1970s, Kröner [**58**] had discussed the use of Lippmann-Schwinger equation for solving elastostatic mechanics problems. It has been also extended to consider multiple scattering problems in elastodynamics, while referred as volume integral equation method (VIEM) [**63, 62**]. As mentioned in Mura's book [**95**], the equivalent inclusion method, which introduces the concept of eigenstrain, is actually an alternative interpretation of the Lippmann-Schwinger integral equation. In 1957, Eshelby [**32**] first pointed out that when the eigenstrain inside an inclusion is chosen properly, the stress disturbance in an applied stress due to the presence of an inhomogeneity can be simulated by the inclusion with eigenstress. Based on Eshelby's solution, a myriad of micromechanics methods, such as Mcori-Tanaka method [**92**] and self-consistent method [**48**], were proposed to approximate the solution of the Lippmann-Schwinger equation. To solve the equation directly, Moulinec et al. [**93**] proposed a fast Fourier transformation(FFT)-based scheme to analyze an RVE problem based on Lippmann-Schwinger equation for small strain, which was later extended to finite strain by Lahellec et al [**87**]. Vondejc et al. [**116**] proposed a weak form formulation of the same RVE problem and proved the equivalence to the Lippmann-Schwinger equation. In their work [**24**], a conjugate gradient (CG) solver was also adopted to solve the integral equation directly. Unlike the FFT-based solver [**93**], its convergence is not sensitive to the choice of the reference material. In this chapter, the Lippmann-Schwinger integral equation will be derived from

the equilibrium condition based on the Green's function, and some important features of this integral equation will also be discussed.

2.2. Small-strain formulation

The Lippmann-Schwinger integral equation is first derived under a small-strain assumption. Generally, the equilibrium condition without body force in a material domain Ω can be written as

$$\frac{\partial \sigma_{ij}(\mathbf{x})}{\partial x_i} = 0 \quad \text{in } \Omega. \tag{2.1}$$

By introducing a homogeneous elastic reference material with stiffness $\mathbf{C}^0$, the real stress in the heterogeneous material can be divided into two parts,

$$\boldsymbol{\sigma}(\mathbf{x}) = \mathbf{C}^0 : \boldsymbol{\varepsilon}(\mathbf{x}) + \mathbf{p}(\mathbf{x}), \tag{2.2}$$

where $\mathbf{p}(\mathbf{x})$ is the so-called polarization stress, which denotes the difference between the real stress and the stress in the reference material under the same strain. By substituting Eq. (2.2) into (2.1), we obtain

$$C^0_{ijkl}\frac{\partial \varepsilon_{kl}(\mathbf{x})}{\partial x_i} = -\frac{\partial p_{ij}(\mathbf{x})}{\partial x_i} \quad \text{in } \Omega. \tag{2.3}$$

With the help of the Green's function $\boldsymbol{\Phi}^0(\mathbf{x}, \mathbf{x}')$ which represents the strain at $\mathbf{x}$ contributed by a concentrated external stress at $\mathbf{x}'$ in the reference material, the original equilibrium condition can be rewritten in an integral form if we regard the polarization stress as an external stress on the reference material [**46, 45**],

$$\boldsymbol{\varepsilon}(\mathbf{x}) + \int_\Omega \boldsymbol{\Phi}^0(\mathbf{x}, \mathbf{x}') : \mathbf{p}(\mathbf{x}')d\mathbf{x}' - \boldsymbol{\varepsilon}^0 = 0, \tag{2.4}$$

where $\boldsymbol{\varepsilon}^0$ is the far-field strain, which is homogeneous for a homogeneous reference material and controls the evolution of the strain $\boldsymbol{\varepsilon}(\mathbf{x})$. By substituting Eq. (2.2) into (2.4), we obtain the integral equation in terms of the local strain $\boldsymbol{\varepsilon}(\mathbf{x})$,

$$\boldsymbol{\varepsilon}(\mathbf{x}) + \int_\Omega \boldsymbol{\Phi}^0(\mathbf{x}, \mathbf{x}') : \left[\boldsymbol{\sigma}(\mathbf{x}') - \mathbf{C}^0 : \boldsymbol{\varepsilon}(\mathbf{x}')\right] d\mathbf{x}' - \boldsymbol{\varepsilon}^0 = 0. \tag{2.5}$$

For convenience, Eq. (2.5) can also be written in incremental form:

$$\Delta\boldsymbol{\varepsilon}(\mathbf{x}) + \int_{\Omega} \boldsymbol{\Phi}^0(\mathbf{x},\mathbf{x}') : \left[\Delta\boldsymbol{\sigma}(\mathbf{x}') - \mathbf{C}^0 : \Delta\boldsymbol{\varepsilon}(\mathbf{x}')\right] d\mathbf{x}' - \Delta\boldsymbol{\varepsilon}^0 = 0, \tag{2.6}$$

Integral equations (2.5) or (2.6) are also known as the Lippmann-Schwinger equation in the continuum mechanics community [**58**]. The integral equation based on a homogeneous reference material will serve as the basis for both the analytical method and semi-analytical data-driven method introduced in Chapter 3 and 4.

Moreover, it can be shown that the far field strain $\Delta\boldsymbol{\varepsilon}^0$ is equal to the homogenized strain in the RVE based on the properties of the Green's function. By averaging the incremental integral equation 2.5 in Ω, we have

$$\begin{aligned} &\frac{1}{|\ \Omega\ |}\int_{\Omega} \Delta\boldsymbol{\varepsilon}(\mathbf{x}) d\mathbf{x} \\ &+\frac{1}{|\ \Omega\ |}\int_{\Omega}\left[\int_{\Omega} \boldsymbol{\Phi}^0(\mathbf{x},\mathbf{x}') d\mathbf{x}\right] : \left[\Delta\boldsymbol{\sigma}(\mathbf{x}') - \mathbf{C}^0 : \Delta\boldsymbol{\varepsilon}(\mathbf{x}')\right] d\mathbf{x}' - \Delta\boldsymbol{\varepsilon}^0 = \mathbf{0}. \end{aligned} \tag{2.7}$$

Moreover, the integral of the Green's function vanishes in the spacial domain,

$$\int_{\Omega} \boldsymbol{\Phi}^0(\mathbf{x},\mathbf{x}') d\mathbf{x} = \mathbf{0}. \tag{2.8}$$

Substituting Eq. (2.8) into (2.7) gives

$$\Delta\boldsymbol{\varepsilon}^0 = \frac{1}{|\ \Omega\ |}\int_{\Omega} \Delta\boldsymbol{\varepsilon}(\mathbf{x}) d\mathbf{x}. \tag{2.9}$$

In order to solve $\Delta\boldsymbol{\varepsilon}(\mathbf{x})$ in the integral equation 2.6, constraints are needed from the macroscopic boundary conditions. Different types of constraints can be used: 1) macro-strain constraint

$$\frac{1}{|\ \Omega\ |}\int_{\Omega} \Delta\boldsymbol{\varepsilon}(\mathbf{x}) d\mathbf{x} = \Delta\boldsymbol{\varepsilon}_M \quad \text{or} \quad \Delta\boldsymbol{\varepsilon}^0 = \Delta\boldsymbol{\varepsilon}_M; \tag{2.10}$$

and 2) macro-stress constraint

$$\frac{1}{|\ \Omega\ |}\int_{\Omega} \boldsymbol{\sigma}(\mathbf{x}) d\mathbf{x} = \boldsymbol{\sigma}_M \tag{2.11}$$

For more general cases, mixed constraints can also be formulated [**70**]. Here the boundary conditions are applied as constraints on the volume averages of strain or stress inside the RVE. This is different from standard FE method where the boundary conditions constrain the displacement or force on the RVE boundaries.

In a more general sense, the reference material is not necessary to be homogeneous. The stiffness tensor of a heterogeneous reference material can be written as

$$\mathbf{C}^0 = \mathbf{C}^0(\mathbf{x}). \tag{2.12}$$

The derivation of the integral equation is the same as the one for a homogeneous reference material, except that the far-field strain $\Delta\boldsymbol{\varepsilon}^0$ also becomes inhomogeneous. The new Lippmann-Schwinger equation can be derived as

$$\Delta\boldsymbol{\varepsilon}(\mathbf{x}) + \int_\Omega \boldsymbol{\Phi}^0(\mathbf{x},\mathbf{x}') : \left[\Delta\boldsymbol{\sigma}(\mathbf{x}') - \mathbf{C}^0(\mathbf{x}) : \Delta\boldsymbol{\varepsilon}(\mathbf{x}')\right] d\mathbf{x}' - \Delta\boldsymbol{\varepsilon}^0(\mathbf{x}) = 0, \tag{2.13}$$

where $\boldsymbol{\Phi}^0(\mathbf{x},\mathbf{x}')$ is the Green's function of the heterogeneous elastic reference material. Details of determining the Green's function for both homogeneous and heterogeneous materials will be discussed in Section 2.3. By averaging the integral equation (2.13) and utilizing the property of the Green's function in Eq. (4.17), we have

$$\frac{1}{\mid \Omega \mid}\int_\Omega \Delta\boldsymbol{\varepsilon}(\mathbf{x})d\mathbf{x} = \frac{1}{\mid \Omega \mid}\int_\Omega \Delta\boldsymbol{\varepsilon}^0(\mathbf{x})d\mathbf{x} = \Delta\boldsymbol{\varepsilon}_M, \tag{2.14}$$

where $\Delta\boldsymbol{\varepsilon}_M$ is the macroscopic homogenized strain. One can further define a so-called strain concentration tensor $\mathbf{A}(\mathbf{x})$, which maps $\Delta\boldsymbol{\varepsilon}_M$ to $\Delta\boldsymbol{\varepsilon}^0(\mathbf{x})$ in the heterogeneous reference material:

$$\Delta\boldsymbol{\varepsilon}^0(\mathbf{x})d\mathbf{x} = \mathbf{A}(\mathbf{x}) : \Delta\boldsymbol{\varepsilon}_M. \tag{2.15}$$

Substituting Eq. (2.15) to 2.13 gives

$$\Delta\boldsymbol{\varepsilon}(\mathbf{x}) = \mathbf{A}(\mathbf{x}) : \Delta\boldsymbol{\varepsilon}_M - \int_\Omega \boldsymbol{\Phi}^0(\mathbf{x},\mathbf{x}') : \left[\Delta\boldsymbol{\sigma}(\mathbf{x}') - \mathbf{C}^0(\mathbf{x}) : \Delta\boldsymbol{\varepsilon}(\mathbf{x}')\right] d\mathbf{x}'. \tag{2.16}$$

The integral equation (2.16) based on a heterogeneous reference material has been used in some existing reduced order methods, such as transformation field analysis (TFA) [**28**] and

nonlinear transformation field analysis (NTFA) [**86**]. It can be observed that the integral equation for a homogeneous material is a special case of the one for a heterogeneous material, and the strain concentration tensor $\mathbf{A}(\mathbf{x})$ in Eq. (2.16) is equal to the fourth-order identity tensor $\mathbf{II}$,

$$\mathbf{A}(\mathbf{x}) = \mathbf{II} \tag{2.17}$$

Since the physical problem is fully determined by the equilibrium condition, the solution of the continuous integral equation $\Delta\boldsymbol{\varepsilon}(\mathbf{x})$ does not depend on the choice of the reference material. Moreover, the continuous integral equation can be equivalently decomposed as

$$\int_{\Omega} \boldsymbol{\Phi}^0(\mathbf{x}, \mathbf{x}') : \Delta\boldsymbol{\sigma}(\mathbf{x}') d\mathbf{x}' = \mathbf{0} \tag{2.18}$$

and

$$\Delta\boldsymbol{\varepsilon}(\mathbf{x}) = \mathbf{A}(\mathbf{x}) : \Delta\boldsymbol{\varepsilon}_M + \int_{\Omega} \boldsymbol{\Phi}^0(\mathbf{x}, \mathbf{x}') : \left[\mathbf{C}^0(\mathbf{x}) : \Delta\boldsymbol{\varepsilon}(\mathbf{x}')\right] d\mathbf{x}'. \tag{2.19}$$

In other words, we have

$$Eq.(2.18) + Eq.(2.19) \rightleftarrows Eq.(2.16). \tag{2.20}$$

In order to prove the relation in (2.20), we will only need to show that Eq.(2.19) is satisfied if and only if the strain field $\Delta\boldsymbol{\varepsilon}(\mathbf{x})$ is compatible:

$$\Delta\boldsymbol{\varepsilon}(\mathbf{x}) \text{ is compatible} \rightleftarrows \text{Eq.(2.19)}. \tag{2.21}$$

Proof. of (2.21): For "$\Delta\boldsymbol{\varepsilon}(\mathbf{x})$ is compatible $\rightarrow$ Eq.(2.19)", assume the stiffness tensor of the real material vanishes everywhere inside the RVE, that is,

$$C_{ijkl}(\mathbf{x}) = \mathbf{0}.$$

For any compatible strain field, the equilibrium condition of this zero-stiffness material should be satisfied,

$$\frac{\partial C_{ijkl}\varepsilon_{ij}(\mathbf{x})}{\partial x_i} = 0 \quad \text{in } \Omega.$$

Then the equilibrium condition can be written as an integral equation with $C_{ijkl}(\mathbf{x}) = \mathbf{0}$, which yields Eq. (2.19).

For "Eq.(2.19) $\rightarrow$ $\Delta\boldsymbol{\varepsilon}(\mathbf{x})$ is compatible", we can utilize the property of the Green's function, namely that it maps any stress field to a compatible strain field,

$$\int_{\Omega} \boldsymbol{\Phi}^0(\mathbf{x}, \mathbf{x}') : \left[\mathbf{C}^0(\mathbf{x}) : \Delta\boldsymbol{\varepsilon}(\mathbf{x}')\right] d\mathbf{x}' \text{ is compatible.}$$

By definition of the strain concentration tensor of the reference material, the term $\mathbf{A}(\mathbf{x}) : \Delta\boldsymbol{\varepsilon}_M$ is also compatible. As a result, $\Delta\boldsymbol{\varepsilon}(\mathbf{x})$ is a compatible strain field. □

In some direct methods for solving the continuous Lippmann-Schwinger equation [**86, 105, 24**], Eq. (2.18) and (2.19) have been used to simplify the solution algorithm. However, it should be noted that after the discretization, the solution of the discontinuous integral equation is no longer independent of the reference material, and the relation in (2.20) will also not hold any more.

2.3. Green's function

The key to the integral equation is the corresponding Green's function of the reference material. It is firstly derived for a homogeneous linear elastic reference material. The auxiliary problem of the reference material subject to a periodic polarization stress field $\mathbf{p}(\mathbf{x})$ is to find the periodic solution $\mathbf{u}^*(\mathbf{x})$ so that the following system of equations can be satisfied,

$$\begin{cases} \boldsymbol{\sigma}(\mathbf{x}) = \mathbf{C}^0 : \boldsymbol{\varepsilon}^*(\mathbf{u}^*(\mathbf{x})) + \mathbf{p}(\mathbf{x}) \\ \nabla \cdot \boldsymbol{\sigma}(\mathbf{x}) = \mathbf{0} \end{cases} \tag{2.22}$$

where the strain $\boldsymbol{\varepsilon}^*$ can be expressed as

$$\boldsymbol{\varepsilon}^* = \frac{1}{2}\left(\nabla \mathbf{u}^* + \nabla^T \mathbf{u}^*\right) \tag{2.23}$$

Suppose all the quantities are given in the form of single wave with a wave vector $\boldsymbol{\xi}$ corresponding to the periodicity of the RVE,

$$\mathbf{u}^*(\mathbf{x}) = \hat{\mathbf{u}}^*(\boldsymbol{\xi}) \exp(\mathrm{i}\boldsymbol{\xi} \cdot \mathbf{x}), \quad \boldsymbol{\varepsilon}^*(\mathbf{x}) = \hat{\boldsymbol{\varepsilon}}^*(\boldsymbol{\xi}) \exp(\mathrm{i}\boldsymbol{\xi} \cdot \mathbf{x}) \tag{2.24}$$

$$\boldsymbol{\sigma}^*(\mathbf{x}) = \hat{\boldsymbol{\sigma}}^*(\boldsymbol{\xi}) \exp(\mathrm{i}\boldsymbol{\xi} \cdot \mathbf{x}), \quad \mathbf{p}^*(\mathbf{x}) = \hat{\mathbf{p}}^*(\boldsymbol{\xi}) \exp(\mathrm{i}\boldsymbol{\xi} \cdot \mathbf{x}). \tag{2.25}$$

Then the system of equations in Eq. (2.22) can be written as

$$\begin{cases} \hat{\sigma}_{ij}(\boldsymbol{\xi}) = \mathrm{i} C^0_{ijkl} \xi_l \hat{u}^*_k(\boldsymbol{\xi}) + \hat{\mathrm{p}}_{ij}(\boldsymbol{\xi}) \\ \mathrm{i}\hat{\sigma}_{ij}(\boldsymbol{\xi}) \xi_j = 0 \end{cases} \tag{2.26}$$

Eliminating the term $\hat{\sigma}_{ij}(\boldsymbol{\xi})$ in 2.26 yields

$$C^0_{ijkl} \xi_l \xi_j \hat{u}^*_k(\boldsymbol{\xi}) = \mathrm{i}\hat{\mathrm{p}}_{ij}(\boldsymbol{\xi}) \xi_j \tag{2.27}$$

Use the notation

$$K_{ik}(\boldsymbol{\xi}) = C^0_{ijkl} \xi_l \xi_j. \tag{2.28}$$

Due to the symmetry of the stiffness tensor, the matrix $\mathbf{K}(\boldsymbol{\xi})$ is also symmetric. Eq. (2.27) can be rewritten as

$$K_{ik}(\boldsymbol{\xi}) \hat{u}^*_k(\boldsymbol{\xi}) = \mathrm{i}\hat{\mathrm{p}}_{ij}(\boldsymbol{\xi}) \xi_j. \tag{2.29}$$

The auxiliary displacement field is solved by

$$\hat{u}^*_k(\boldsymbol{\xi}) = \mathrm{i} N_{ki}(\boldsymbol{\xi}) \xi_j \hat{\mathrm{p}}_{ij}(\boldsymbol{\xi}), \tag{2.30}$$

where $N_{il}(\boldsymbol{\xi})$ denotes the component of the inverse of the matrix $\mathbf{K}(\boldsymbol{\xi})$,

$$\mathbf{N}(\boldsymbol{\xi}) = \mathbf{K}^{-1}(\boldsymbol{\xi}) \tag{2.31}$$

Based on the symmetry of the polarization stress $\hat{\mathrm{p}}_{ij}$, we have

$$\hat{u}^*_k(\boldsymbol{\xi}) = \frac{\mathrm{i}}{2} \left(N_{ki}(\boldsymbol{\xi}) \xi_j + N_{kj}(\boldsymbol{\xi}) \xi_i \right) \hat{\mathrm{p}}_{ij}(\boldsymbol{\xi}), \tag{2.32}$$

Thus, the auxiliary strain field can be written as

$$\hat{\varepsilon}^*_{km}(\boldsymbol{\xi}) = -\frac{1}{4} \left(N_{ki}(\boldsymbol{\xi}) \xi_j \xi_m + N_{kj}(\boldsymbol{\xi}) \xi_i \xi_m + N_{mi}(\boldsymbol{\xi}) \xi_j \xi_k + N_{mj}(\boldsymbol{\xi}) \xi_i \xi_k \right) \hat{\mathrm{p}}_{ij}(\boldsymbol{\xi}). \tag{2.33}$$

Finally, the Green's function Φ^0_{lmij} can be defined as a tensor mapping from the polarization stress $\hat{\mathrm{p}}_{ij}(\boldsymbol{\xi})$ to the auxiliary strain $\hat{\varepsilon}^*_{km}(\boldsymbol{\xi})$,

$$\Phi^0_{kmij}(\boldsymbol{\xi}) = \frac{1}{4}\left(N_{ki}(\boldsymbol{\xi})\xi_j\xi_m + N_{kj}(\boldsymbol{\xi})\xi_i\xi_m + N_{mi}(\boldsymbol{\xi})\xi_j\xi_k + N_{mj}(\boldsymbol{\xi})\xi_i\xi_k\right) \tag{2.34}$$

As shown in Mura's book [**95**], the expression of $\mathbf{N}(\boldsymbol{\xi})$ can be very complex for anisotropic materials. However, its form becomes particularly simple for a isotropic linear elastic reference material. The stiffness tensor $\mathbf{C}^0$ is determined by two independent Lamé parameters λ^0 and μ^0,

$$\mathbf{C}^0 = \mathbf{f}(\lambda^0, \mu^0) = \lambda^0 \mathbf{I} \otimes \mathbf{I} + \mu^0 \mathbf{II}. \tag{2.35}$$

where $\mathbf{I}$ is the second-rank identity tensor, and $\mathbf{II}$ is the symmetric part of the fourth-rank identity tensor. Based on the definitions in Eq. (2.28) and (2.31), it can be derived that

$$N_{ij}(\boldsymbol{\xi}) = \frac{1}{\mu^0 \mid \boldsymbol{\xi} \mid^2}\left(\delta_{ij} - \frac{\lambda^0 + \mu^0}{\lambda^0 + 2\mu^0}\frac{\xi_i\xi_j}{\mid \boldsymbol{\xi} \mid^2}\right). \tag{2.36}$$

Substituting Eq. (2.36) into (2.34), the Green's function is obtained

$$\hat{\Phi}^0_{ijkl}(\boldsymbol{\xi}) = \frac{1}{4\mu^0 \mid \boldsymbol{\xi} \mid^2}\left(\delta_{ki}\xi_j\xi_l + \delta_{il}\xi_j\xi_k + \delta_{jl}\xi_i\xi_k + \delta_{jk}\xi_i\xi_l\right) - \frac{\lambda^0 + \mu^0}{\mu^0(\lambda^0 + 2\mu^0)}\frac{\xi_i\xi_j\xi_k\xi_l}{\mid \boldsymbol{\xi} \mid^4}. \tag{2.37}$$

It is also possible to write the Green's function of isotropic linearly elastic reference material explicitly in the real space, and the detailed expressions in 2D and 3D can be found in [**95, 71**]. Due to the symmetry of the strain and stress tensor under small-deformation assumption, the fourth-order Green's function can be simplified as a second-order tensor through Voigt notation. However, it will not be the case when finite strain is considered. For heterogeneous elastic reference material, there is usually no closed-form solution of its Green's function in either frequency or spacial domain. Thus, it has to be determined numerically by solving the RVE problem using DNS methods [**36**].

2.4. Finite strain generalization

The extension of Lippmann-Schwinger equation from small strain to finite strain is straightforward. For finite strain, all the equations are formulated in the reference configuration. The stress and strain measures become the first Piola-Kirchhoff stress $\mathbf{P}(\mathbf{X})$ and the deformation gradient $\mathbf{F}(\mathbf{X})$, respectively. The equilibrium condition in the reference configuration can be written as

$$\frac{\partial P_{ij}(\mathbf{X})}{\partial X_i} = 0 \quad \text{in } \Omega^0. \tag{2.38}$$

Similarly, a homogeneous reference material comes into play, whose constitutive law is given by

$$\mathbf{P} = \mathbf{C}^0 : \mathbf{F}, \tag{2.39}$$

It should be noted that the constitutive law of the reference material may not be physical, and the reason of taking the form in Eq. (2.39) is for the ease of deriving the Green's function and developing the integral equation. Since the physical problem is fully determined by the equilibrium condition and real material properties, the choice of the reference material will not affect the solution. The integral equation for finite strain can be written as

$$\mathbf{F}(\mathbf{X}) + \int_{\Omega^0} \mathbf{\Phi}^0(\mathbf{X}, \mathbf{X}') : \left[\mathbf{P}(\mathbf{X}') - \mathbf{C}^0 : \mathbf{F}(\mathbf{X}')\right] d\mathbf{X}' - \mathbf{F}^0 = 0, \tag{2.40}$$

where $\mathbf{\Phi}^0(\mathbf{X}, \mathbf{X}')$ is the Green's function of the reference material. The far-field deformation gradient $\mathbf{F}^0$ is equal to the averaged deformation gradient in the RVE,

$$\mathbf{F}^0 = \int_{\Omega^0} \mathbf{F}(\mathbf{X}) d\mathbf{X}. \tag{2.41}$$

The derivation of the Green's function still follows the same procedure. In the frequency domain, the auxiliary strain field can be expressed as

$$\hat{u}_k^*(\boldsymbol{\xi}) = \mathrm{i} N_{ki}(\boldsymbol{\xi}) \xi_j \hat{\mathrm{P}}_{ij}(\boldsymbol{\xi}), \tag{2.42}$$

where $\hat{\mathrm{P}}_{ij}(\boldsymbol{\xi})$ is the polarization first Piola-Kirchhoff stress. Then the deformation gradient becomes

$$\hat{F}_{km}(\boldsymbol{\xi}) = -N_{ki}(\boldsymbol{\xi})\xi_j\xi_m\hat{\mathrm{P}}_{ij}(\boldsymbol{\xi}) \tag{2.43}$$

The Green's function can be extracted as

$$\Phi^0_{kmij}(\boldsymbol{\xi}) = N_{ki}(\boldsymbol{\xi})\xi_j\xi_m \tag{2.44}$$

Since $\mathbf{P}$ and $\mathbf{F}$ are no longer symmetric, the Green's function for finite strain Φ^0_{ijkl} only has major symmetry, so that it can not be written in Voigt notation.

Again, explicit formulation can be derived for the Green's function if $\mathbf{C}^0$ represents a isotropic elastic material: $\mathbf{C}^0 = \mathbf{f}(\lambda^0, \mu^0) = \lambda^0\mathbf{I}\otimes\mathbf{I} + \mu^0\mathbf{II}$. Substituting Eq. (2.36) into (2.44) yields

$$\Phi^0_{ijkl}(\boldsymbol{\xi}) = \frac{1}{\mu^0 \mid \boldsymbol{\xi} \mid^2}\left(\delta_{ik}\xi_j\xi_l - \frac{\lambda^0+\mu^0}{\lambda^0+2\mu^0}\frac{\xi_i\xi_j\xi_k\xi_l}{\mid \boldsymbol{\xi} \mid^2}\right). \tag{2.45}$$

Although this thesis will mainly investigate the problems under small-strain assumption, it is possible to extend the developed methods in Section 3 and 4 to the finite-strain regime, which will be important for considering material behaviors under large deformation, such as hyperelasticity and crystal plasticity.

CHAPTER 3

Analytical Homogenization: an Extended Micromechanics Theory for Overlapping Geometries

Micromechanics methods aim to solve the integral equation through analytical or semi-analytical approaches. Based on analytical solutions of representative material systems and homogenization assumptions, these micromechanics model typically have much less degrees of freedoms than FE or FFT-based models. However, other than the limited predicting accuracy, a difficulty of most of the existing analytical micromechanics models is that simple shaped inclusions must remain unique, and the physical pictures behind those models become vague once inclusions' ranges of influence begin to overlap and strong interactions begin to occur. Mori-Tanaka [**92, 10**] and self-consistent methods [**48, 23**]) are sensitive to the volume fraction of the inclusion phase, but cannot distinguish between inclusions that are well dispersed (nonoverlaping) or strongly interacted (overlapping). For example, let us consider a two-phase material with spherical inclusions embedded in the matrix. If the inclusions do not overlap, the matrix phase is always continuous and dominates the overall properties of the two-phase material even for high volume fraction of the inclusion phase. However, when the inclusions can overlap, the inclusions can percolate through the matrix and become a competitor of the matrix phase as the volume fraction increases. Another challenge in modeling the overlap is that the physics in the overlapping regions will vary with the material system. Thus, many different overlapping conditions may be necessary to account for a wide range of overlapping phenomena. In this chapter, a new analytical reduced-order homogenization method for overlapping geometries is proposed, which can account for complex microstructural morphologies due to inclusion overlapping and establish a unified mathematical framework for different overlapping conditions.

3.1. Mathematical formulations of overlapping

Before introducing different overlapping conditions, let us start with the RVE domain containing N overlapping inclusions. The domain of each inclusion is denoted as Ω^r, with $r = 1, 2, ..., N$. Due to the existence of overlapping, we have

$$\bigcap_{r=1}^{N} \Omega^r \neq \emptyset. \tag{3.1}$$

The combined domain of all inclusion phases Ω^c and domain of the matrix phase Ω^m can be expressed as

$$\Omega^c = \bigcup_{r=1}^{N} \Omega^r, \quad \Omega^m = \Omega \setminus \bigcup_{r=1}^{N} \Omega^r. \tag{3.2}$$

Furthermore, the volume fraction of the inclusion phase is

$$f_c = \frac{|\Omega^c|}{|\Omega|}, \text{ with } |\Omega| = |\Omega^c| + |\Omega^m|. \tag{3.3}$$

Here, I use the characteristic function to identify the region of each inclusion,

$$\chi_r(\mathbf{x}) = \begin{cases} 1 & \text{if } x \in \Omega^r \\ 0 & \text{otherwise} \end{cases}, \tag{3.4}$$

where $\chi^r(\mathbf{x})$ is the characteristic function of the r-th inclusion at point $\mathbf{x}$.

Meanwhile, the reference medium is assumed to share the same properties as the matrix material, and the integral equation in terms of the strain $\boldsymbol{\varepsilon}$ becomes

$$\varepsilon_{ij}(\mathbf{x}) = \varepsilon^0_{ij} - \int_{\Omega^c} \Phi^0_{ijkl}(\mathbf{x}, \mathbf{x}') \delta C_{klmn}(\mathbf{x}') \varepsilon_{mn}(\mathbf{x}') d\mathbf{x}' \quad \text{in } \Omega, \tag{3.5}$$

where ε^0_{ij} is the far field strain and where

$$\delta\mathbf{C}(\mathbf{x}) = \mathbf{C}(\mathbf{x}) - \mathbf{C}^0. \tag{3.6}$$

The fourth-order Green's function of the reference medium $\Phi^0_{ijkl}(\mathbf{x}, \mathbf{x}')$ represents the strain contribution at $\mathbf{x}$ from a concentrated external stress at $\mathbf{x}'$. Expressions of Green's functions for isotropic 2-D plane strain and 3-D material can be found in [**95**]. It should be

noted that this Green's function will not be directly used in the proposed micromechanics method. Instead, analytical expressions of its integrals (such as Eshelby's tensor [**32**]) will be adopted.

By solving Eq. (3.5) in the material domain with prescribed boundary conditions, one can homogenize the local responses to get the macroscopic properties. Before proceeding to the details of homogenization, the material domain Ω is defined to be an RVE, so that its size greatly exceeds the wavelength of the local fluctuations of strain and stress fields. The overall properties of the RVE should not depend on the boundary conditions, and it can be treated as a homogeneous material at the macro-scale. With the energy equivalence indicated by Hill-Mandel principle of macro-homogeneity in Eq. (1.1), the RVE can be treated as a homogeneous material so that an effective constitutive relationship can be defined as,

$$\langle \boldsymbol{\sigma} \rangle_\Omega = \bar{\mathbf{C}} : \langle \boldsymbol{\varepsilon} \rangle_\Omega, \tag{3.7}$$

where $\bar{\mathbf{C}}$ is the effective stiffness tensor of the heterogeneous material.

The average strain in the RVE can be determined by taking the volume average of strain inside Ω,

$$\bar{\boldsymbol{\varepsilon}} = \langle \boldsymbol{\varepsilon} \rangle_\Omega = \frac{1}{|\Omega|} \int_\Omega \boldsymbol{\varepsilon}(\mathbf{x}) d\mathbf{x}, \tag{3.8}$$

where $|\Omega|$ is the volume of the RVE. Furthermore, the average stress inside the RVE domain is

$$\bar{\boldsymbol{\sigma}} = \langle \boldsymbol{\sigma} \rangle_\Omega = \frac{1}{|\Omega|} \int_\Omega \left[\mathbf{C}^0 + \delta\mathbf{C}(\mathbf{x}) \right] \boldsymbol{\varepsilon}(\mathbf{x}) = \mathbf{C}^0 : \bar{\boldsymbol{\varepsilon}} + \langle \delta\mathbf{C}(\mathbf{x}) : \boldsymbol{\varepsilon}(\mathbf{x}) \rangle_{\Omega^c}. \tag{3.9}$$

As we can see from Eq. (3.9), the key step in the homogenization is to calculate the *average polarization stress* $\langle \delta\mathbf{C}(\mathbf{x}) : \boldsymbol{\varepsilon}(\mathbf{x}) \rangle_{\Omega^c}$ as a function of a certain macroscopic quantity (e.g., average strain $\bar{\boldsymbol{\varepsilon}}$), and then the effective stiffness tensor can be computed based on Eq. (3.7). Due to inclusion overlapping, $\langle \delta\mathbf{C}(\mathbf{x}) : \boldsymbol{\varepsilon}(\mathbf{x}) \rangle_{\Omega^c}$ is not naturally a linear combination of the contribution from each individual inclusion, which blurs the physical picture behind most micromechanics methods which are based on a single representative

inclusion. As will be shown later, this issue can be resolved by properly choosing the overlapping conditions, which govern the calculation of moduli in the overlapping region.

In this section, I will introduce two basic overlapping conditions: 1) the weighted-mean overlapping condition and 2) the additive overlapping condition. Figure 3.1 shows the relative modulus in an overlapping region $\delta\mathbf{C}(\mathbf{x})$ normalized by the relative inclusion modulus $\delta\mathbf{C}^c$ for a system with constant modulus inclusions. Then, the new strain

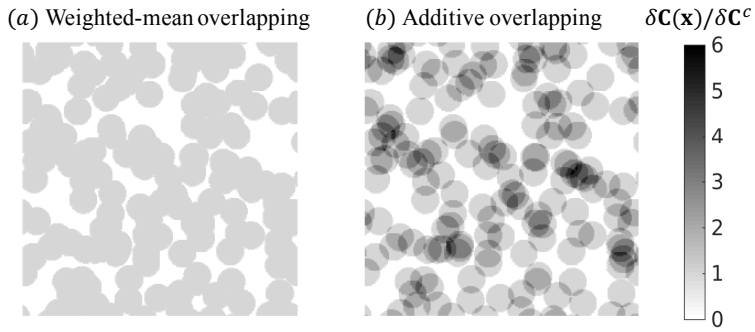

Figure 3.1. 2-D examples of Boolean-Poisson model under (a) weighted-mean (with all weights set to 1) and (b) additive overlapping conditions. The volume fraction of the inclusion phase is 70%.

definitions and modified integral equations in each inclusion, as well as expressions of the average polarization stress, will be derived under both conditions. A unified micromechanics method will be proposed in Section 3.2 to predict the effective properties of heterogeneous materials with overlapping effects.

3.1.1. Weighted-mean overlapping condition

First, I will introduce the weighted-mean overlapping condition. The goal is to formulate the weighted-mean overlapping condition such that if the material is uniform in each inclusion before overlapping, the material properties are also uniform after overlapping (i.e., the resulting heterogeneous material only has two phases). The relative stiffness

tensor at any point in Ω^c is chosen to be

$$\delta\mathbf{C}(\mathbf{x}) = \frac{\sum_{r=1}^{N} \chi_r(\mathbf{x})\eta_r(\mathbf{x})\delta\mathbf{C}^r(\mathbf{x})}{\sum_{r=1}^{N} \chi_r(\mathbf{x})\eta_r(\mathbf{x})} = \frac{\sum_{r=1}^{N} \chi'_r(\mathbf{x})\delta\mathbf{C}^r(\mathbf{x})}{\sum_{r=1}^{N} \chi'_r(\mathbf{x})}, \tag{3.10}$$

where $\eta_r(\mathbf{x})$ is the weighting function in the r-th inclusion, and $\chi'_r(\mathbf{x})$ is the weighted characteristic function defined as

$$\chi'_r(\mathbf{x}) = \chi_r(\mathbf{x})\eta_r(\mathbf{x}). \tag{3.11}$$

The weighting function is employed–primarily–to enforce impenetrability of phases. The weighting function can be chosen to have a high value for phases that are considered to be impenetrable (i.e., no overlap allowed). For instance, a point in a high weighted particle region overlapped by a low weighted interphase region would take on the properties of the particle region, as if the overlap had not occurred. Substituting Eq. (3.10) into the original integral equation (3.5) and decomposing the integral into each individual inclusion domain gives,

$$\varepsilon_{ij}(\mathbf{x}) = \varepsilon^0_{ij} - \sum_{s=1}^{N} \int_{\Omega_s} \Phi_{ijkl}(\mathbf{x},\mathbf{x}') \left(\frac{\chi'_s(\mathbf{x}')\delta C^s_{klmn}(\mathbf{x}')}{\sum_{t=1}^{N} \chi'_t(\mathbf{x})} \right) \varepsilon_{mn}(\mathbf{x}')d\mathbf{x}' \quad \text{in } \Omega. \tag{3.12}$$

Decomposing the total strain at $\mathbf{x}'$ gives the strain in the s-th inclusion which can be defined as

$$\boldsymbol{\varepsilon}^s(\mathbf{x}') = \frac{\chi'_s(\mathbf{x}')}{\sum_{t=1}^{N} \chi'_t(\mathbf{x}')}\boldsymbol{\varepsilon}(\mathbf{x}'). \tag{3.13}$$

After substituting Eq. (3.13) into (3.12), we obtain

$$\varepsilon_{ij}(\mathbf{x}) = \sum_{s=1}^{N} \varepsilon^s_{ij}(\mathbf{x}) = \varepsilon^0_{ij} - \sum_{s=1}^{N} \int_{\Omega_s} \Phi_{ijkl}(\mathbf{x},\mathbf{x}')\delta C^s_{klmn}(\mathbf{x}')\varepsilon^s_{mn}(\mathbf{x}')d\mathbf{x}' \quad \text{in } \Omega. \tag{3.14}$$

Also as imposed by the definition of the strain in each inclusion (see Eq. (3.13)), the following relationship must be satisfied,

$$\chi'_t(\mathbf{x})\boldsymbol{\varepsilon}^s(\mathbf{x}) = \chi'_s(\mathbf{x})\boldsymbol{\varepsilon}^t(\mathbf{x}) \quad \text{in } \Omega. \tag{3.15}$$

As a result, the integral equation in the r-th inclusion can be derived as

$$\left(\sum_{s=1}^{N} \chi'_s(\mathbf{x})/\chi'_r(\mathbf{x})\right)\varepsilon^r_{ij}(\mathbf{x}) = \varepsilon^0_{ij} - \sum_{s=1}^{N}\int_{\Omega_s} \Phi_{ijkl}(\mathbf{x},\mathbf{x}')\delta C^s_{klmn}(\mathbf{x}')\varepsilon^s_{mn}(\mathbf{x}')d\mathbf{x}' \quad \text{in } \Omega^r. \tag{3.16}$$

The key term in the homogenization procedure is the average polarization stress $\langle\delta\mathbf{C}(\mathbf{x}) : \boldsymbol{\varepsilon}(\mathbf{x})\rangle_\Omega$, and it can be computed as a summation of the contribution from each inclusion based on Eq. (3.10) and (3.13).

$$\langle\delta\mathbf{C}(\mathbf{x}) : \boldsymbol{\varepsilon}(\mathbf{x})\rangle_\Omega = \frac{1}{|\Omega|}\int_\Omega \delta\mathbf{C}(\mathbf{x}) : \boldsymbol{\varepsilon}(\mathbf{x})d\mathbf{x} = \frac{1}{|\Omega|}\sum_{s=1}^{N}\int_{\Omega_s} \delta\mathbf{C}^s(\mathbf{x})\boldsymbol{\varepsilon}^s(\mathbf{x})d\mathbf{x}. \tag{3.17}$$

3.1.2. Additive overlapping condition

Another way of overlapping inclusions is to take the summation of relative stiffness tensors of all the inclusions involved in the overlapping. By using the characteristic function defined in Eq. (3.4), the relative stiffness tensor at any point in Ω can be written as

$$\delta\mathbf{C}(\mathbf{x}) = \sum_{r=1}^{N} \chi_r(\mathbf{x})\delta\mathbf{C}^r(\mathbf{x}). \tag{3.18}$$

Similarly, one can substitute Eq. (3.18) into the original integral equation (3.5) and decompose the integral into each individual inclusion domain, so that the new integral equation in Ω becomes

$$\varepsilon_{ij}(\mathbf{x}) = \varepsilon^0_{ij} - \sum_{s=1}^{N}\int_{\Omega_s} \Phi_{ijkl}(\mathbf{x},\mathbf{x}')\chi_s(\mathbf{x}')\delta C^s_{klmn}(\mathbf{x}')\varepsilon_{mn}(\mathbf{x}')d\mathbf{x}' \quad \text{in } \Omega. \tag{3.19}$$

In Eq. (3.19), the strain in the s-th inclusion can be defined as

$$\boldsymbol{\varepsilon}^s(\mathbf{x}') = \chi_s(\mathbf{x}')\boldsymbol{\varepsilon}(\mathbf{x}'). \tag{3.20}$$

According to the definition of $\boldsymbol{\varepsilon}^s(\mathbf{x}')$, the following condition should be satisfied,

$$\chi_t(\mathbf{x})\boldsymbol{\varepsilon}^s(\mathbf{x}) = \chi_s(\mathbf{x})\boldsymbol{\varepsilon}^t(\mathbf{x}) \quad \text{in } \Omega. \tag{3.21}$$

Finally, the integral equation in the r-th inclusion becomes

$$\varepsilon^r_{ij}(\mathbf{x}) = \varepsilon^0_{ij} - \sum_{s=1}^{N} \int_{\Omega_s} \Phi_{ijkl}(\mathbf{x}, \mathbf{x}')\delta C^s_{klmn}(\mathbf{x}')\varepsilon^s_{mn}(\mathbf{x}')d\mathbf{x}' \quad \text{in } \Omega^r. \tag{3.22}$$

It can be shown that Eq. (3.17) for the average polarization stress $\langle \delta\mathbf{C}(\mathbf{x}) : \boldsymbol{\varepsilon}(\mathbf{x})\rangle_\Omega$ is also satisfied under additive overlapping condition.

In Table 3.1, I summarize the mathematical formulations of both weighted-mean and additive overlapping conditions.

Table 3.1. Summary of mathematical formulations for weighted-mean and additive overlapping conditions.

	Weighted-mean overlapping	Additive overlapping
Overall relative stiffness tensor	$\delta\mathbf{C}(\mathbf{x}) = \dfrac{\sum_{r=1}^{N} \chi'_r(\mathbf{x})\delta\mathbf{C}^r(\mathbf{x})}{\sum_{r=1}^{N} \chi'_r(\mathbf{x})}$	$\delta\mathbf{C}(\mathbf{x}) = \sum_{r=1}^{N} \chi_r(\mathbf{x})\delta\mathbf{C}^r(\mathbf{x})$
Definition of strain in each inclusion	$\boldsymbol{\varepsilon}^s(\mathbf{x}') = \dfrac{\chi'_s(\mathbf{x}')}{\sum_{t=1}^{N} \chi'_t(\mathbf{x}')}\boldsymbol{\varepsilon}(\mathbf{x}')$	$\boldsymbol{\varepsilon}^s(\mathbf{x}') = \chi_s(\mathbf{x}')\boldsymbol{\varepsilon}(\mathbf{x}')$
The integral equation in each inclusion	$L^r(\mathbf{x})\varepsilon^r_{ij}(\mathbf{x}) = \varepsilon^0_{ij} - \sum_{s=1}^{N} \int_{\Omega_s} \Phi_{ijkl}(\mathbf{x}, \mathbf{x}')\delta C^s_{klmn}(\mathbf{x}')\varepsilon^s_{mn}(\mathbf{x}')d\mathbf{x}'$	
	$L^r(\mathbf{x}) = \sum_{s=1}^{N} \chi'_s(\mathbf{x})/\chi'_r(\mathbf{x})$	$L^r(\mathbf{x}) = 1$
Average polarization stress	$\langle \delta\mathbf{C}(\mathbf{x}) : \boldsymbol{\varepsilon}(\mathbf{x})\rangle_\Omega = \dfrac{1}{\lvert\Omega\rvert} \sum_{s=1}^{N} \int_{\Omega_s} \delta\mathbf{C}^s(\mathbf{x})\boldsymbol{\varepsilon}^s(\mathbf{x})d\mathbf{x}$	

By comparing Eq. (3.22) with (3.16), one can see that the only difference is the coefficient $L^r(\mathbf{x})$ before $\varepsilon^r_{ij}(\mathbf{x})$ on the left hand side, due to different definitions of the strain in each inclusion. It should be noted, that the entire procedure of deriving the integral equation in each inclusion–based on the given overlapping condition–is general,

and it can be applied to other overlapping conditions as long as the overall relative stiffness tensor is a linear combination of those in each inclusion. Although the overlap condition could take many forms based on the physics of a material system, I will focus on the weighted-mean and additive overlapping conditions in this chapter.

3.2. General homogenizing scheme

In this section, I aim to calculate the effective constitutive equation for a heterogeneous material containing multiple overlapping inclusions. Rather than using full direct numerical simulation, which is time-consuming (especially for complex microstructures with important features on scales much smaller than the RVE, such as nanocomposite), an analytical micromechanics method will be developed to homogenize the multi-inclusion system more efficiently, and to take into account inclusion overlap.

The first step is to elucidate the essential assumption of the extended micromechanics methods for overlapping geometries. In order to probe the properties at a given point, a new *test* inclusion randomly will be inserted into the original material. Since overlapping is allowed, this *test* inclusion may overlap with the matrix material and other existing inclusions at the same time. In order to simplify the physical picture, the dimension of the *test* inclusion is assumed to be orders of magnitude smaller than the original inclusions, while its shape and material constituents are kept the same. Therefore, the strain and material properties surrounding the *test* inclusion can be considered constant, and the overlapping state in the *test* inclusion can be considered homogeneous. For example, if the *test* inclusion was relatively large, it could overlap with one inclusion through part of its domain and two inclusions through another part, and the physical picture would be more complicated. Under this assumption, the *test* inclusion is equivalent to a sampling point in the original material, and the outcomes of this random testing process form a sample space Ξ,

$$\Xi = \{\xi_0, \xi_1, \xi_2, ...\}, \quad \text{with} \sum_{\xi_i \in \Xi} p(\xi_i) = 1, \tag{3.23}$$

where ξ_i is an overlapping state in Ξ at the sampling point (or *test* inclusion), and p is a probability function mapping Ξ to $[0, 1]$. For example, $p(\xi_0)$ represents the probability that the sampling point is in the matrix material, and $p(\xi_3)$ in the Boolean-Poisson model (see Eq. (A.3)) represents the probability that the sampling point overlaps with three inclusions.

For the overlapping state ξ_0, there is no overlapping of inclusions at the sampling point, so that the *test* inclusion is inserted into the matrix material as shown in Figure A.1(a). For this state, the strain in the *test* inclusion $\boldsymbol{\varepsilon}^{\text{test}}$ can be related to the average strain in the matrix $\bar{\boldsymbol{\varepsilon}}^m$ (similar to the concept in the Mori-Tanaka method [**92, 10**]),

$$\boldsymbol{\varepsilon}^{\text{test}}_{(\xi_0)} = \mathbf{T}_{(\xi_0)} : \bar{\boldsymbol{\varepsilon}}^m, \tag{3.24}$$

where $\mathbf{T}_{(\xi_0)}$ depends on the shape of the inclusion, the properties of both the inclusion and matrix materials, and is not necessarily uniform in the inclusion. However, when the test inclusion is ellipsoidal in 3D (or elliptic in 2-D) with uniform material properties, $\mathbf{T}_{(\xi_0)}$ will be a constant relating to the Eshelby's tensor $\mathbf{S}^m$ of the matrix material. The definition of Eshelby's tensor can be found in Appendix B, and its expression for a 3-D spherical inclusion in given in Eq. (B.4). More interestingly, Benveniste has shown that Eq. (3.24) takes inclusion interactions into account although $\boldsymbol{\varepsilon}^{\text{test}}_{(\xi_0)}$ is only a function of $\bar{\boldsymbol{\varepsilon}}^m$ [**10**].

For the overlapping state $\xi_i (i \neq 0)$, the *test* inclusion is inserted into a non-matrix region with a stiffness tensor $\mathbf{C}_{(\xi_i)}$ and strain $\hat{\boldsymbol{\epsilon}}_{(\xi_i)}$. Similarly, the strain in the test inclusion can be determined by

$$\boldsymbol{\varepsilon}^{\text{test}}_{(\xi_i)} = \mathbf{T}_{(\xi_i)} : \hat{\boldsymbol{\epsilon}}_{(\xi_i)} \quad \text{for } i \neq 0. \tag{3.25}$$

Other than the inclusion shape and material properties, $\mathbf{T}_{(\xi_i)}$ is also related to the overlapping condition and the corresponding integral equation (3.16) or (3.22).

In order to approximate the strain $\hat{\boldsymbol{\epsilon}}_{(\xi_i)}$, I use the strain concentration tensor $\mathbf{A}$ as

$$\hat{\boldsymbol{\epsilon}}_{(\xi_i)} = \mathbf{A}_{(\xi_i)} : \bar{\boldsymbol{\varepsilon}}. \tag{3.26}$$

where $\mathbf{A}_{(\xi_i)}$ is the strain concentration tensor of the overlapping state ξ_i. Inserting Eq. (3.26) in Eq. (3.25) gives:

$$\boldsymbol{\varepsilon}^{\text{test}}_{(\xi_i)} = \left(\mathbf{T}_{(\xi_i)} : \mathbf{A}_{(\xi_i)}\right) : \bar{\boldsymbol{\varepsilon}} \quad \text{for } i \neq 0, \tag{3.27}$$

For a 3-D spherical (or circular in 2-D) inclusion embedded in a homogeneous medium, the strain concentration tensor becomes a function of Eshelby's tensor, the properties of the inclusion, and the properties of the surrounding medium. Here, the inclusion is assumed to have a stiffness tensor $\mathbf{C}_{(\xi_i)}$. The surrounding material properties are assumed to be that of the effective medium $\bar{\mathbf{C}}$, as in self-consistent methods [**48, 23, 26**]. The strain concentration tensor of overlapping state ξ_i then becomes:

$$\mathbf{A}_{(\xi_i)} = \left[\mathbf{I} + \bar{\mathbf{S}} : \bar{\mathbf{C}}^{-1} : (\mathbf{C}_{(\xi_i)} - \bar{\mathbf{C}})\right]^{-1} \quad \text{for } i \neq 0, \tag{3.28}$$

where $\mathbf{I}$ is the forth-order identity tensor and by $\bar{\mathbf{S}}$ denotes the Eshelby's tensor of the effective medium. Using Eq. (3.28), the strain in the *test* inclusion becomes:

$$\boldsymbol{\varepsilon}^{\text{test}}_{(\xi_i)} = \left(\mathbf{T}_{(\xi_i)} : \left[\mathbf{I} + \bar{\mathbf{S}} : \bar{\mathbf{C}}^{-1} : (\mathbf{C}_{(\xi_i)} - \bar{\mathbf{C}})\right]^{-1}\right) : \bar{\boldsymbol{\varepsilon}} \quad \text{for } i \neq 0, \tag{3.29}$$

An illustration of the simplified model for state $\xi_i (i \neq 0)$ is provided in Figure 3.2(b).

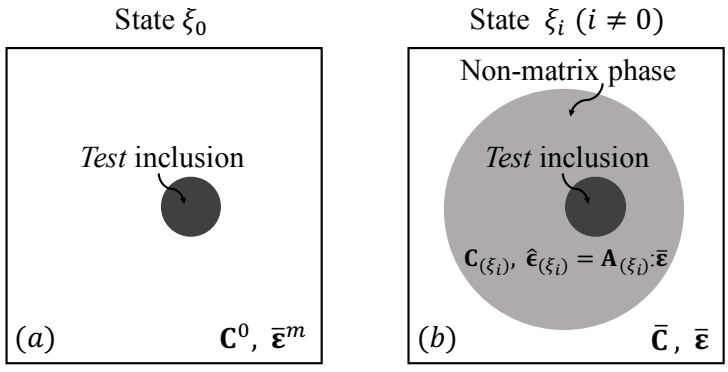

Figure 3.2. Illustration of the physical models for different overlapping states.

From Eq. (3.24) and (3.27), the expected value of strain in the *test* inclusion $\langle \boldsymbol{\varepsilon}^{\text{test}} \rangle$ is defined as

$$\langle \boldsymbol{\varepsilon}^{\text{test}} \rangle = \sum_{\xi_i \in \Xi} p(\xi_i) \boldsymbol{\varepsilon}^{\text{test}}_{(\xi_i)} = p(\xi_0) \mathbf{T}_{(\xi_0)} : \bar{\boldsymbol{\varepsilon}}^m + \left[\sum_{\xi_i \in (\Xi \setminus \xi_0)} p(\xi_i) \mathbf{T}_{(\xi_i)} : \mathbf{A}_{(\xi_i)} \right] : \bar{\boldsymbol{\varepsilon}} \tag{3.30}$$

In addition, the following equation for the average strain must be satisfied,

$$\bar{\boldsymbol{\varepsilon}} = (1 - f_c) \bar{\boldsymbol{\varepsilon}}^m + f_c \bar{\boldsymbol{\varepsilon}}^c, \tag{3.31}$$

where $\bar{\boldsymbol{\varepsilon}}^c$ is the average strain in the overall inclusion phase. By assuming that all of the inclusions share the same expectation of strain with the *test* inclusion, $\bar{\boldsymbol{\varepsilon}}^c$ can be written as a function of $\langle \boldsymbol{\varepsilon}^{\text{test}} \rangle$,

$$\bar{\boldsymbol{\varepsilon}}^c = \mathbf{F}(\langle \boldsymbol{\varepsilon}^{\text{test}} \rangle), \tag{3.32}$$

where $\mathbf{F}$ is a function depending on the overlapping condition (as shown in Eq. (3.38) and (3.46)). For a material with non-overlapping inclusions, one simply has $\bar{\boldsymbol{\varepsilon}}^c = \langle \boldsymbol{\varepsilon}^{\text{test}} \rangle$.

Finally, based on Eq. (1.1), (3.9) and (3.17), the effective stiffness $\bar{\mathbf{C}}$ can be calculated. As we can see from Eq. (3.30), the extended micromechanics method is self-consistent since $\mathbf{A}_{(\xi_i)}$ depends on $\bar{\mathbf{C}}$; therefore, the effective stiffness tensor will be calculated iteratively using a fix-point method in this work. A special case exists when the inclusions do not overlap with each other (or $p(\xi_0) = 1$), and Eq. (3.30) becomes

$$\langle \boldsymbol{\varepsilon}^{\text{test}} \rangle = \mathbf{T}_{(\xi_0)} : \bar{\boldsymbol{\varepsilon}}^m \quad \text{if } p(\xi_0) = 1. \tag{3.33}$$

In this case, the extended micromechanics method reproduces the Mori-Tanaka method, and no iteration is required when solving the effective stiffness tensor.

3.3. Results for Boolean-Poisson model under different overlapping conditions

In this section, the extended micromechanics method will be used to predict the effective stiffness tensors of the Boolean-Poisson model under weighted-mean and additive

overlapping conditions. Details of the Boolean-Poisson model can be found in Appendix A. The predictions will be compared with DNS results computed by the FFT-based method introduced by Moulinec and Suquet [**93**]. The original stiffness tensor before overlapping is uniform and equal to $\mathbf{C}^c$ in each inclusion.

The homogenization of the Boolean-Poisson model will be considered in the cases of spherical voids or spherical hard inclusions in 3-D. All the material interfaces are assumed to be perfectly bonded. The Young's modulus and Poisson's ratio of the matrix material are $E^0 = 1$ GPa and $\nu^0 = 0.3$. The material properties of hard inclusions are $E^c = 100$ GPa and $\nu^c = 0.3$. Due to convergence issues with the FFT-based DNS methods for infinite contrasted material properties [**93, 94**], the Young's modulus of "void" is chosen to be a small value (0.001 GPa) rather than equal to 0 GPa. In the FFT-based computations, I have run 6 samples on 200^3 grids for each set of material parameters.

1) Weighted-mean overlapping condition

For the weighted-mean overlapping condition, the weighting function of each inclusion $\eta_r(\mathbf{x})$ is chosen to be equal to 1, so that $\chi'_r(\mathbf{x}) = \chi_r(\mathbf{x})$. In the non-matrix region (i.e., overlapping state $\xi_i (i \neq 0)$), one has

$$\mathbf{C}_{(\xi_i)} = \mathbf{C}^c \quad \text{and } \mathbf{A}_{(\xi_i)} = \left[\mathbf{I} + \bar{\mathbf{S}} : \bar{\mathbf{C}}^{-1} : (\mathbf{C}^c - \bar{\mathbf{C}})\right]^{-1} \quad \text{for } i \neq 0. \tag{3.34}$$

Based on the inclusion-wise integral equation (3.16) under weighted-mean overlapping condition and Eshelby's solution for spherical inclusions, the concentration factors can be determined as,

$$\mathbf{T}_{(\xi_0)} = \left[\mathbf{I} + \mathbf{S}^0 : (\mathbf{C}^0)^{-1} : (\mathbf{C}^c - \mathbf{C}^0)\right]^{-1} \tag{3.35}$$

and

$$\mathbf{T}_{(\xi_i)} = \frac{1}{i+1}\left[\mathbf{I} + \mathbf{S}_{(\xi_i)} : \mathbf{C}^{-1}_{(\xi_i)} : (\mathbf{C}^c - \mathbf{C}_{(\xi_i)})\right]^{-1} = \frac{1}{i+1} \quad \text{for } i \neq 0, \tag{3.36}$$

Where the $1/(i+1)$ term comes from the coefficient before $\varepsilon^r_{ij}(\mathbf{x})$ in Eq. (3.16) (or $L^r(\mathbf{x})$ in Table 3.1). Also in Eq. (3.36), $\mathbf{C}_{(\xi_i)} = \mathbf{C}^c$ in accordance with Eq. (3.34), resulting in the cancellation of the stiffness terms. By substituting Eq. (A.4) and (3.36) into (3.30),

the expectation of strain in the *test* inclusion under weighted-mean overlapping condition becomes

$$\langle \boldsymbol{\varepsilon}^{\text{test}} \rangle = e^{-\lambda V^c} \mathbf{T}_{(\xi_0)} : \bar{\boldsymbol{\varepsilon}}^m + (\rho^c - e^{-\lambda V^c}) \mathbf{A}_{(\xi_i)} : \bar{\boldsymbol{\varepsilon}}. \tag{3.37}$$

Then, based on the definition of inclusion-wise strain in Eq. (3.13), it can be shown that

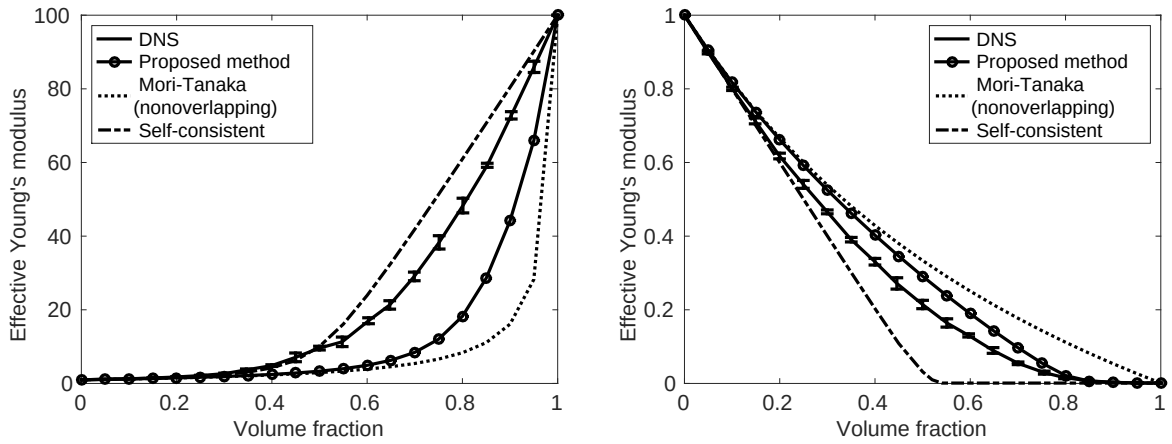

Figure 3.3. Effective Young's modulus of Boolean-Poisson model under weighted-mean overlapping conditions.

the average strain in the inclusion phase is

$$\bar{\boldsymbol{\varepsilon}}^c = \frac{\lambda V^c}{f_c} \langle \boldsymbol{\varepsilon}^{\text{test}} \rangle, \tag{3.38}$$

and Eq. (3.31) for the overall average strain becomes

$$\bar{\boldsymbol{\varepsilon}} = (1 - f_c) \bar{\boldsymbol{\varepsilon}}^m + \lambda V^c \langle \boldsymbol{\varepsilon}^{\text{test}} \rangle, \tag{3.39}$$

with the volume fraction of the inclusion phase f_c provided in Eq. (A.7). Moreover, the overall average stress defined in Eq. (3.9) can be written as

$$\bar{\boldsymbol{\sigma}} = \mathbf{C}^0 : \bar{\boldsymbol{\varepsilon}} + \lambda V^c (\mathbf{C}^c - \mathbf{C}^0) : \langle \boldsymbol{\varepsilon}^{\text{test}} \rangle. \tag{3.40}$$

Combining Eq. (3.37), (3.39) and (3.40), $\bar{\boldsymbol{\sigma}}$ can be eventually expressed as $\bar{\boldsymbol{\sigma}} = \bar{\mathbf{C}} : \bar{\boldsymbol{\varepsilon}}$. The effective stiffness tensor $\bar{\mathbf{C}}$ of the Boolean-Poisson model under weighted-mean overlapping

condition is given by

$$\bar{\mathbf{C}} = \mathbf{C}^0 + \lambda V^c(\mathbf{C}^c - \mathbf{C}^0) : \frac{\mathbf{T}_{(\xi_0)} + (\rho^c - e^{-\lambda V^c})\mathbf{A}_{(\xi_i)}}{\mathbf{I} + \lambda V^c \mathbf{T}_{(\xi_0)}} \tag{3.41}$$

with $\mathbf{T}_{(\xi_0)}$ and $\mathbf{A}_{(\xi_i)}$ defined in Eq. (3.35) and (3.34)

Results of the Boolean-Poisson model for hard inclusions and "voids" (soft inclusions) under weighted-mean overlapping condition are shown in Figure 3.3. In both situations, the effective Young's modulus vs. inclusion volume fraction curves predicted by the proposed method are bound by the Mori-Tanaka method and Hill's self-consistent method. Each DNS data point has 6 samples on a 200^3 grid. Comparing to the DNS results, the proposed method underestimates the effective Young's modulus for hard inclusions, and overestimates it for voids. In particular, the predicted modulus becomes negligible for a critical void volume fraction of $f_c \approx 0.85$ which agrees with the DNS result very well, while the self-consistent method estimates this critical volume fraction to be $f_c = 0.50$.

More importantly, the proposed method can account for the overlapping effects while the Mori-Tanaka and self-consistent methods only account for volume fraction of the inclusions phase. For example, the proposed model can account for the distribution of inclusions through the Boolean-Poisson model or a non-overlapping model; whereas, the Mori-Tanaka and self-consistent method cannot account for inclusion distributions.

2) Additive overlapping condition

For the additive overlapping condition, the material in the inclusion phase is heterogeneous, and the overall stiffness tensor is proportional to the number of inclusions involved in the overlapping. For overlapping state $\xi_i (i \neq 0)$, the overlapping stiffness tensor and the corresponding strain concentration tensor are

(3.42)

$$\mathbf{C}_{(\xi_i)} = i(\mathbf{C}^c - \mathbf{C}^0) + \mathbf{C}^0 \quad \text{and} \quad \mathbf{A}_{(\xi_i)} = \{\mathbf{I} + \bar{\mathbf{S}} : \bar{\mathbf{C}}^{-1} : \left[i(\mathbf{C}^c - \mathbf{C}^0) + \mathbf{C}^0 - \bar{\mathbf{C}}\right]\}^{-1} \quad \text{for } i \neq 0.$$

As we can see from Eq. (3.42), $\mathbf{C}_{(\xi_i)}$ and $\mathbf{A}_{(\xi_i)}$ now vary with the overlapping state ξ_i. Based on the inclusion-wise integral equation (3.22) under additive overlapping condition and Eshelby's solution for spherical inclusions, the concentration factors for different

overlapping states can be determined as

$$\mathbf{T}_{(\xi_0)} = \left[\mathbf{I} + \mathbf{S}^0 : (\mathbf{C}^0)^{-1} : (\mathbf{C}^c - \mathbf{C}^0)\right]^{-1} \tag{3.43}$$

and

$$\mathbf{T}_{(\xi_i)} = \left[\mathbf{I} + \mathbf{S}_{(\xi_i)} : \mathbf{C}^{-1}_{(\xi_i)} : (\mathbf{C}^c - \mathbf{C}^0)\right]^{-1} \quad \text{for } i \neq 0, \tag{3.44}$$

where, $\mathbf{T}_{(\xi_i)}$ depends on the overlapping state. Substituting Eq. (A.4) into (3.30) gives

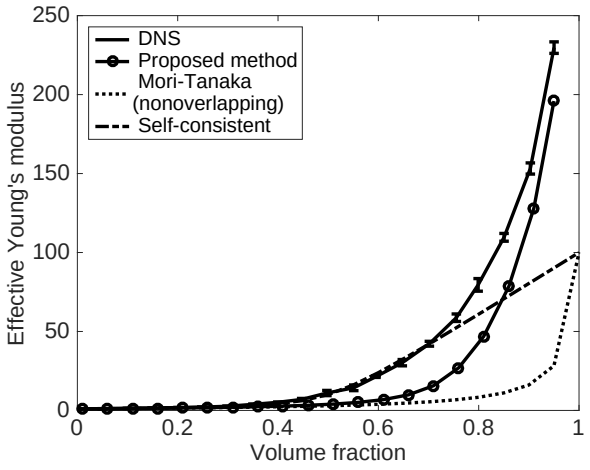

Figure 3.4. Effective Young's modulus of Boolean-Poisson model under additive overlapping condition.

the expectation of strain in the *test* inclusion under additive overlapping condition

$$\langle \boldsymbol{\varepsilon}^{\text{test}} \rangle = e^{-\lambda V^c} \left\{ \mathbf{T}_{(\xi_0)} : \bar{\boldsymbol{\varepsilon}}^m + \left[\sum_{i=1}^{\infty} \frac{(\lambda V^c)^i}{i!} \mathbf{T}_{(\xi_i)} : \mathbf{A}_{(\xi_i)} \right] : \bar{\boldsymbol{\varepsilon}} \right\}. \tag{3.45}$$

Similarly, the average strain in the inclusion phase $\bar{\boldsymbol{\varepsilon}}^c$ can be related to $\langle \boldsymbol{\varepsilon}^{\text{test}} \rangle$ through Eq. (3.20),

$$\bar{\boldsymbol{\varepsilon}}^c = \langle \boldsymbol{\varepsilon}^{\text{test}} \rangle \tag{3.46}$$

Then, the overall average strain can be expressed as

$$\bar{\boldsymbol{\varepsilon}} = (1 - f_c)\bar{\boldsymbol{\varepsilon}}^m + f_c \boldsymbol{\varepsilon}^c, \tag{3.47}$$

However, the expression of the average stress stays the same as Eq. (3.40),

$$\bar{\boldsymbol{\sigma}} = \mathbf{C}^0 : \bar{\boldsymbol{\varepsilon}} + \lambda V^c (\mathbf{C}^c - \mathbf{C}^0) : \boldsymbol{\varepsilon}^c. \tag{3.48}$$

With Eq. (3.45), (3.47) and (3.48), the effective stiffness tensor $\bar{\mathbf{C}}$ of the Boolean-Poisson model under additive overlapping condition can be calculated as

$$\bar{\mathbf{C}} = \mathbf{C}^0 + \lambda V^c (\mathbf{C}^c - \mathbf{C}^0) : \frac{\mathbf{T}_{(\xi_0)} + e^{-\lambda V^c} \sum_{i=1}^{\infty} \frac{(\lambda V^c)^i}{i!} \mathbf{T}_{(\xi_i)} : \mathbf{A}_{(\xi_i)}}{\mathbf{I} + f_c \mathbf{T}_{(\xi_0)}}, \tag{3.49}$$

where $\mathbf{T}_{(\xi_0)}$ and $\mathbf{A}_{(\xi_i)}$ are defined in Eq. (3.43) and (3.42). In Eq. (3.49), the summation on the right hand side should be truncated for numerical calculation since no simplified analytical form exists. In the following 3-D example, λV^c will go up to 5 ($f_c = 0.993$), so 25 terms will be kept in the summation to guarantee that the coefficients $(\lambda V^c)^i / i!$ of the abandoned terms are less than 1×10^{-8}.

Results of the Boolean-Poisson model for hard inclusions under the additive overlapping condition are shown in Figure 3.4. The proposed method captures the DNS trend well, especially at high volume fractions. Both the Mori-Tanaka and the self-consistent method cannot consider the additive overlapping effect, so they do not perform well at high volume fraction of the inclusion phase. However, if one switch from the original Boolean-Poisson model to a non-overlapping model, the proposed method will degrade to the Mori-Tanaka method.

3.4. Application to viscoelastic polymer nanocomposite

Nanoparticle-reinforced polymer composites have attracted intense attention in the research and industrial communities during the past decades. As the size of filler particles approaches the nano-scale, composite materials may exhibit advantageous thermal, electrical or mechanical properties, even with addition of a small amount of fillers [**3, 102**]. Because of these extraordinary behaviors, polymer nanocomposites also show promise as multi-functional materials in automotive and aerospace industries [**101**].

Many polymer fillers do not adhere to simple geometric shapes (i.e., spheres, diamonds, cylinders). Rather, fillers, such as carbon-black in tire applications, tend to have

irregular geometries and to form networks of agglomerated filler particles [**118**]. Even, more pristine filler particle structures, such as nano-diamonds, will form larger aggregates unless explicitly processed to prevent such formation [**91**].

Both experiments and molecular dynamics (MD) simulations have suggested that there exists an interphase region in the vicinity of a nanoparticle, with dramatically different thermal-mechanical, mechanical and structural properties than observed in bulk polymer [**30, 119, 65, 21**]. For example, Cheng et al. measured the modulus of confined polymer films adjacent to a plane substrate through atomic force microscopy (AFM)-based indentation, and the thickness of the interphase is found to be around several tens of nanometers [**21**]. However, directly measuring mechanical properties (e.g., dynamic moduli) of the interphase in a nanoparticle-reinforced polymer composite can be challenging and/or time-consuming. In this thesis, I am interested in using the overall mechanical properties of the polymer composite to inversely predict the interphase properties. This motivates us to develop a general homogenization method in a natural and efficient way, that allows us to consider the shape and spacial distributions of the nanoparticles, properties of the interphase and, more importantly, the effects of overlapping regions.

This section will discuss the interphase modeling of polymer nanocomposites. For this system, the inclusion is comprised of a spherical core particle (e.g., carbon or silicon nanoparticles) surrounded by an interphase region. As a result of the interaction between the polymer matrix and nanoparticles, the material properties in the interphase are different from those of the bulk polymer matrix material. The material properties are assumed to be uniform in the nanoparticle and interphase before any overlapping occurs. The stiffness tensor of the nanoparticle phase is $\mathbf{C}^{np}$, while the stiffness tensor of the interphase is $\mathbf{C}^{ip}$. The weighted-mean overlapping condition is chosen for the model. The weighting functions of the nanoparticle and interphase are denoted as η^{np} and η^{ip} respectively. Even if an interphase region overlaps with a particle, the particle properties should not be affected. To enforce this condition, η^{np} is chosen to be much larger than η^{ip},

$$\eta^{np} \gg \eta^{ip}. \tag{3.50}$$

The spacial distribution of the inclusions is chosen to follow the Poisson point process in the Boolean-Poisson model. For these distributions, the aforementioned single phase model is first extended to two phases and then is applied to viscoelastic polymer composites.

For linear viscoelastic materials, one can use the complex modulus E^* to represent the steady-state dynamic nature of the material,

$$E^*(i\omega) = E'(\omega) + iE''(\omega) = |E^*(i\omega)|e^{i\delta(\omega)}, \tag{3.51}$$

where i is the imaginary unit that satisfies $i^2 = -1$, and ω is the angular velocity. The storage modulus is given by E' and the loss modulus by E''. E' and E'' are also called the dynamic moduli of the material. The phase lag between a steady oscillating stress and strain is $\delta(\omega)$. These values are related by

$$\tan\delta(\omega) = \frac{E''(\omega)}{E'(\omega)}. \tag{3.52}$$

3.4.1. Boolean-Poisson model with two-phase inclusions

The volumes of the nanoparticle and interphase are denoted as V^{np} and V^{ip} respectively, with $V^{np} + V^{ip} = V^c$. As shown in Figure 3.5, the center of the first inclusion O_1 is inside B_0, so that its nanoparticle phase overlaps with $\mathbf{x}_0$. For the second inclusion, its center O_2 is inside B_1 so that its interphase overlaps with $\mathbf{x}_0$. For the third inclusion, its center O_3 is outside both B_0 and B_1 so that it will not influence the material properties at $\mathbf{x}_0$. Thus, the influence region with a center at the sampling point $\mathbf{x}_0$ can now be divided into a sphere with volume V^{np} (region B_0) and a thick shell with volume V^{ip} (region B_1). If the center of an inclusion is inside B_0, its nanoparticle phase will overlap with the sampling point. Because the weighting function of the nanoparticle phase is much larger than that of the interphase, the corresponding stiffness tensor $\mathbf{C}_{(\xi_i)} = \mathbf{C}^{np}$ at the sampling point. If the center of the inclusion is inside B_1, its interphase will overlap with the sampling point. However, $\mathbf{C}_{(\xi_i)} = \mathbf{C}^{ip}$ only occurs when centers of all the other inclusions are outside B_0, and this state has a conditional probability equal to $e^{-\lambda V^{np}}$. Finally, if an inclusion center is neither in B_0 nor in B_1, the inclusion will not overlap with the sampling point, and

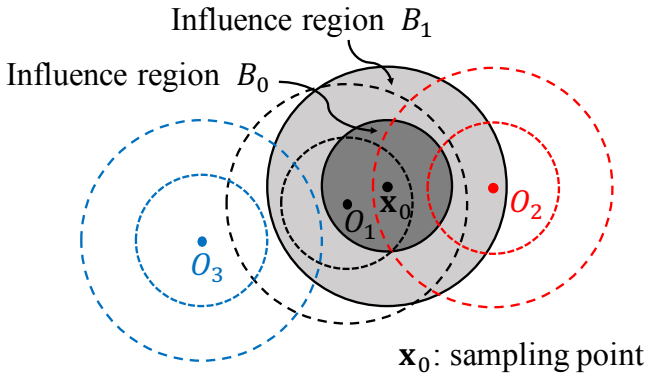

Figure 3.5. Illustration of the influence region B_0 centering at the sampling point $\mathbf{x}_0$.

the properties at the sampling point will remain unaltered as the matrix material. By taking all the possible situations into account, one can divide the sampling space Ξ into three subsets based on the material properties at the sampling point as shown in Figure 3.6. Set Ξ_{ip} includes the states when $\mathbf{C}_{(\xi_i)} = \mathbf{C}^{ip}$, and Set Ξ_{np} includes the states when $\mathbf{C}_{(\xi_i)} = \mathbf{C}^{np}$.

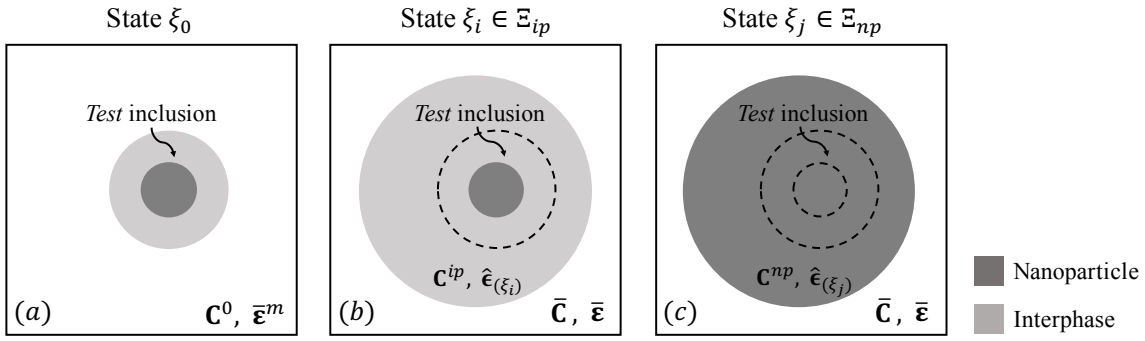

Figure 3.6. Illustration of the physical models of the two-phase inclusion under different overlapping states.

After calculating the probability function of each state using Eq. (A.2), the volume fractions of the nanoparticle phase f_{np} and interphase f_{ip} can be derived as

$$f_{np} = 1 - e^{-\lambda V^{np}}, \quad f_{ip} = e^{-\lambda V^{np}} \left[1 - e^{-\lambda V^{ip}}\right] \tag{3.53}$$

For mechanical properties, Eshelby's solution of spherical inclusion [**32**] and Tanaka-Mori's theorem [**95**] can be directly applied to model in Figure 3.6(b) and 3.6(c). However, due to the interphase effects, for the model in Figure 3.6(a), there exists no closed-form solution for inclusion strain, and strains in the nanoparticle phase and interphase become non-uniform. I adopt the assumption in [**96**] that the strains are uniform in the nanoparticle and interphase, so that Eshelby's solution is applicable. While this assumption loses some accuracy in representing the spatial variation of strain in inclusions, it is believed that these spatial variations should have a minor effect on the effective properties. However, if these spatial variations are needed, the inclusion could be discretized as in [**71**]. By taking all overlapping states into account, one can get the expected values of the strain $\langle \boldsymbol{\varepsilon}_{np}^{\text{test}} \rangle$ in the nanoparticle phase and $\langle \boldsymbol{\varepsilon}_{ip}^{\text{test}} \rangle$ in the interphase of the test inclusion (see Eq. (C.1) and (C.2)). In order to close the scheme, the equations of average strain and stress are needed, which are given as

$$\bar{\boldsymbol{\varepsilon}} = (1 - f_{np} - f_{ip})\bar{\boldsymbol{\varepsilon}}^m + \lambda \left(V^{np} \langle \boldsymbol{\varepsilon}_{np}^{\text{test}} \rangle + V^{ip} \langle \boldsymbol{\varepsilon}_{ip}^{\text{test}} \rangle \right), \tag{3.54}$$

and

$$\bar{\boldsymbol{\sigma}} = \mathbf{C}^0 : \bar{\boldsymbol{\varepsilon}} + \lambda \left(V^{np} \delta \mathbf{C}^{np} : \langle \boldsymbol{\varepsilon}_{np}^{\text{test}} \rangle + V^{ip} \delta \mathbf{C}^{ip} : \langle \boldsymbol{\varepsilon}_{ip}^{\text{test}} \rangle \right), \tag{3.55}$$

where $\langle \boldsymbol{\varepsilon}^{np} \rangle$ and $\langle \boldsymbol{\varepsilon}^{ip} \rangle$ are the expectations of strain in the nanoparticle phase and interphase respectively.

Finally, the effective stiffness tensor $\bar{\mathbf{C}}$ of the Boolean-Poisson model with two-phase inclusions can be expressed as

$$\bar{\mathbf{C}} = \mathbf{C}^0 + \lambda \left(V^{np} \delta \mathbf{C}^{np} : \langle \mathbf{A}^{np} \rangle + V^{ip} \delta \mathbf{C}^{ip} : \langle \mathbf{A}^{ip} \rangle \right), \tag{3.56}$$

where $\langle \mathbf{A}^{np} \rangle$ and $\langle \mathbf{A}^{ip} \rangle$ are defined in Eq. (C.8). More detailed derivations are provided in Appendix C.

3.4.2. Inverse modeling of interphase properties

Next, I will demonstrate how to combine our micromechanics model with experimental data from a composite to approximate the interphase properties in 3-D. The experimental data of carbon-black filled styrene butadiene rubbers with various volume fractions of fillers (0%, 2.4%, 13.0%, 16.7%, 20.0% and 23.0%) from Diani's paper [**27**] is used, where 0% filler represents the matrix properties. Dynamic mechanical analysis (DMA) was used to experimentally characterize the linear viscoelasticity of each material, and the master curves of the storage modulus E' and loss modulus E'' were reconstructed at a reference temperature 0°C. The matrix and interphase are considered nearly incompressible with Poisson's ratios of $\nu_0 = 0.499$ and $\nu_{ip} = 0.499$ respectively. The Young's modulus and Poisson's ratio of the nanoparticle material (carbon-black) are $E_{np} = 30$ GPa and $\nu_{np} = 0.19$ respectively. The complex modulus and thickness of the interphase are assumed to be independent of the volume fraction of nanoparticles.

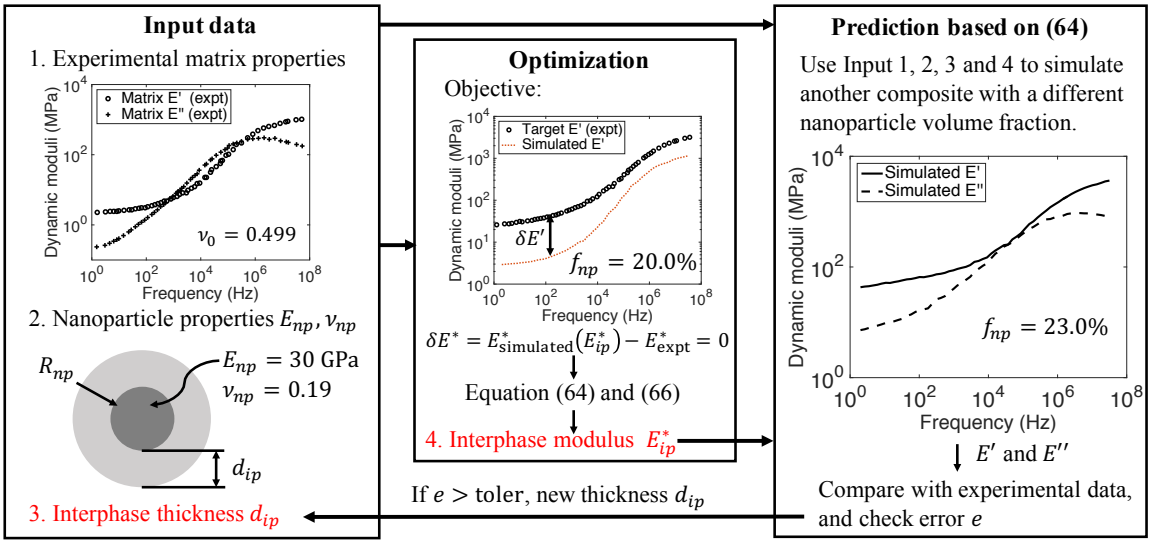

Figure 3.7. Flowchart summarizing the inverse modeling of interphase properties.

A flowchart describing the inverse modeling of interphase properties is provided in Figure 3.7. For a given interphase thickness d_{ip}, together with the known properties of the matrix and nanoparticle materials, the effective complex modulus of a simulated

composite $E^*_{\text{simulated}}$ is only a function of the interphase's complex modulus E^*_{ip}, based on Eq. (3.56). As shown in the "Optimization" box, the objective is to find the optimum interphase complex modulus that minimizes the difference between the simulated effective modulus $E^*_{\text{simulated}}(E^*_{ip})$ and the experimentally measured value E^*_{expt} for the same composite material. Since no constraint is put on the interphase properties in our current work, the optimization problem becomes a root-finding exercise, which solves for E^*_{ip} such that

$$\delta E^* = E^*_{\text{simulated}}(E^*_{ip}) - E^*_{expt} = 0 \quad \text{at each frequency point.} \tag{3.57}$$

The experimental data for nanoparticle volume fraction 20% is chosen as the reference for E^*_{expt}. In order to solve Eq. (3.57), the secant method is used to search for the complex modulus of the interphase at every frequency point. The recurrence relation using the secant method can be written as

$$E^*_{ip}[n] = E^*_{ip}[n-1] - \delta E^*[n-1]\frac{E^*_{ip}[n-1] - E^*_{ip}[n-2]}{\delta E^*[n-1] - \delta E^*[n-2]}, \tag{3.58}$$

where n denotes the iteration number. One will continue this process until a sufficiently high level of accuracy is reached with respect to the experimental results for the composite modulus. After obtaining the interphase modulus E^*_{ip}, one can calculate the effective properties of another composite with a different amount of fillers (specifically compared to a volume fraction 23%). By comparing these predictions with experimental data, one can evaluate whether the choice of the interphase thickness (d_{ip}) is physical.

Using the procedure in Figure 3.7, the interphase thickness (d_{ip}) is found to be in the range

$$d_{ip} = 0.60R_{np} \quad \text{to} \quad 0.65R_{np}, \tag{3.59}$$

which gives converged interphase modulus, as well as accurate predictions of the effective dynamic moduli within the whole frequency range ($1 - 10^8$ Hz). For typical nanoparticles with radius $R_{np} = 30$ nm, the interphase thickness is around $18 - 20$ nm, which is realistic

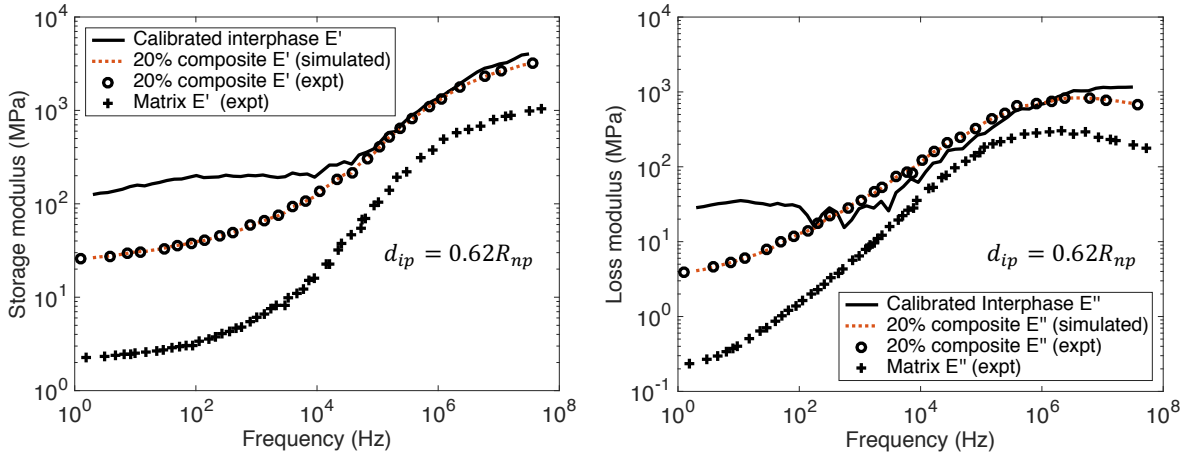

Figure 3.8. Predicted interphase's storage modulus (Left) and loss modulus (Right).

according to AFM nano-indentation experiments in [**21**]. In this section, I will show the results for $d_{ip} = 0.62R_{np}$.

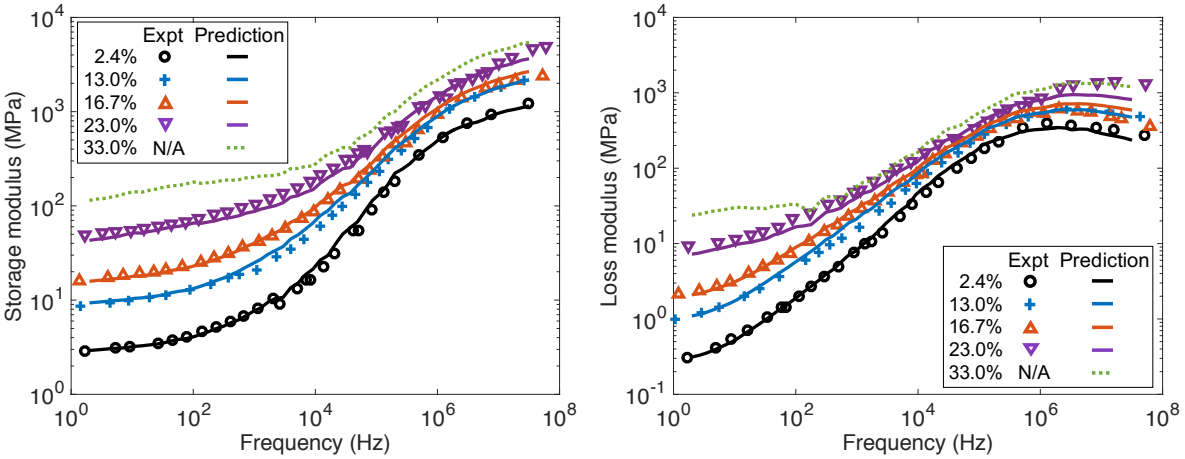

Figure 3.9. Experimental validation of the inversely predicted interphase properties for nanoparticle volume fraction 2.4%, 13.0% and 16.7%.

The predicted dynamic moduli of the interphase are shown in Figure 3.8 together with those of the matrix material. As we can see from the figure, the dynamic moduli of the interphase is higher than the dynamic moduli of the matrix across the whole frequency range due to the presence of polymer-nanoparticle interaction. Also the ratio

of interphase dynamic moduli to the dynamic moduli of bulk matrix is larger in the lower frequency (higher temperature) domain, indicating a stronger effect of polymer-nanoparticle interaction.

Furthermore, the predicted dynamic moduli and the choice of the interphase thickness are validated against experimental data with nanoparticle volume fraction 2.4%, 13.0% and 16.7%. As we can see from Figure 3.9, the experimental data agrees well with the predictions of the extended micromechanics method across the whole frequency range. Since our model's interphase properties and thickness were predicted with one set of filler volume fractions (20% and 23%) and – using these interphase properties – the model showed agreement for a different set of volume fractions (2.4%, 13.0% and 16.7%), it is suggested by our proposed method that the amount of nanoparticles has little influence on interphase properties.

CHAPTER 4

Data-driven Homogenization: Self-consistent Clustering Analysis

Analytical micromechanicsl methods [**32, 46, 48, 71, 72**] are very efficient because they describe the heterogeneous material by several microstructural descriptors, rather than considering the whole RVE explicitly. However, they are based on mean-field assumptions and linear superposition, which usually only provide a rough estimated solution of the Lippmann-Schwinger equation. This limits their application to materials with complex microstructure and localized nonlinear behavior where plasticity is present.

In order to consider the complex interaction within arbitrary microstructure, the starting point of material homogenization is a high-fidelity Representative Volume Element (RVE) of the material, i.e. a representative domain of the microstructure of a material. This high-fidelity RVE can be analyzed by different methods, e.g. fast-Fourier transformation based micromechanics method [**93**], such that accurate predictions of the material's mechanical behavior are achieved. However, the computational cost associated with these RVEs is usually significantly large because they involve a very fine numerical discretization to capture the microstructural shapes of the material and its detailed mechanical behavior. In this chapter, a data-driven reduced-order homogenization method called self-consistent clustering analysis (SCA) is developed [**70**], which enables both accuracy and efficiency by integrating advanced data clustering techniques and micromechanics theories.

4.1. Discretization of the Lippmann-Schwinger equation

With the aim of lowering the computational expenses one may consider decomposing the high-fidelity RVE into a group of large subdomains, obtaining a reduced RVE – Figure 4.1. These subdomains are designated as **material clusters** henceforth. However, if one

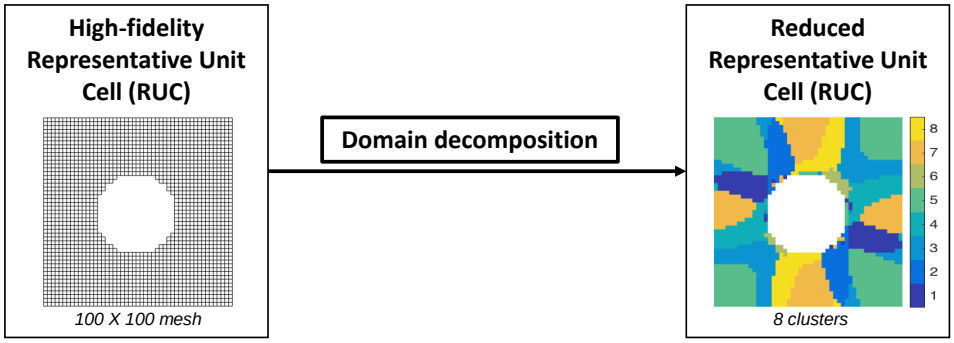

Figure 4.1. Illustration of arbitrary domain decomposition for a high-fidelity RVE.

uses the same analysis method considered for the high-fidelity RVE, the resolution for the analysis is degraded, and the accuracy of the predictions decreases. For example, if using the finite element method, the larger subdomains (material clusters) would have to correspond to larger finite elements, introducing limitations in the shape of these clusters and the accuracy of the solution. The procedure used to determine these material clusters will be introduced later in Section 4.2. In addition, assume that *every local variable* $\boldsymbol{\beta}_m(\boldsymbol{x})$ *within each material cluster is uniform.* This is equivalent to considering a piecewise uniform approximation to the local variables of interest in the RVE:

$$\boldsymbol{\beta}_m(\mathbf{x}) = \sum_{I=1}^{k} \boldsymbol{\beta}_m^I \chi^I(\mathbf{x}), \tag{4.1}$$

where $\boldsymbol{\beta}_m^I$ is the homogeneous variable in the I-th material cluster and $\chi^I(\mathbf{x})$ is the characteristic function in the domain of the I-th material cluster Ω^I, defined as

$$\chi^I(\mathbf{x}) = \begin{cases} 1 & \text{if } x \in \Omega^I \\ 0 & \text{otherwise} \end{cases} \tag{4.2}$$

from which the following cluster averaging relationship can be written,

$$\int_{\Omega} \chi^I(\mathbf{x})[\bullet] d\mathbf{x} \equiv \int_{\Omega^I} [\bullet] d\mathbf{x} \tag{4.3}$$

where $[\bullet]$ signifies any quantity of interest to be averaged in the cluster domain Ω^I.

Remark 1. *Starting from this chapter, the subscript* $\square_m$ *denotes a microscopic or local quantity in the RVE. For example,* $\boldsymbol{\varepsilon}_m$ *represents the microscopic strain. Moreover, the subscript* $\square_M$ *denotes a macroscopic quantity in the RVE.*

Under these assumptions, a system of equations can be derived by successively homogenizing each material cluster via the Lippmann-Schwinger equation, the Lippmann-Schwinger equation is averaged for **each** cluster:

$$\begin{aligned}(4.4)\qquad &\frac{1}{c^I \mid \Omega \mid}\int_\Omega \chi^I(\mathbf{x})\Delta\boldsymbol{\varepsilon}_m(\mathbf{x})d\mathbf{x}\\ &+\frac{1}{c^I \mid \Omega \mid}\int_\Omega\int_\Omega \chi^I(\mathbf{x})\boldsymbol{\Phi}^0(\mathbf{x},\mathbf{x}') : \left[\Delta\boldsymbol{\sigma}_m(\mathbf{x}') - \mathbf{C}^0 : \Delta\boldsymbol{\varepsilon}_m(\mathbf{x}')\right] d\mathbf{x}'d\mathbf{x} - \Delta\boldsymbol{\varepsilon}^0 = 0,\end{aligned}$$

where this equation follows directly from averaging the original integral equation within the I-th cluster, and where the first term corresponds to $\Delta\boldsymbol{\varepsilon}_m^I$. Moreover, recalling the piecewise uniform assumption of all the local variables, Eq. (4.1),

$$(4.5)\qquad \Delta\boldsymbol{\varepsilon}_m(\mathbf{x}) = \sum_{J=1}^{k}\chi^J(\mathbf{x})\Delta\boldsymbol{\varepsilon}_m^J, \quad \Delta\boldsymbol{\sigma}_m(\mathbf{x}) = \sum_{J=1}^{k}\chi^J(\mathbf{x})\Delta\boldsymbol{\sigma}_m^J$$

where $\Delta\boldsymbol{\varepsilon}_m^J$ and $\Delta\boldsymbol{\sigma}_m^J$ are the incremental stain and stress in the J-th cluster. Hence, Eq. (4.4) can be simplified according to these relations as,

$$\begin{aligned}(4.6)\qquad &\Delta\boldsymbol{\varepsilon}_m^I + \sum_{J=1}^{k}\left[\frac{1}{c^I \mid \Omega \mid}\int_\Omega\int_\Omega \chi^I(\mathbf{x})\chi^J(\mathbf{x}')\boldsymbol{\Phi}^0(\mathbf{x},\mathbf{x}')d\mathbf{x}'d\mathbf{x}\right] : \left[\Delta\boldsymbol{\sigma}_m^J - \mathbf{C}^0 : \Delta\boldsymbol{\varepsilon}_m^J\right]\\ &-\Delta\boldsymbol{\varepsilon}^0 = 0.\end{aligned}$$

where the term within brackets is a well-defined quantity in micromechanical analysis of materials: the interaction tensor $\mathbf{D}^{IJ}$,

$$(4.7)\qquad \mathbf{D}^{IJ} = \frac{1}{c^I \mid \Omega \mid}\int_\Omega\int_\Omega \chi^I(\mathbf{x})\chi^J(\mathbf{x}')\boldsymbol{\Phi}^0(\mathbf{x},\mathbf{x}')d\mathbf{x}'d\mathbf{x},$$

written as an integral of Green's function $\boldsymbol{\Phi}^0(\mathbf{x},\mathbf{x}')$ in an RVE domain Ω with periodic boundary conditions, and where c^I is the volume fraction of the I-th cluster and $\mid \Omega \mid$ is the volume of domain Ω.

Eq. (4.4) can then be re-written considering Eq. (4.7) as

$$\Delta\boldsymbol{\varepsilon}_m^I + \sum_{J=1}^{k} \mathbf{D}^{IJ} : \left[\Delta\boldsymbol{\sigma}_m^J - \mathbf{C}^0 : \Delta\boldsymbol{\varepsilon}_m^J\right] - \Delta\boldsymbol{\varepsilon}^0 = \mathbf{0}. \tag{4.8}$$

After the discretization, the far field strain is still equal to the average strain in the RVE,

$$\Delta\boldsymbol{\varepsilon}^0 = \sum_{I=1}^{k} c^I \Delta\boldsymbol{\varepsilon}_m^I. \tag{4.9}$$

Meanwhile, the macroscopic boundary conditions are also required to be discretized. For instance, the discrete form of the macro-strain constraint can be written as

$$\sum_{I=1}^{k} c^I \Delta\boldsymbol{\varepsilon}_m^I = \Delta\boldsymbol{\varepsilon}_M \quad \text{or} \quad \Delta\boldsymbol{\varepsilon}^0 = \Delta\boldsymbol{\varepsilon}_M. \tag{4.10}$$

Similarly, the discretized macro-stress constraint becomes

$$\sum_{I=1}^{k} c^I \Delta\boldsymbol{\sigma}_m^I = \Delta\boldsymbol{\sigma}_M. \tag{4.11}$$

Also note that the separate averaging of the Lippmann-Schwinger equation introduced in this section implies that stresses in adjacent clusters are not enforced to be continuous, but the global average of the local strains and stresses are constrained to coincide with the macroscopic applied strain or stress. In a way, this is similar to what happens in the finite element discretization of the conservation of linear momentum equation where the continuity of stresses is also not enforced between adjacent elements, but global equilibrium is satisfied.

An important feature of the continuous Lippmann-Schwinger equation is that its solution is independent of the choice of the reference material $\mathbf{C}^0$. This can be explained by the fact that the physical problem is fully described by the equilibrium condition and the prescribed macroscopic boundary conditions. However, once the equation is discretized based on the piecewise uniform assumption, the equilibrium condition is not strictly satisfied at every point in the RVE, and the solution of the reduced system depends on the choices of $\mathbf{C}^0$. This discrepancy can be reduced by increasing the number of clusters

into the system, but with a computational cost increase due to the increased degrees of freedom. To improve the accuracy, a self-consistent scheme is proposed to correct the reference material during the online prediction stage. The combination of the offline determination of material clusters and the online self-consistent scheme gives the so-called Self-consistent Clustering Analysis (SCA).

4.2. Offline-stage

Grouping material points with similar mechanical behavior into a single cluster is performed by domain decomposition of the material points using the clustering methods [**76**]. First, the similarity between two material points is measured by the strain concentration tensor $\mathbf{A}_m(\mathbf{x})$, which is defined as

$$\boldsymbol{\varepsilon}_m(\mathbf{x}) = \mathbf{A}_m(\mathbf{x}) : \boldsymbol{\varepsilon}_M \quad \text{in } \Omega, \tag{4.12}$$

where $\boldsymbol{\varepsilon}_M$ is the elastic macroscopic strain corresponding to the boundary conditions on the RVE, and $\boldsymbol{\varepsilon}_m(\mathbf{x})$ is the elastic local strain at point $\mathbf{x}$ in the microscale RVE domain Ω. For a linear elastic material, the strain concentration tensor is independent of the loading conditions. Other metrics such as effective plastic strain and damage indicators can also be selected as the offline data, but may require extra computation in the offline stage.

For a 2-dimensional (2D) material, the strain concentration tensor $\mathbf{A}_m(\mathbf{x})$ in each material point has 9 independent components which are determined by direct numerical simulation (DNS) of the high-fidelity RVE under 3 orthogonal loading conditions. While for a 3-dimensional (3D) material, $\mathbf{A}(\mathbf{x})$ has 36 independent components, needing a set of DNS under 6 orthogonal loading conditions. The format of the raw data for a 2D material is shown in Figure 4.2. The dimension of the data is 9 in the 2D case, and N is the total number of discretization points in the DNS. For example, if the high-fidelity RVE is discretized by a 600×600 finite element mesh with reduced integration elements, then N is equal to 3.6×10^5.

After computing the strain concentration tensor $\mathbf{A}_m(\mathbf{x})$, the k-means clustering method [**122**] is used to group data points. Additional details about the clustering algorithm are provided in Appendix D. Since all the material points in a cluster are assumed to have

DataIndex	A_{11}	A_{22}	A_{33}	A_{12}	A_{21}	A_{23}	A_{32}	A_{13}	A_{31}
1	–	–	–	–	–	–	–	–	–
2	–	–	–	–	–	–	–	–	–
⋮			⋮			⋮			⋮
N	–	–	–	–	–	–	–	–	–

Figure 4.2. 2D Data format based on the strain concentration tensor.

the same mechanical responses, the number of the degrees of freedom is significantly reduced through this compression/clustering step. The k-means clustering results of 2D heterogeneous RVEs with different microstructure at two levels of resolution are provided in Figure 4.3.

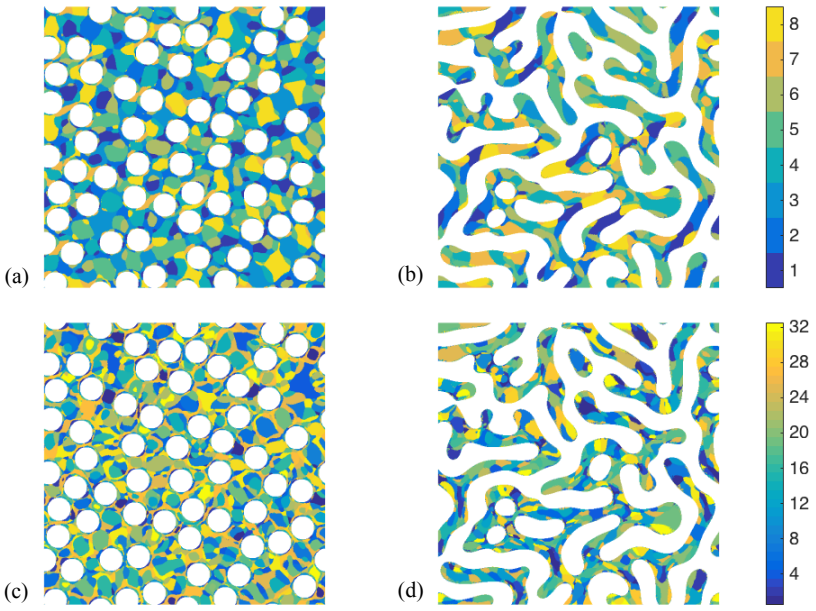

Figure 4.3. 2D clustering results of a fiber-reinforced composite and amorphous material.

Figure 4.3a) and b) show the reduced RVE domain decomposition considering only 8 clusters for the matrix phase, while figures c) and d) were obtained considering 32 clusters for the same phase. Regions with the same color represent the same cluster. In Figure

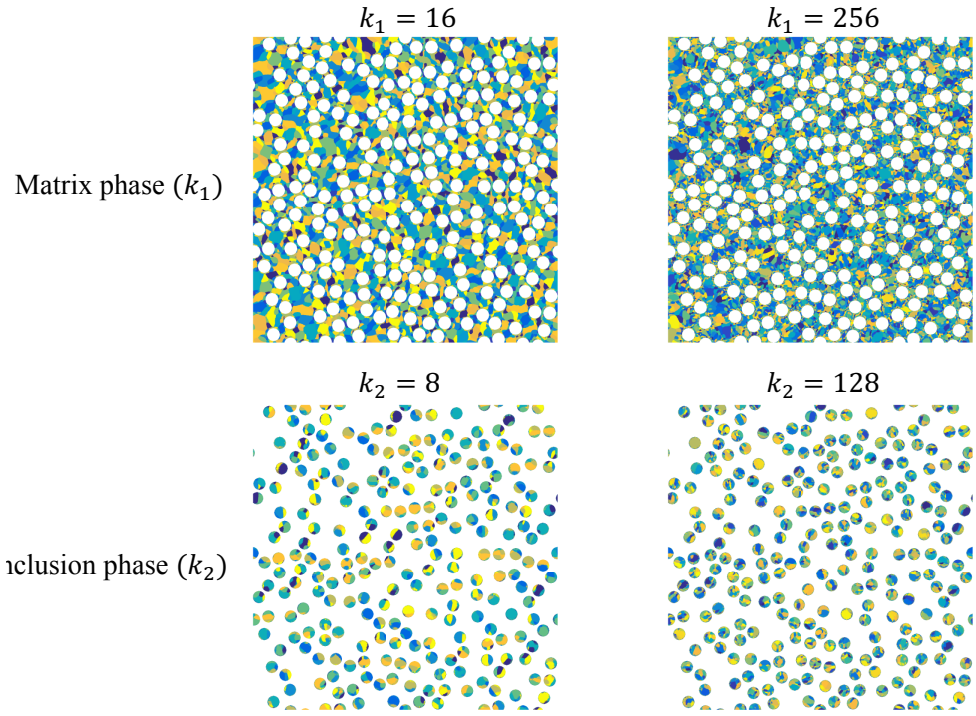

Figure 4.4. 2D clustering results for a larger FEM mesh 1200×1200.

4.4, clustering results for both matrix and inclusion phase are provided, and a larger FEM mesh is also used in the offline stage. Moreover, clustering results of a 3D composite with identical spherical inclusions embedded in the matrix are shown in Figure 4.5. Recall that the methodology proposed in this work assumes that the local variables in each cluster are uniform. Therefore, in this example, the finite element mesh of the high-fidelity RVE that had three hundred and sixty thousand elements was reduced to a few clusters (8 or 32) that can be used to solve the system of equations. This represents an extensive data compression that is expected to lead to tremendous computational savings in the posterior online stage.

In the discretized/reduced Lippmann-Schwinger equation, one can utilize the piecewise uniform assumption to extract the interaction tensor $\mathbf{D}^{IJ}$, which represents the influence of the stress in the J-th cluster on the strain in the I-th cluster [**70**]. In a periodic RVE domain Ω, the interaction tensor can be written as a convolution of the Green's function

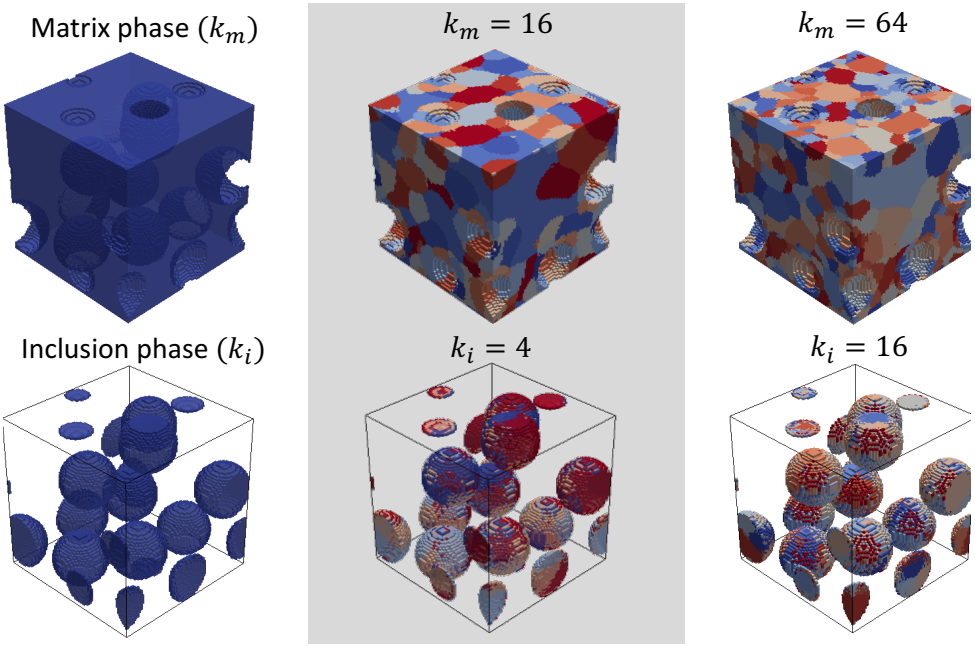

Figure 4.5. 3D clustering results of a matrix-inclusion composite with a FEM mesh $80 \times 80 \times 80$.

and the characteristic functions,

$$\mathbf{D}^{IJ} = \frac{1}{c^I \mid \Omega \mid} \int_\Omega \int_\Omega \chi^I(\mathbf{x}) \chi^J(\mathbf{x}') \mathbf{\Phi}^0(\mathbf{x}, \mathbf{x}') d\mathbf{x}' d\mathbf{x}, \tag{4.13}$$

where c^I is the volume fraction of the I-th cluster, and $\mid \Omega \mid$ is the volume of the RVE domain. $\mathbf{\Phi}^0(\mathbf{x}, \mathbf{x}')$ is the fourth-order periodic Green's function associated with an isotropic linear elastic reference material, and its stiffness tensor is $\mathbf{C}^0$. This reference material is introduced in the online stage as a homogeneous media to formulate the Lippmann-Schwinger integral equation. With the periodicity of the RVE, $\mathbf{\Phi}^0(\mathbf{x}, \mathbf{x}')$ takes a simple form for isotropic materials in the frequency domain as shown in Chapter 2,

$$\hat{\mathbf{\Phi}}^0(\boldsymbol{\xi}) = \frac{1}{4\mu^0} \hat{\mathbf{\Phi}}^1(\boldsymbol{\xi}) + \frac{\lambda^0 + \mu^0}{\mu^0(\lambda^0 + 2\mu^0)} \hat{\mathbf{\Phi}}^2(\boldsymbol{\xi}), \tag{4.14}$$

with

$$\hat{\Phi}^1_{ijkl}(\boldsymbol{\xi}) = \frac{1}{|\ \boldsymbol{\xi}\ |^2}\left(\delta_{ik}\xi_j\xi_l + \delta_{il}\xi_j\xi_k + \delta_{jl}\xi_i\xi_k + \delta_{jk}\xi_i\xi_l\right) \tag{4.15}$$

$$\hat{\Phi}^2_{ijkl}(\boldsymbol{\xi}) = -\frac{\xi_i\xi_j\xi_k\xi_l}{|\ \boldsymbol{\xi}\ |^4}, \tag{4.16}$$

where $\boldsymbol{\xi}$ is the coordinate in Fourier space corresponding to $\mathbf{x}$ in real space, and δ_{ij} is the Kronecker delta function. λ^0 and μ^0 are Lamé constants of the reference material. The expression of $\hat{\Phi}^0_{ijkl}(\boldsymbol{\xi})$ is not well defined at frequency point $\boldsymbol{\xi} = \mathbf{0}$. However, imposing by the boundary conditions for deriving the Green's function, a uniformly distributed polarization stress field will not induce any strain field inside the RVE, which indicates

$$\hat{\Phi}^0_{ijkl}(\boldsymbol{\xi} = \mathbf{0}) = \mathbf{0}. \tag{4.17}$$

Based on Eq. (4.14), the convolution term in the spacial domain in Eq. (4.13) can be translated into a direct multiplication at each point $\boldsymbol{\xi}$ in the frequency domain using a Fourier transformation,

$$\bar{\boldsymbol{\Phi}}^0_J(\mathbf{x}) = \int_\Omega \chi^J(\mathbf{x}')\boldsymbol{\Phi}^0(\mathbf{x},\mathbf{x}')d\mathbf{x}' = \mathscr{F}^{-1}\left(\hat{\chi}^J(\boldsymbol{\xi})\hat{\boldsymbol{\Phi}}^0(\boldsymbol{\xi})\right). \tag{4.18}$$

As we can see from Eq. (4.15) and (4.16), $\hat{\boldsymbol{\Phi}}^1(\boldsymbol{\xi})$ and $\hat{\boldsymbol{\Phi}}^2(\boldsymbol{\xi})$ are independent of the material properties, so that they can be computed for one time only in the offline stage. If the reference material is changed in the self-consistent scheme at the online stage, only the coefficients relating to its Lamé constants in Eq. (4.14) need to be updated.

4.3. Online-stage

To achieve both efficiency and accuracy, I propose to use a self-consistent scheme in the online stage, which shows good accuracy with less number of clusters. In the self-consistent scheme, the stiffness tensor of the reference material $\mathbf{C}^0$ is set approximately same as the homogenized stiffness tensor $\bar{\mathbf{C}}$ of the whole RVE,

$$\mathbf{C}^0 \to \bar{\mathbf{C}}. \tag{4.19}$$

The idea of the self-consistent scheme originates from the self-consistent method in classical micromechanics [**48**], where a representative inclusion is assumed to be embedded in a effective medium. The self-consistent scheme proposed here plays a very similar role as the self-consistent method, and it is more accurate for a material/RVE with more disordered microstructural morphology. For a multi-phase material with a phase that dominates the material property, such as matrix with densely embedded non-overlapping inclusions, the self-consistent scheme in Eq. (4.19) may not be a good choice. In those cases, it is better to approximate the reference material in the same manner as the effective stiffness tensor $\bar{\mathbf{C}}^*$ in the dominating phase/Matrix,

$$\mathbf{C}^0 \to \bar{\mathbf{C}}^*. \tag{4.20}$$

The homogenized stiffness tensor $\bar{\mathbf{C}}$ of the RVE can be expressed as

$$\bar{\mathbf{C}} = \sum_{I=1}^{k} c^I \mathbf{C}^I_{\text{alg}} : \mathbf{A}^I_m, \tag{4.21}$$

where $\mathbf{C}^I_{\text{alg}}$ is the algorithm stiffness tensor of the material in the I-th cluster and is an output of the local constitutive law for the current strain increment in the cluster,

$$\mathbf{C}^I_{\text{alg}} = \frac{\partial \Delta \boldsymbol{\sigma}^I_m}{\partial \Delta \boldsymbol{\varepsilon}^I_m} \tag{4.22}$$

The strain concentration tensor of the I-th cluster $\mathbf{A}^I_m$ relates the local strain increment in the I-th cluster $\Delta\boldsymbol{\varepsilon}^I_m$ to the far-field strain increment $\Delta\boldsymbol{\varepsilon}^0$,

$$\Delta \boldsymbol{\varepsilon}^I_m = \mathbf{A}^I_m : \Delta \boldsymbol{\varepsilon}^0. \tag{4.23}$$

The strain concentration tensor $\mathbf{A}^I_m$ can be determined by first linearizing the discretized integral equation (4.8) using $\mathbf{C}^I_{\text{alg}}$ and then inversing the Jacobian matrix from the Newton's method. Since $\bar{\mathbf{C}}$ is only required for the self-consistent scheme, the calculation $\bar{\mathbf{C}}$ is performed once after the convergence of the Newton's method to save the computational cost. Similarly, the effective stiffness tensor $\bar{\mathbf{C}}^*$ in the dominating phase/matrix can be

calculated as

$$\bar{\mathbf{C}}^* = \left(\sum_I^{k^*} c^I \mathbf{A}_m^I \right)^{-1} : \sum_I^{k^*} c^I \mathbf{C}_{\text{alg}}^I : \mathbf{A}_m^I, \tag{4.24}$$

where k^* represents the clusters inside the dominating phase/matrix.

Due to the nonlinearity of the material responses, such as plasticity, it is usually not possible to determine an isotropic $\mathbf{C}^0$ which provides an exact match with $\bar{\mathbf{C}}$. Here, two types of self-consistent schemes have been proposed to approximate Eq. (4.19): 1) linear regression of average strain increment $\Delta\bar{\boldsymbol{\varepsilon}}$ and stress increment $\Delta\bar{\boldsymbol{\sigma}}$ (or regression-based scheme) and 2) isotropic projection of the effective stiffness tensor $\bar{\mathbf{C}}$ (or projection-based scheme).

In the regression-based scheme [**71**], the self-consistent scheme is formulated as an optimization problem: the goal is to find an isotropic $\mathbf{C}^0$ that minimizes the error between the predicted average stress increments. The inputs of the regression algorithm are the average strain increment $\Delta\bar{\boldsymbol{\varepsilon}}$ and stress increment $\Delta\bar{\boldsymbol{\sigma}}$, which are computed as

$$\Delta\boldsymbol{\varepsilon}_M = \sum_{I=1}^{k} c^I \Delta\boldsymbol{\varepsilon}_m^I \quad \text{and} \quad \Delta\boldsymbol{\sigma}_M = \sum_{I=1}^{k} c^I \Delta\boldsymbol{\sigma}_m^I \tag{4.25}$$

The objective of the regression-based scheme is to find the λ^0 and μ^0 of the reference material by computing

$$\left\{\lambda^0, \mu^0\right\} = \underset{\{\lambda', \mu'\}}{\operatorname{argmin}} \; ||\Delta\boldsymbol{\sigma}_M - \mathbf{f}(\lambda', \mu') : \Delta\boldsymbol{\varepsilon}_M||^2, \tag{4.26}$$

where $||\mathbf{Z}||^2 = \mathbf{Z} : \mathbf{Z}$ for an arbitrary second-order tensor $\mathbf{Z}$. The function $\mathbf{f}(\lambda', \mu')$ can be expressed as

$$\mathbf{f}(\lambda', \mu') = \lambda' \mathbf{I} \otimes \mathbf{I} + \mu' \mathbf{II}. \tag{4.27}$$

where $\mathbf{I}$ is the second-rank identity tensor, and $\mathbf{II}$ is the symmetric part of the fourth-rank identity tensor. Equivalently, the cost function $g(\lambda', \mu')$ of the optimization problem can be written as

$$g(\lambda', \mu') = ||\Delta\boldsymbol{\sigma}_M - \mathbf{f}(\lambda', \mu') : \Delta\boldsymbol{\varepsilon}_M||^2. \tag{4.28}$$

The optimum point is found via the respective partial derivatives of the cost function,

$$\left.\frac{\partial g}{\partial \lambda'}\right|_{\lambda^0,\mu^0} = 0 \quad \text{and} \quad \left.\frac{\partial g}{\partial \mu'}\right|_{\lambda^0,\mu^0} = 0, \tag{4.29}$$

which forms a system of two linear equations in terms of the Lamé constants. The system always has a unique solution except under a pure-shear loading condition, where λ^0 is under-determined. In this case, the value of λ^0 is not updated. Additionally, $g\left(\lambda^0, \mu^0\right)$ vanishes when the effective macroscopic homogeneous material is also isotropic linear elastic.

Although this scheme does not require computing $\bar{\mathbf{C}}$ explicitly, it has mainly two drawbacks. First, the optimization problem is under-determined under pure shear or hydrostatic loading conditions, so that one of two independent elastic constants needs to be estimated. More importantly, the modulus of the optimum reference material may become negative under complex loading conditions, which is deleterious to the convergence of the fixed-point method.

To resolve the problems in the regression-based scheme, a new self-consistent scheme is proposed based on projection of the effective stiffness tensor $\bar{\mathbf{C}}$, which is formulated as two well-defined optimization problems. For a 2D plane strain problem, the stiffness tensor of the isotropic reference material $\mathbf{C}^0_{pe}$ is decomposed as

$$\mathbf{C}^0_{iso} = 2\kappa^0 \mathbf{J} + 2\mu^0 \mathbf{K}, \tag{4.30}$$

where the 2D bulk modulus can be related to the Lamé parameters,

$$\kappa^0 = \lambda^0 + \mu^0. \tag{4.31}$$

The fourth-rank tensor $\mathbf{J}$ and $\mathbf{K}$ are defined as

$$\mathbf{J} = \frac{1}{2}\left(\mathbf{I} \otimes \mathbf{I}\right) \quad \text{and} \quad \mathbf{K} = \mathbf{II} - \mathbf{J}, \tag{4.32}$$

where $\mathbf{I}$ is the second-rank identity tensor, $\mathbf{II}$ is the fourth-rank symmetric identity tensor. It can be shown that $\mathbf{J}$ and $\mathbf{K}$ are orthogonal to each other,

$$\mathbf{J} :: \mathbf{K} = 0, \tag{4.33}$$

and

$$\mathbf{J} :: \mathbf{J} = 1, \quad \mathbf{K} :: \mathbf{K} = 2. \tag{4.34}$$

To find the optimum κ^0 and μ^0 from the projection of the effective stiffness tensor $\bar{\mathbf{C}}$, two optimization problems are defined

$$\kappa^0 = \underset{\{\kappa'\}}{\operatorname{argmin}} \; || \left[\bar{\mathbf{C}} - \mathbf{C}_{iso}(\kappa')\right] : \Delta\boldsymbol{\varepsilon}_h^0||^2 \tag{4.35}$$

and

$$\mu^0 = \underset{\{\mu'\}}{\operatorname{argmin}} \; || \left[\bar{\mathbf{C}} - \mathbf{C}_{iso}(\mu')\right] : \Delta\boldsymbol{\varepsilon}_d^0||^2, \tag{4.36}$$

where $\Delta\boldsymbol{\varepsilon}_h^0$ and $\Delta\boldsymbol{\varepsilon}_d^0$ are the hydrostatic and deviatoric parts of the far-field strain increment $\Delta\boldsymbol{\varepsilon}^0$. By taking the derivative of the cost functions in Eq. (4.35) and (4.35) for finding the stationary points, the optimum κ^0 and μ^0 can be expressed in Voigt notation as

$$\kappa^0 = \frac{\bar{\mathbf{C}}_{11} + \bar{\mathbf{C}}_{12} + \bar{\mathbf{C}}_{21} + \bar{\mathbf{C}}_{22}}{4} \tag{4.37}$$

and

$$\mu^0 = \eta_1 \left(\frac{\bar{\mathbf{C}}_{11} - \bar{\mathbf{C}}_{12} - \bar{\mathbf{C}}_{21} + \bar{\mathbf{C}}_{22}}{4} \right) + (1 - \eta_1)\bar{\mathbf{C}}_{33} + \eta_2(\bar{\mathbf{C}}_{13} - \bar{\mathbf{C}}_{23} - \bar{\mathbf{C}}_{32} + \bar{\mathbf{C}}_{31}), \tag{4.38}$$

with

$$\eta_1 = \frac{(\Delta\varepsilon_{11}^0 - \Delta\varepsilon_{22}^0)^2}{(\Delta\varepsilon_{11}^0 - \Delta\varepsilon_{22}^0)^2 + (\Delta\gamma_{12}^0)^2}, \quad \eta_2 = \frac{(\Delta\varepsilon_{11}^0 - \Delta\varepsilon_{22}^0)\Delta\gamma_{12}^0}{(\Delta\varepsilon_{11}^0 - \Delta\varepsilon_{22}^0)^2 + (\Delta\gamma_{12}^0)^2}. \tag{4.39}$$

For cases when the denominator $(\Delta\varepsilon_{11}^0 - \Delta\varepsilon_{22}^0)^2 + (\Delta\gamma_{12}^0)^2$ vanishes, I set $\eta_1 = 0.5$ and $\eta_2 = 0$. Specifically, if the effective macroscopic material is orthotropic, the third term in Eq. (4.38) can be dismissed. Similarly, this self-consistent scheme can also be extended to 3D materials. The expressions of κ^0 and μ^0 for the 3D self-consistent scheme are derived based on Eq. (4.35) and (4.36).

$$\kappa^0 = \frac{\bar{\mathbf{C}}_{11} + \bar{\mathbf{C}}_{12} + \bar{\mathbf{C}}_{13} + \bar{\mathbf{C}}_{21} + \bar{\mathbf{C}}_{22} + \bar{\mathbf{C}}_{23} + \bar{\mathbf{C}}_{31} + \bar{\mathbf{C}}_{32} + \bar{\mathbf{C}}_{33}}{9} \tag{4.40}$$

and

$$\mu^0 = \frac{\Delta\boldsymbol{\varepsilon}_d^0 : \bar{\mathbf{C}} : \Delta\boldsymbol{\varepsilon}_d^0}{\Delta\boldsymbol{\varepsilon}_d^0 : \mathbf{T} : \Delta\boldsymbol{\varepsilon}_d^0}, \tag{4.41}$$

where $\mathbf{T}$ is a transformation tensor derived from the optimum problem. It can be written in Voigt notation as

$$\mathbf{T} = \begin{Bmatrix} 4/3 & -2/3 & -2/3 & 0 & 0 & 0 \\ -2/3 & 4/3 & -2/3 & 0 & 0 & 0 \\ -2/3 & -2/3 & 4/3 & 0 & 0 & 0 \\ 0 & 0 & 0 & 1 & 0 & 0 \\ 0 & 0 & 0 & 0 & 1 & 0 \\ 0 & 0 & 0 & 0 & 0 & 1 \end{Bmatrix} \tag{4.42}$$

Finally, the algorithm of the self-consistent scheme is shown in Box I in a general sense. For nonlinear materials, the stress increment $\Delta\boldsymbol{\sigma}_m^J$ is a nonlinear function of its strain increment $\Delta\boldsymbol{\varepsilon}_m^J$, and Newton's method is usually used to solve the nonlinear system iteratively at each load increment. Additional details on the Newton's iteration are provided in the Appendix E.

Box I General algorithm for the self-consistent scheme

(1) Initial conditions and initialization: set $(\kappa^0, \mu^0)\,; n = 0; \{\Delta\boldsymbol{\varepsilon}_m^I, \Delta\boldsymbol{\varepsilon}^0\}_n = \mathbf{0}$

(2) For loading increment $n+1$, update the interaction tensor $\mathbf{D}^{IJ}$ and the stiffness tensor of the reference material $\mathbf{C}^0$ based on (κ^0, μ^0)

(3) Solve the discretized Lippmann-Schwinger equation (4.8). For nonlinear materials, Newton's method is used

(4) Compute the effective stiffness tensor $\bar{\mathbf{C}}$, and calculate the optimum (κ^0, μ^0) using Eq. (4.37) and (4.38) (projection-based scheme) or using Eq. (4.29) (regression-based scheme)

(5) Check error criterion for (κ^0, μ^0); if not met, go to 2

(6) Update the strain and stress increments: $\{\Delta\boldsymbol{\varepsilon}_m^I, \Delta\boldsymbol{\varepsilon}^0\}_{n+1}, \{\Delta\boldsymbol{\sigma}_m^I\}_{n+1}$

(7) Update the index of loading increment: $n \leftarrow n+1$

(8) If simulation not complete, go to 2.

4.4. Numerical examples

The proposed reduced order homogenization method was applied to 2D plane strain and 3D heterogeneous materials under different load cases. As detailed in the previous sections, the whole modeling framework can be divided into two stages: 1) offline stage; and 2) online stage. In the 2D plane strain examples, two types of materials with different microstructures as shown in Figure 4.3 are analyzed. The first one is a composite material with identical circular fibers (phase 2) embedded in the matrix (phase 1), where the fiber volume fraction was considered as $V_{f_2} = 30\%$. The second 2D plane strain example is a two-phase material with microstructure obtained from a phase-field simulation based on the Cahn-Hilliard equation, where the volume fraction of either phase is equal to 50%. For convenience, the two types of materials are abbreviated as fiber-reinforced composite and amorphous material, respectively.

Two examples in 3D are also presented: one was chosen as a two-phase composite material with identical spherical inclusions embedded in the matrix (volume fraction of 20%), and the other as an amorphous material with a microstructure obtained from a 3D

phase-field simulation (volume fraction of 50%). All the microstructures considered in the examples are periodic.

The same material properties are used in the 2D and 3D problems. For the linear elastic direct numerical simulations in the offline stage, the Young's moduli and Poisson's ratios of phase 1 and 2 are:

$$E_1 = 100 \text{ MPa}, \nu_1 = 0.3; \quad E_2 = 500 \text{ MPa}, \nu_2 = 0.19. \tag{4.43}$$

The clustering results for all these materials can be found in Figure 4.3, 4.4 and 4.5. Each reduced RVE obtained for a chosen number of clusters is then analyzed in the online stage. Note that the same reduced RVE can be used for predicting plastic behavior of the material with any local plasticity laws for each phase (no additional calibration needed). Therefore, the following examples considered two different plasticity laws in order to assess the predictive capabilities of the proposed approach.

Two plasticity laws were considered in the online stage for phase 1 (the matrix material). Both laws considered a von Mises yield surface,

$$f = \bar{\sigma} - \sigma_Y(\varepsilon_p) \leqslant 0, \tag{4.44}$$

where $\bar{\sigma}$ is the von Mises equivalent stress, and the yield stress σ_Y is given by the chosen hardening law that depends on the equivalent plastic strain ε_p.

The first hardening law considered was piecewise linear and isotropic as follows,

$$\sigma_Y(\varepsilon_p) = \begin{cases} 0.5 + 5\varepsilon_p & \varepsilon_p \in [0, 0.04) \\ 0.7 + 2\varepsilon_p & \varepsilon_p \in [0.04, \infty) \end{cases} \text{ MPa}. \tag{4.45}$$

The other hardening law considered was the following power-law,

$$\sigma_Y(\varepsilon_p) = 0.1 + 0.3\varepsilon_p^{0.4} \text{ MPa}. \tag{4.46}$$

The plasticity simulations were conducted under different loading conditions. For example, under uniaxial tension the macroscopic strain ε_{11} is prescribed, and the macroscopic stresses vanish in all other directions: $\sigma_{ij} = 0$ for $i, j \neq 1$. For pure shear loading condition, γ_{12} is imposed, and the remaining stress-free conditions are applied similarly.

The predictions given by the reduced order modeling, including macroscopic behavior and microscopic stress/strain fields, are validated against high-fidelity direct numerical simulations (DNS) using the finite element method with a fine mesh and imposing periodic boundary conditions. The computational efficiency of the proposed method is discussed as well.

4.4.1. Two-dimensional nonlinear elasto-plastic materials

Particularly relevant is the assessment of the predictive capabilities of the proposed model when capturing the nonlinear plastic behavior of the RVE under various loading conditions, as well as the computational cost (CPU time and memory) when compared to the DNS. First, the influence of the self-consistent scheme on the plastic predictions is investigated considering the two hardening laws introduced previously: the piece-wise linear hardening, Eq. (5.32); and the power-law hardening, Eq. (4.46). Figure 4.6 presents the stress-strain results for the fiber-reinforced composite subjected to uniaxial tension for these two hardening laws of the matrix.

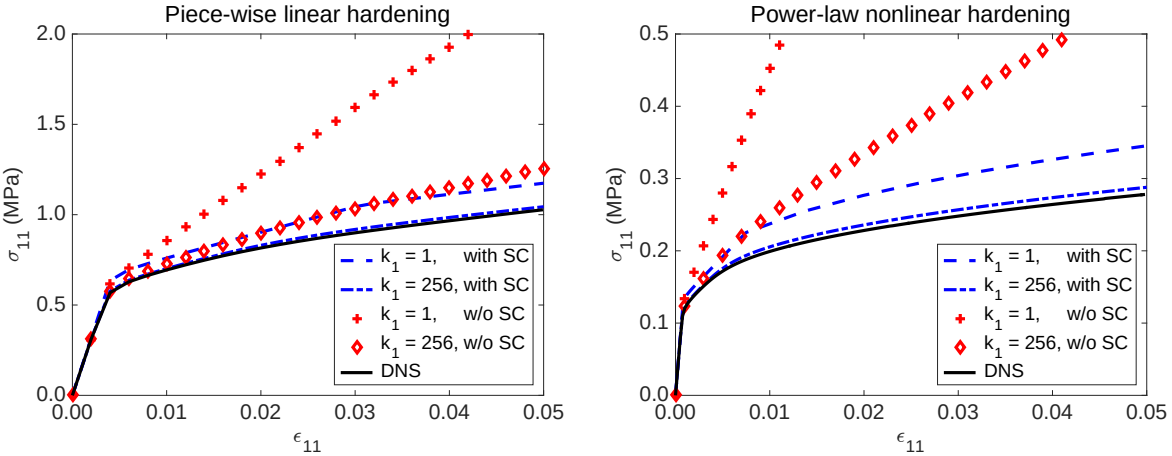

Figure 4.6. The effect of the self-consistent scheme.

As can be observed in the figure, although the error of the method when compared to DNS is reduced in each case by increasing the number of clusters, the self-consistent scheme converges significantly faster for a desired level of accuracy. This is especially visible for the power-law nonlinear hardening. When plastic yielding happens in the

heterogeneous material, the macroscopic tangent stiffness tensor starts decreasing when compared to the elastic case due to localized plasticity in the matrix, so that $\mathbf{C}^{\text{matrix}}$ is no longer a good choice for the tangent stiffness $\mathbf{C}^0$ of the reference material. By consistently updating $\mathbf{C}^0$ with an approximate value of the effective stiffness of the RVE, see Box 2.2, the evolution of the local internal variables in each cluster is captured more accurately.

Another point to be considered is the effect of the $\mathbf{A}$-based clustering used during the offline stage. As discussed in that section, the k-means clustering was done based on the strain concentration tensor $\mathbf{A}(\mathbf{x})$ at each data point, with the purpose of grouping the data points with similar mechanical behavior into one cluster. A more naive compression scheme would be to do the clustering purely based on the spatial coordinates $\mathbf{x}$ of the data points, i.e. grouping points by their spatial proximity instead of considering the similarity of mechanical behavior. This position-based clustering leads to a cluster map resembling a Voronoi diagram, as illustrated in Figure 4.7 (left) for 32 clusters in phase 1 for the fiber-reinforced composite. The reader is encouraged to compare this figure with Figure 4.3c) to see the difference in the clustering scheme for the **same** number of clusters but using the $\mathbf{A}$-based clustering.

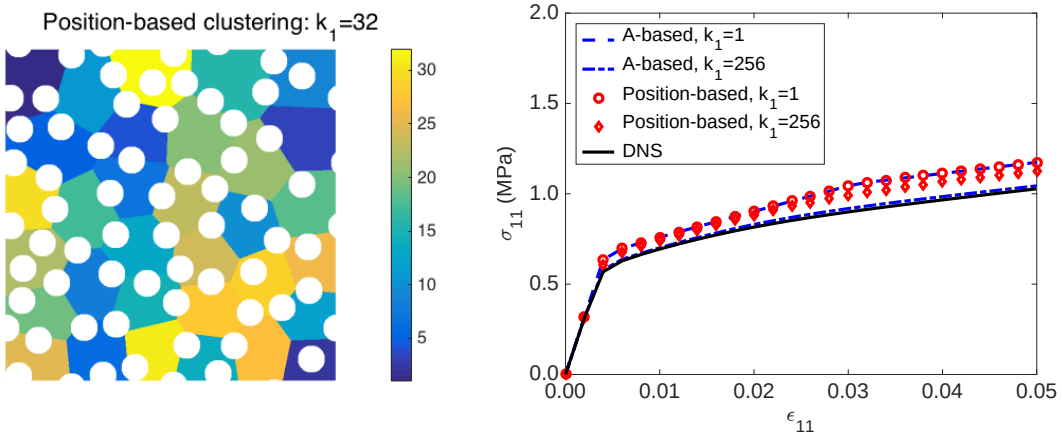

Figure 4.7. The effect of the raw data type on the clustering results (32 clusters) and the macroscopic predictions.

On the right of Figure 4.7, the results of position-based clustering are compared to the **A**-based clustering. In this figure, it is seen that the convergence using the position-based clusters is poor, and the accuracy of the prediction does not change significantly even considering 256 clusters for phase 1. On the contrary, with the same number of clusters, the predictions from **A**-based clustering reproduce the DNS almost exactly. For more complex material properties such as damage and fracture, one may also add more nonlinear information like equivalent plastic strain field into the raw data, so that the localized behaviors can be well characterized by the clustering steps.

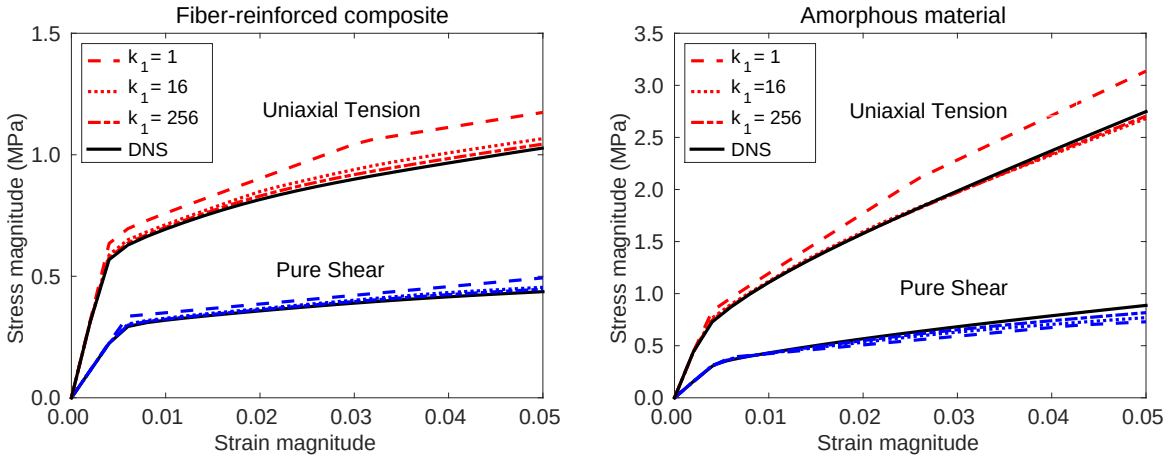

Figure 4.8. The predictions for the fiber-reinforced composite (left) and amorphous material (right).

Figure 4.8 includes the stress-strain curves for the fiber-reinforced composite and the amorphous material considering two different load cases, uniaxial tension and pure shear, using the self-consistent scheme. The number of clusters in phase 1 ranges from 1 to 256, and the results from DNS are also provided for comparison. By looking at the plots, one can conclude that the proposed method is capable of capturing the nonlinear plastic behavior with significantly fewer degrees of freedom but with a small loss in accuracy. Furthermore, the refinement of the discretization by including more clusters clearly improves the predictions: a desirable characteristic allowing the analyst to choose between accuracy and efficiency.

Figure 4.9 provides a comparison of the local fields obtained from DNS of the high-fidelity RVE and from the proposed self-consistent clustering analysis of a reduced RVE

with 256 clusters for phase 1. The figures show that the new method is able to reproduce the equivalent plastic strain fields, although the localized regions are reproduced in a more diffuse manner leading to regions with lower strain concentrations. This is expected since by definition the goal of the proposed approach is to predict as accurately as possible the global (homogenized) mechanical response with the minimum amount of information possible. In order to improve the resolution at these regions, the total number of clusters could be increased or, more wisely, a nonlinear mapping of the k-means clustering could be applied so that more clusters are assigned to regions needing higher resolution (the issue is finding these regions, since different loading conditions lead to different localization areas).

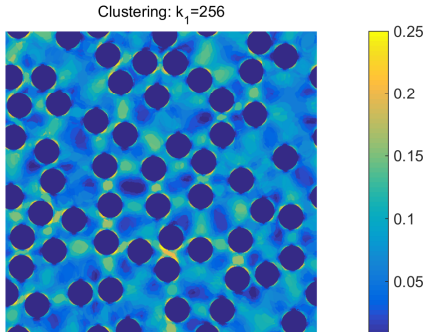

(a) Reduced RVE for composite material

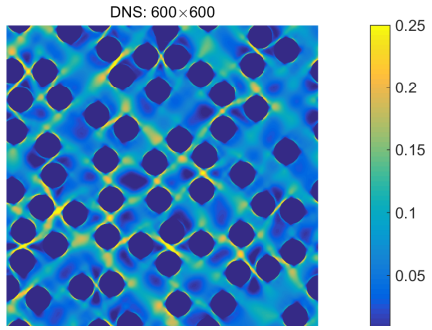

(b) High-fidelity RVE for composite material

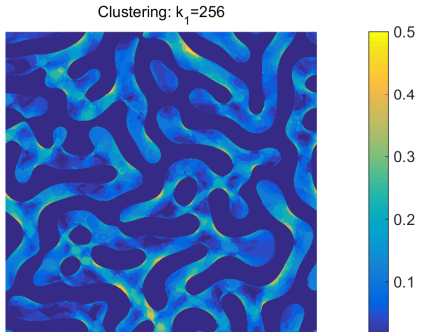

(c) Reduced RVE for amorphous material

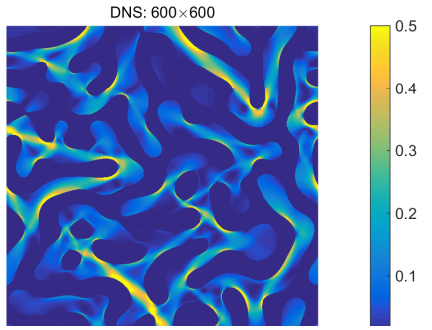

(d) High-fidelity RVE for amorphous material

Figure 4.9. Equivalent plastic strain fields obtained from DNS and from SCA.

Up to this point the computational cost reduction of the method was not quantified. Even though the reduction achieved in the number of degrees of freedom is obvious, the

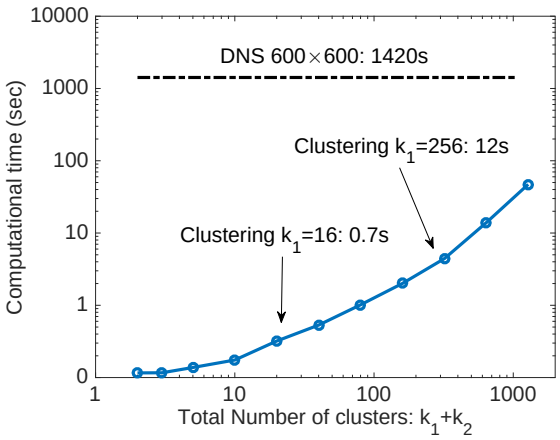

Figure 4.10. The computational time comparison.

system of equations that is being solved uses an iterative approach, and each equation involves the summation over every cluster. Therefore, there is a clear trade-off between the compression of information achieved by the clustering procedure and the actual solution of the Lippmann-Schwinger equations. Figure 4.10 shows a comparison of computation time between the proposed approach for different numbers of clusters and the DNS. The results are encouraging, especially considering that the DNS finite element analyses were performed using a commercial code (significantly optimized), while the proposed method was implemented in MATLAB. A typical two-dimensional DNS took about 1420s ($\approx$ 24min) on one intel i7-3632 processor, while the online stage of the reduced order method with the self-consistent scheme (in MATLAB) took 4s for $k_1 = 16$ and 75s for $k_1 = 256$. For $k_1 \in [1, 512]$, the computational time is almost proportional to the number of clusters in the system, which indicates that the most time-consuming part is to update the internal variables locally at each cluster.

Finally, the reduced order model was also validated against a complex loading path. Macro-strain constraints are applied on ε_{11} and γ_{12}, while $\sigma_{22} = 0$. Thus, the loading state can be represented by $(\varepsilon_{11}, \gamma_{12})$. As shown in Figure 4.11a), there are three steps in the loading path, and the material finally returns to the initial state $(\varepsilon_{11} = 0, \gamma_{12} = 0)$. Due to plasticity, ε_{22} does not necessarily vanish at the final state, which means that the initial state with $\varepsilon_{22} = 0$ is not reproduced. The stress-strain curves σ_{11}-vs-ε_{11} and

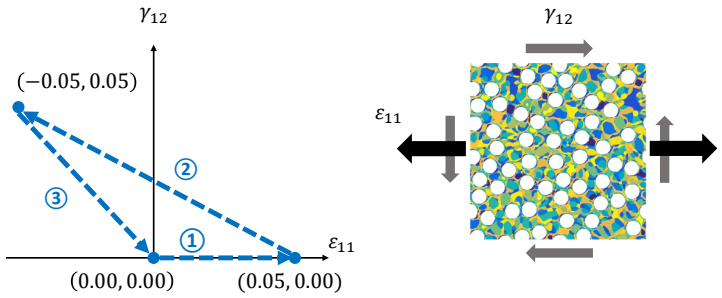

(a) Illustrations of the complex loading path $(\varepsilon_{11}, \gamma_{12})$, where ε_{11} and γ_{12} are imposed as shown and $\sigma_{22} = 0$

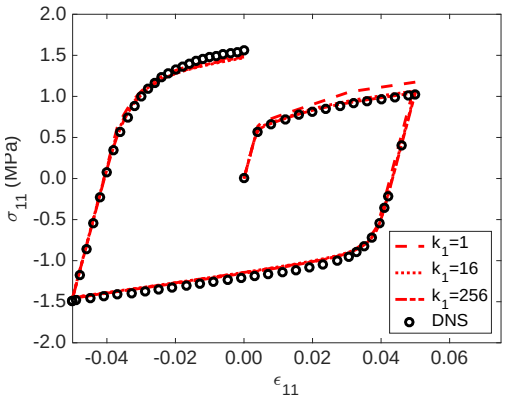

(b) Normal stress versus normal strain

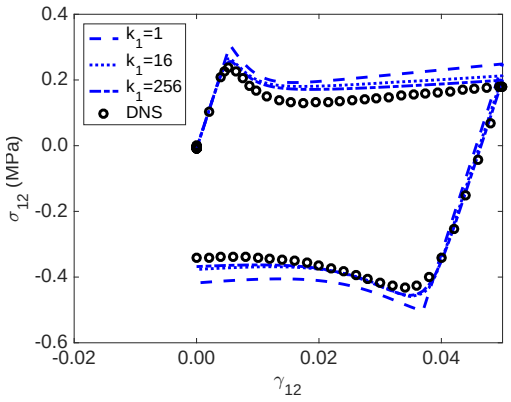

(c) Shear stress versus shear strain

Figure 4.11. Response of the reduced RVE under a three-step complex loading path.

σ_{12}-vs-γ_{12} given by the reduced-order method and the DNS results are shown in Figure 4.11b) and c). Once again good agreement is observed.

4.4.2. Three-dimensional nonlinear elasto-plastic material

The proposed method was also applied to 3D nonlinear elasto-plastic materials similar to the previously presented examples in 2D. First, a spherical-particle composite is considered with the phase 1 being the matrix (as before) and the number of matrix clusters being k_1. The volume fraction of the particle phase (phase 2) was considered to be 20% and $k_2 = \lceil k_1/4 \rceil$. All the material properties are the same as before (see equations (4.43), (5.31) and (5.32)). The mesh size of the finite element model considered as the DNS

was $80 \times 80 \times 80$, and the illustration of the mesh in the inclusion phase (phase 2) is demonstrated in Figure 4.12. The reader is reminded that when generating the raw data, the strain concentration tensor $\mathbf{A(x)}$ has 36 independent components since this is a 3D RVE. Thus, the dimension of data becomes 36, and a linear increase in the running time of the k-means clustering occurs.

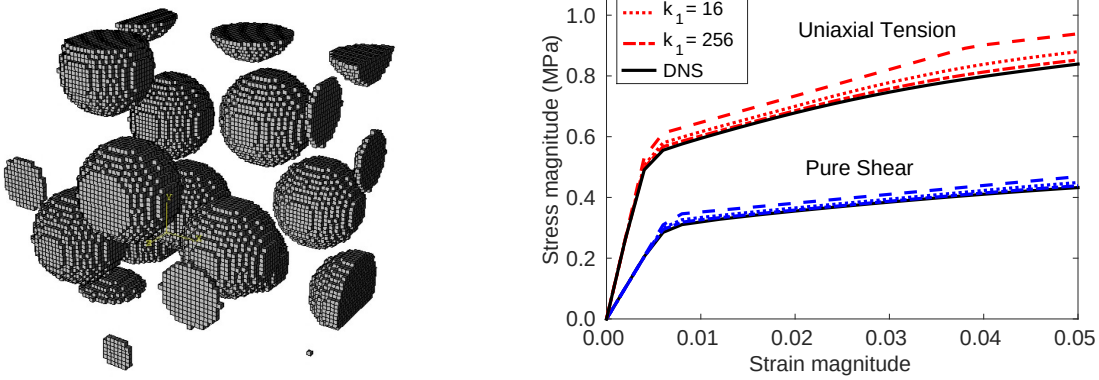

Figure 4.12. The $80 \times 80 \times 80$ FE mesh of the 3D composite and the predicted stress-strain curves.

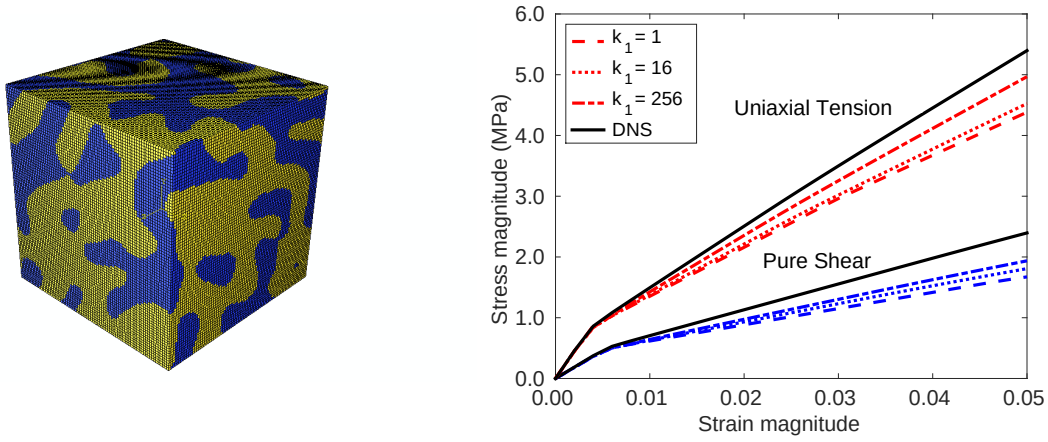

Figure 4.13. The $80 \times 80 \times 80$ FE mesh of the 3D amorphous material and the predicted stress-strain curves.

The stress-strain curves given by the self-consistent clustering analysis of the reduced RVE and the DNS of the high-fidelity RVE results are plotted in Figure 4.12. Although the convergence rates of macroscopic mechanical properties with respect to the number of clusters in 3D is not as high as the ones in 2D, good accuracy can be achieved by assigning 256 clusters in phase 1 (320 in total) under both loading conditions. In terms of computational cost, a typical DNS with $80 \times 80 \times 80$ mesh took 25.7 hours on 24 cores (in a state-of-the art high performance computing cluster with the following compute nodes: Intel Haswell E5-2680v3 2.5GHz 12-cores). The reduced order method (in MATLAB) took 2s and 50s on one intel i7-3632 processor for $k_1 = 16$ and $k_1 = 256$, respectively.

The final example chosen to present in this work is a 3D two-phase amorphous material obtained by solving the Cahn-Hilliard equation in 3D. The illustration of the 3D microstructure is shown in Figure 4.13, and the finite element mesh considered for the DNS was $80 \times 80 \times 80$. The volume fraction of each phase was defined as 50%, so $k_2 = k_1$ in the clustering step. The stress-strain curves in Figure 4.13 show that the predictions given by the reduced order method converge slower than all the previous examples considered: this is attributed to the complexity of microstructure in the 3D amorphous material that leads to fewer similarities in the local stress/strain field, implying the need to use more clusters in order to characterize the nonlinear behavior appropriately.

CHAPTER 5

Homogenization for Strain Softening Materials

5.1. Background and motivation

Modeling material damage and localization with continuum damage methods [**44, 20**] poses stability challenges because the damaged region of the material will always localize to a single layer of elements. Further mesh refinement results in thinner localization bands and reduced energy dissipation, which is contrary to the physical energy dissipation of localization. This challenge occurs due to the local material strain-softening effect, in which the tangential stiffness matrix is no longer positive definite, leading to an imaginary wave speed. As such, the boundary value problem becomes ill-posed. Several methods have been proposed to resolve this mesh-dependence problem due to the strain-softening effect, such as nonlocal damage model [**6**], micromorphic continuum [**80, 113, 79, 115, 37**], phase-field fracture [**89, 88**], crack band theory [**7**] and eigen-erosion method [**98**]. Among all these methods, a material length parameter or the material fracture energy G_f are introduced to regularize the original ill-posed boundary value problem. For example, in phase-field model for quasi-brittle fracture [**89**], G_f is defined as a material constant measured from experiment, which limits the energy dissipation per unit area in the crack. Meanwhile, the material length parameter helps to diffuse the fracture singularity over a finite damaged region, making it numerically solvable. In nonlocal damage models [**6**], the material length parameter is introduced to spread the damaged region over a finite domain, which allows the objectivity of the numerical solution to be recovered.

Meanwhile, material fracture is sensitive to the microstructure and evaluating these effects requires a multiscale modeling approach which incorporates these details. A material's microstructure can consist of voids or inclusions which will lead to a non-uniform

stress and strain state in the microstructure. Multiscale modeling couples the microstructural stress state with the macroscopic calculation to capture the effects of the microstructure in a macroscopic calculation. First, an associated strain increment $d\boldsymbol{\varepsilon}_M$ at a macroscopic integration point is applied as boundary conditions on the microstructural RVE. According to the Hill-Mandel lemma, the homogenized stress $\boldsymbol{\sigma}_M$ can be computed by averaging the microstructural stress $\boldsymbol{\sigma}_m$ in the RVE. Through this homogenization process, the mechanical response at each macro material/integration point is coupled with a microscale RVE model. Meanwhile, the computed microscopic history-dependent internal variables are stored in the RVE for continued analysis. This concurrent framework is advantageous since the constitutive law can be adjusted *on the fly* based on the microstructural characteristics. The multiscale framework obviates the need for a cumbersome equation-based phenomenological constitutive law to account for the behavior of history-dependent material with complex micro-morphologies and nonlinear behavior such as plasticity.

However the homogenization scheme introduced in Section 1.1 may encounter stability problems when the material experiences strain-softening, such as material failure described by a progressive damage model. The progressive damage model directly applied to the microstructural RVE suffers from material instability due to non-physical strain softening, leading to results in which the localization occurs in very narrow bands of elements [**7, 6, 52**]. Since no regularization is introduced in this example, the width of the band depends on the mesh size. Even if the microscale RVE is regularized with a physical band width, the homogenized macroscopic stress-strain response still strongly depends on the RVE size, so that it cannot represent the material behavior at local macroscopic material point [**5**].

5.2. Three-step homogenization scheme

A micro-damage stabilization algorithm is proposed which removes the material strain softening instability associated with traditional damage models. This is accomplished by introducing a reference elastoplastic RVE and decoupling the damage from the plastic evolution. Similar to the phase-field fracture, the damage parameter (or stiffness degradation

function) models the transition of complementary free energy towards the dissipation energy due to fracture. No damage is considered in the reference elastoplastic RVE, and its macroscopic complementary free energy density is proposed as

$$\mathcal{G}_M^0 = \frac{1}{2}\boldsymbol{\sigma}_M^0 : \left[(\mathbf{C}_M)^{-1} : \boldsymbol{\sigma}_M^0\right] = \frac{1}{2}\boldsymbol{\sigma}_M^0 : \boldsymbol{\varepsilon}_M^{el}, \tag{5.1}$$

where $\boldsymbol{\sigma}_M^0$ is the macroscopic stress of the undamaged reference RVE, whose effective elastic stiffness tensor is denoted by $\mathbf{C}_M$. $\boldsymbol{\varepsilon}_M^{el}$ is macroscopic effective elastic strain, which is defined as

$$\boldsymbol{\varepsilon}_M^{el} = (\mathbf{C}_M)^{-1} : \boldsymbol{\sigma}_M^0. \tag{5.2}$$

Note that the complementary free energy density $\mathcal{G}_M^0$ represents the portion of internal elastic energy that can be converted to work. If the RVE is purely elastic, $\mathcal{G}_M^0$ is equal to the average strain energy density in the RVE. However, this equivalence will no longer hold if plasticity happens inside the RVE. Due to the local heterogeneous plastic strain field, the RVE can only be unloaded to a stress-free state with non-zero strain energy, which cannot be converted to work.

Assume the microscopic stress and elastic strain of the stress-free state are denoted by $\hat{\boldsymbol{\sigma}}_m$ and $\hat{\boldsymbol{\varepsilon}}_m^{el}$, with

$$\frac{1}{|\Omega|}\int_\Omega \hat{\boldsymbol{\sigma}}_m d\Omega = \mathbf{0}. \tag{5.3}$$

Then the homogenized elastic strain energy density stored in the stress-free state can be expressed as

$$\hat{\mathcal{U}}_M = \frac{1}{2|\Omega|}\int_\Omega \hat{\boldsymbol{\sigma}}_m : \hat{\boldsymbol{\varepsilon}}_m^{el} d\Omega = \frac{1}{2|\Omega|}\int_\Omega (\mathbf{C}_m : \hat{\boldsymbol{\varepsilon}}_m^{el}) : \hat{\boldsymbol{\varepsilon}}_m^{el} d\Omega, \tag{5.4}$$

where $\mathbf{C}_m$ is the microscopic stiffness tensor in the RVE. For the undamaged elastoplastic RVE, its microscopic stress and elastic strain are denoted by $\boldsymbol{\sigma}_{m1}$ and $\boldsymbol{\varepsilon}_{m1}^{el}$. The total strain energy density in the RVE can be written as

$$\mathcal{U}_M = \frac{1}{2|\Omega|}\int_\Omega \boldsymbol{\sigma}_{m1} : \boldsymbol{\varepsilon}_{m1}^{el} d\Omega. \tag{5.5}$$

The complementary free energy density can be computed as

$$\mathcal{G}_M^0 = \mathcal{U}_M - \hat{\mathcal{U}}_M = \frac{1}{2|\Omega|}\int_\Omega \left(2\hat{\boldsymbol{\sigma}}_m : \boldsymbol{\varepsilon}_{m2} + \boldsymbol{\sigma}_{m2} : \boldsymbol{\varepsilon}_{m2}\right) d\Omega \tag{5.6}$$

where we have

$$\boldsymbol{\varepsilon}_{m2} = \boldsymbol{\varepsilon}_{m1} - \hat{\boldsymbol{\varepsilon}}_m^{el}, \quad \boldsymbol{\sigma}_{m2} = \boldsymbol{\sigma}_{m1} - \hat{\boldsymbol{\sigma}}_m^{el} \quad \text{and} \quad \boldsymbol{\sigma}_{m2} = \mathbf{C}_m : \boldsymbol{\varepsilon}_{m2}. \tag{5.7}$$

For arbitrary compatible strain field $\boldsymbol{\varepsilon}_{m2}$, it can be proved that

$$\int_\Omega \hat{\boldsymbol{\sigma}}_m : \boldsymbol{\varepsilon}_{m2} d\Omega = \mathbf{0}. \tag{5.8}$$

Proof. of Eq. (5.8):

Based on the symmetry of the Cauchy stress tensor, we have

$$\hat{\boldsymbol{\sigma}}_m : \boldsymbol{\varepsilon}_{m2} = \hat{\boldsymbol{\sigma}}_m : \frac{1}{2}\left(\nabla \mathbf{u}_{m2} + \nabla^T \mathbf{u}_{m2}\right) = \hat{\boldsymbol{\sigma}}_m : \nabla \mathbf{u}_{m2},$$

where $\mathbf{u}_{m2}$ is the displacement field corresponding to the compatible strain field $\boldsymbol{\varepsilon}_{m2}$. Then, using integration by parts,

$$\int_\Omega \hat{\boldsymbol{\sigma}}_m : \boldsymbol{\varepsilon}_{m2} d\Omega = \int_\Omega \hat{\boldsymbol{\sigma}}_m : \nabla \mathbf{u}_{m2} d\Omega = \int \mathbf{u}_{m2} \cdot \left(\hat{\boldsymbol{\sigma}}_m \cdot \mathbf{n}\right) d\Gamma - \int_\Omega \mathbf{u}_{m2} \cdot \left(\nabla \cdot \hat{\boldsymbol{\sigma}}_m\right) d\Omega$$

Due to the periodicity of the RVE and stress-free condition,

$$\int \mathbf{u}_{m2} \cdot \left(\hat{\boldsymbol{\sigma}}_m \cdot \mathbf{n}\right) d\Gamma = 0,$$

and the equilibrium condition of the stress-free state gives

$$\nabla \cdot \hat{\boldsymbol{\sigma}}_m = \mathbf{0}$$

Noting the above two equations, we conclude the proof of Eq. (5.8). □

Based on Eq. (5.6) and (5.8), the complementary free energy density can be written as

$$\mathcal{G}_M^0 = \frac{1}{2|\Omega|}\int_\Omega \boldsymbol{\sigma}_{m2} : \boldsymbol{\varepsilon}_{m2} d\Omega = \frac{1}{2|\Omega|}\int_\Omega (\mathbf{C}_m : \boldsymbol{\varepsilon}_{m2}) : \boldsymbol{\varepsilon}_{m2} d\Omega \tag{5.9}$$

Applying the Hill-Mandel lemma yields the expression in Eq. (5.1)

$$\mathcal{G}_M^0 = \frac{1}{2}\boldsymbol{\sigma}_M^0 : \boldsymbol{\varepsilon}_M^{el} \tag{5.10}$$

with

$$\boldsymbol{\sigma}_M^0 = \frac{1}{|\Omega|}\int_\Omega \boldsymbol{\sigma}_{m2} d\Omega, \quad \text{and} \quad \boldsymbol{\varepsilon}_M^{el} = \frac{1}{|\Omega|}\int_\Omega \boldsymbol{\varepsilon}_{m2} d\Omega \tag{5.11}$$

Damage is introduced to convert the complementary free energy to fracture dissipation energy. The complementary free energy density of the damaged RVE is proposed as

$$\mathcal{G}_M^d = \frac{1}{2|\Omega|}\int_\Omega [(1-d_m)\mathbf{C}_m : \boldsymbol{\varepsilon}_{m3}] : \boldsymbol{\varepsilon}_{m3} d\Omega. \tag{5.12}$$

with

$$\frac{1}{|\Omega|}\int_\Omega \boldsymbol{\varepsilon}_{m3} d\Omega = \boldsymbol{\varepsilon}_M^{el} \tag{5.13}$$

The complementary free energy density of the damaged RVE assures that the thermodynamic force or energy dissipation rate Y_m is always positive:

$$Y_m(\mathbf{x}) = -\frac{\partial \mathcal{G}_M^d}{\partial d_m} = \frac{1}{2|\Omega|}\left(\mathbf{C}_m : \boldsymbol{\varepsilon}_{m3}\right) : \boldsymbol{\varepsilon}_{m3} \geq 0. \tag{5.14}$$

Proof. of Eq. (5.14):

Assume the damage parameter d_m has a infinitesimal change δd_m only at a point $\mathbf{x}$ inside the RVE. This will result in the change of the stiffness tensor $(1-d_m)\mathbf{C}_m$ at the same material point, as well as the strain $\boldsymbol{\varepsilon}_{m3}(\mathbf{x})$ in the new RVE. The change of $\boldsymbol{\varepsilon}_{m3}(\mathbf{x})$ is denoted by $\delta\boldsymbol{\varepsilon}_{m3}(\mathbf{x})$. Since the total effective elastic strain is kept the same, we have

$$\int_\Omega \delta\boldsymbol{\varepsilon}_{m3} d\Omega = \mathbf{0}$$

Then the difference in the complementary energy can be expressed as

$$\delta\mathcal{G}_M^d = -\frac{1}{2|\Omega|}\delta d_m \left(\mathbf{C}_m : \boldsymbol{\varepsilon}_{m3}\right) : \boldsymbol{\varepsilon}_{m3} + \frac{1}{|\Omega|}\int_\Omega \boldsymbol{\sigma}_{m3} : \delta\boldsymbol{\varepsilon}_{m3} d\Omega + o(\delta d_m^2).$$

Using integration by parts,

$$\int_\Omega \boldsymbol{\sigma}_{m3} : \delta\boldsymbol{\varepsilon}_{m3} d\Omega = \int_\Omega \hat{\boldsymbol{\sigma}}_{m3} : \nabla\delta\mathbf{u}_{m3} d\Omega = \int \delta\mathbf{u}_{m3} \cdot (\hat{\boldsymbol{\sigma}}_{m3} \cdot \mathbf{n})\, d\Gamma - \int_\Omega \delta\mathbf{u}_{m3} \cdot (\nabla \cdot \hat{\boldsymbol{\sigma}}_{m3})\, d\Omega.$$

Based on the periodicity of the RVE and the equilibrium condition, it follows

$$\int_\Omega \boldsymbol{\sigma}_{m3} : \delta\boldsymbol{\varepsilon}_{m3} d\Omega = 0.$$

Thus, the difference in the complementary free energy becomes

$$\delta\mathcal{G}_M^d = -\frac{1}{2|\Omega|}\delta d_m \left(\mathbf{C}_m : \boldsymbol{\varepsilon}_{m3}\right) : \boldsymbol{\varepsilon}_{m3} + o(\delta d_m^2),$$

and the thermodynamic force can be derived as

$$Y_m(\mathbf{x}) = -\frac{\partial\mathcal{G}_M^d}{\partial d_m} = \frac{1}{2|\Omega|}\left(\mathbf{C}_m : \boldsymbol{\varepsilon}_{m3}\right) : \boldsymbol{\varepsilon}_{m3}.$$

Since the stiffness tensor $\mathbf{C}_m$ is positive definite,

$$Y_m(\mathbf{x}) \geq 0.$$

□

Finally, the effective macroscopic material law of the RVE with damage can be written as

$$\boldsymbol{\sigma}_M^d = \mathbf{C}_M^d : \boldsymbol{\varepsilon}_M^{el} = \mathbf{C}_M^d : \left(\boldsymbol{\varepsilon}_M - \boldsymbol{\varepsilon}_M^{pl}\right), \tag{5.15}$$

where $\boldsymbol{\sigma}_M^d$ is the macroscopic stress of the damaged RVE, and $\mathbf{C}_M^d$ is the macroscopic effective elastic stiffness tensor of the damaged RVE. Moreover, $\boldsymbol{\varepsilon}_M^{el}$ and $\boldsymbol{\varepsilon}_M^{pl}$ are the macroscopic effective elastic strain and plastic strain, respectively. The effective material law of the reference elasto-plastic RVE can be written as

$$\boldsymbol{\sigma}_M^0 = \mathbf{C}_M : \boldsymbol{\varepsilon}_M^{el} = \mathbf{C}_M : \left(\boldsymbol{\varepsilon}_M - \boldsymbol{\varepsilon}_M^{pl}\right), \tag{5.16}$$

where $\boldsymbol{\sigma}_M^0$ is the macroscopic stress of the undamaged reference RVE, whose effective elastic stiffness tensor is denoted by $\mathbf{C}_M$. Assuming the damaged elastoplastic RVE has the same macroscopic effective elastic strain (or effective plastic strain), the following

relationship between $\boldsymbol{\sigma}_M^d$ and $\boldsymbol{\sigma}_M^0$ exists

$$\boldsymbol{\sigma}_M^d = \mathbf{C}_M^d : \left[(\mathbf{C}_M)^{-1} : \boldsymbol{\sigma}_M^0\right]. \tag{5.17}$$

In a general multi-dimensional heterogeneous material, the macroscopic effective plastic strain $\boldsymbol{\varepsilon}_M^{pl}$ is not necessarily a volume average of the microscopic plastic strain $\boldsymbol{\varepsilon}_m^{pl}$. According to the definition of the macroscopic material law in Eq. (5.16), $\boldsymbol{\sigma}_M^0$ should vanish if $\boldsymbol{\varepsilon}_M$ coincides with $\boldsymbol{\varepsilon}_M^{pl}$

$$\boldsymbol{\sigma}_M^0 = \mathbf{0}, \quad \text{if } \boldsymbol{\varepsilon}_M = \boldsymbol{\varepsilon}_M^{pl} \quad (\text{or} \quad \boldsymbol{\varepsilon}_M^{el} = \mathbf{0}). \tag{5.18}$$

The three-step stabilization algorithm is proposed to compute the effective macroscopic quantities in Eq. (5.15) and (5.16), as illustrated in Figure 5.1.

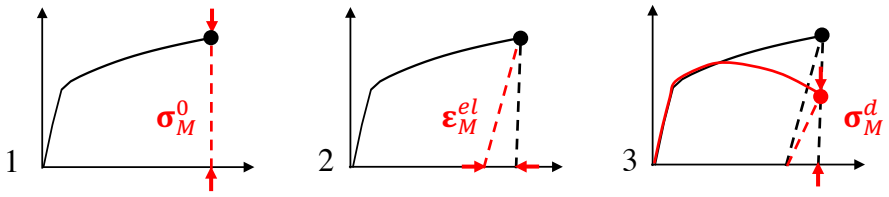

Figure 5.1. Illustration of the three-step algorithm on the macroscopic stress-strain curve.

(1) A strain increment at a macroscopic material point is passed to the reference elasto-plastic RVE as a homogenized strain increment, $d\boldsymbol{\varepsilon}_M$, and applied as a boundary condition. The microscopic material law in RVE1 is

$$\boldsymbol{\sigma}_{m1} = \mathbf{C}_m : \left(\boldsymbol{\varepsilon}_{m1} - \boldsymbol{\varepsilon}_m^{pl}\right). \tag{5.19}$$

The microstructural stress and total strain are computed and the microstructural stress is homogenized using the Hill-Mandel lemma to obtain the macroscopic stress

$$\boldsymbol{\sigma}_M^0 = \frac{1}{|\Omega|}\int_\Omega \boldsymbol{\sigma}_{m1} d\Omega. \tag{5.20}$$

(2) The second step is to separate the macroscopic effective elastic strain $\boldsymbol{\varepsilon}_M^{el}$ (or plastic strain $\boldsymbol{\varepsilon}_M^{pl}$) from the total strain. According to Eq. (5.16), the effective macroscopic elastic strain can be expressed as

$$\boldsymbol{\varepsilon}_M^{el} = (\mathbf{C}_M)^{-1} : \boldsymbol{\sigma}_M^0. \tag{5.21}$$

This is equivalent to applying the homogenized stress from RVE1, $\boldsymbol{\sigma}_M^0$, to a second RVE which is identical to the first RVE, except that the material is an undamaged elastic material,

$$\boldsymbol{\sigma}_{m2} = \mathbf{C}_m : \boldsymbol{\varepsilon}_{m2}. \tag{5.22}$$

The microstructural strain in RVE2 is computed and homogenized so as to yield the macroscopic elastic strain as

$$\boldsymbol{\varepsilon}_M^{el} = \frac{1}{|\Omega|}\int_\Omega \boldsymbol{\varepsilon}_{m2} d\Omega. \tag{5.23}$$

(3) Finally, the macroscopic stress of the damaged material can be computed based on Eq. (5.15)

$$\boldsymbol{\sigma}_M^d = \mathbf{C}_M^d : \boldsymbol{\varepsilon}_M^{el}. \tag{5.24}$$

This is equivalent to applying the homogenized strain from RVE2, $\boldsymbol{\varepsilon}_M^{el}$, to a third RVE with damaged elastic material properties,

$$\boldsymbol{\sigma}_{m3} = (1 - d_m)\mathbf{C}_m : \boldsymbol{\varepsilon}_{m3}, \tag{5.25}$$

where the microscopic damage parameter d_m is a function of the state variables in RVE1 or the reference elasto-plastic RVE,

$$d_m = d_m(\mathbf{q}_{m1}). \tag{5.26}$$

The microscopic stress in RVE3 is computed and homogenized as

$$\boldsymbol{\sigma}_M^d = \frac{1}{|\Omega|}\int_\Omega \boldsymbol{\sigma}_{m3} d\Omega. \tag{5.27}$$

The homogenized stress, $\boldsymbol{\sigma}_M^d$, is returned to the macroscale model as the damaged macroscopic stress at the material point corresponding to the macroscopic strain.

Box II Algorithm for the homogenization scheme of multiscale damage

(1) At each material point in the macroscale simulation, pass the strain increment $d\boldsymbol{\varepsilon}_M$ in to the corresponding microscale RVE model.

(2) Analyze the microscale RVE model:

  (a) Apply $d\boldsymbol{\varepsilon}_M$ to a history-dependent elasto-plastic RVE1 without damage. The stress is computed and homogenized as $\boldsymbol{\sigma}_M^0$

  (b) Apply $\boldsymbol{\sigma}_M^0$ to an undamaged elastic RVE2. The elastic strain is computed and homogenized as $\boldsymbol{\varepsilon}_M^{el}$

  (c) Compute the local microscale damage parameter d_m based on RVE1 analysis and apply $\boldsymbol{\varepsilon}_M^{el}$ to an damaged elastic RVE3. The stress is computed and homogenized as $\boldsymbol{\sigma}_M^d$

(3) Calculate and store relevant internal variables, such as the effective damage parameter d_M

(4) Return $\boldsymbol{\sigma}_M^d$ to the macroscale material point.

To characterize the damage state of the RVE, an effective macroscopic damage parameter, d_M, can be defined,

$$d_M = 1 - \frac{||\boldsymbol{\sigma}_M^d : \boldsymbol{\sigma}_M^0||}{||\boldsymbol{\sigma}_M^0 : \boldsymbol{\sigma}_M^0||} \tag{5.28}$$

The macroscale homogenized material and the associated RVE are usually said to be fully damaged when $d_M = 1$, although it is also possible to fail the RVE at a smaller d_M to model a more brittle behavior. Note that the effective damage parameter is not defined as the field average of the local damage parameter, so full damage can be achieved even if only part of the RVE is fully damaged. The effective damage parameter is a natural by-product of the homogenization scheme and does not affect the stress-strain relation, but it does provide a useful state variable/indicator for tracking localization in the macroscale

simulation. Finally, all the basics steps in the proposed three-step homogenization scheme are listed in Box II.

5.3. RVE-size independence for the three-step homogenization algorithm

In this section, the effect of RVE size on the homogenized results is evaluated. A comparison is made between an RVE of size L, an RVE of size $0.5L$, and an RVE of size $2L$ with non-overlapping circular inclusions embedded in the matrix material, as shown in Figure 5.2. Each RVE has the same inclusion radius, volume fraction and nearest

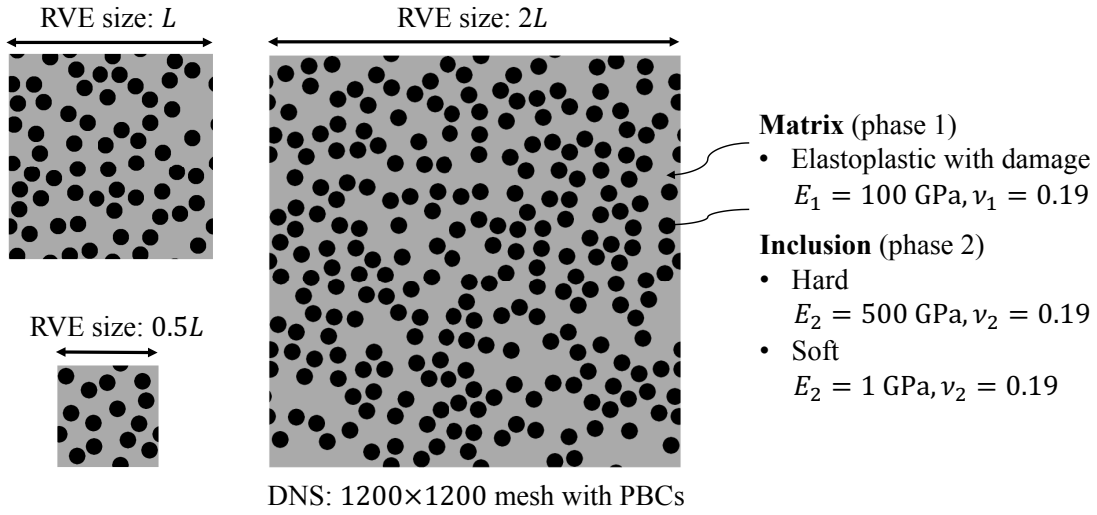

Figure 5.2. Illustration of the microscale RVE of a two-phase heterogeneous material used for the analysis: matrix (phase 1) with randomly distributed circular inclusions (phase 2) embedded.

inclusion distance [**71**]. Inclusions are randomly placed into the matrix material using an algorithm introduced in [**83**]. Both hard inclusions and soft inclusions are considered to be linearly elastic, whose material properties are given in Eq. (5.29) and Eq. (5.30), respectively,

$$E_2 = 500 \text{ GPa}, \nu_2 = 0.19 \quad \text{for hard inclusions,} \tag{5.29}$$

and

$$E_2 = 1 \text{ GPa}, \nu_2 = 0.19 \quad \text{for soft inclusions.} \tag{5.30}$$

The matrix phase is assumed to be an elasto-plastic material with damage. In this chapter, an associative plastic flow law with a von Mises yield surface is considered

$$f = \sigma_v - \sigma_Y(\varepsilon_p) \leqslant 0, \tag{5.31}$$

where σ_v is the equivalent von Mises stress. The yield stress σ_Y is determined by the hardening law as a function of the effect plastic strain ε_p, which is a monotonically increasing internal state variable of the plastic material during the deformation. The hardening law was considered to be piecewise linear and isotropic,

$$\sigma_Y(\varepsilon_p) = \begin{cases} 0.5 + 5\varepsilon_p & \varepsilon_p \in [0, 0.04) \\ 0.7 + 2\varepsilon_p & \varepsilon_p \in [0.04, \infty) \end{cases} \text{ MPa.} \tag{5.32}$$

The damage evolution law has a similar formulation proposed by [**99**], where the damage parameter d_m is defined as function of the effective plastic strain ε_p

$$d_m(\varepsilon_p) = \begin{cases} 0 & \text{if } \varepsilon_p \leq \varepsilon^{\text{cr}} \\ 1 - \dfrac{\varepsilon^{\text{cr}}}{\varepsilon_p} \exp(-\alpha(\varepsilon_p - \varepsilon^{\text{cr}})) & \text{if } \varepsilon_p > \varepsilon^{\text{cr}} \end{cases} \tag{5.33}$$

where α denotes the evolution rate and ε^{cr} is the critical effective plastic strain at damage initiation. Since the damage process is irreversible, $\alpha \geq 0$. If $\alpha = 0$, the material is purely elasto-plastic with no damage. For positive α, a fully damaged condition ($d_m = 1$) will be achieved at a finite ε_p. In this section, the damage evolution rate and critical effective plastic strain are chosen to be constant,

$$\alpha_0 = 100, \quad \varepsilon_0^{\text{cr}} = 0.02. \tag{5.34}$$

Three loading directions in terms of the macroscopic strain $\boldsymbol{\varepsilon}_M$ are considered:
1) uniaxial-strain condition [1 0 0]

$$\{\varepsilon_M\}_{11} = \bar{\varepsilon}, \quad \{\varepsilon_M\}_{22} = 0, \quad \{\varepsilon_M\}_{12} = 0; \tag{5.35}$$

2) biaxial-strain condition [1 1 0]

$$\{\varepsilon_M\}_{11} = \bar{\varepsilon}, \quad \{\varepsilon_M\}_{22} = \bar{\varepsilon}, \quad \{\varepsilon_M\}_{12} = 0; \tag{5.36}$$

3) shear-strain condition [1 -1 0]

$$\{\varepsilon_M\}_{11} = \bar{\varepsilon}, \quad \{\varepsilon_M\}_{22} = -\bar{\varepsilon}, \quad \{\varepsilon_M\}_{12} = 0; \tag{5.37}$$

where $\bar{\varepsilon}$ denotes the magnitude of the macroscopic strain.

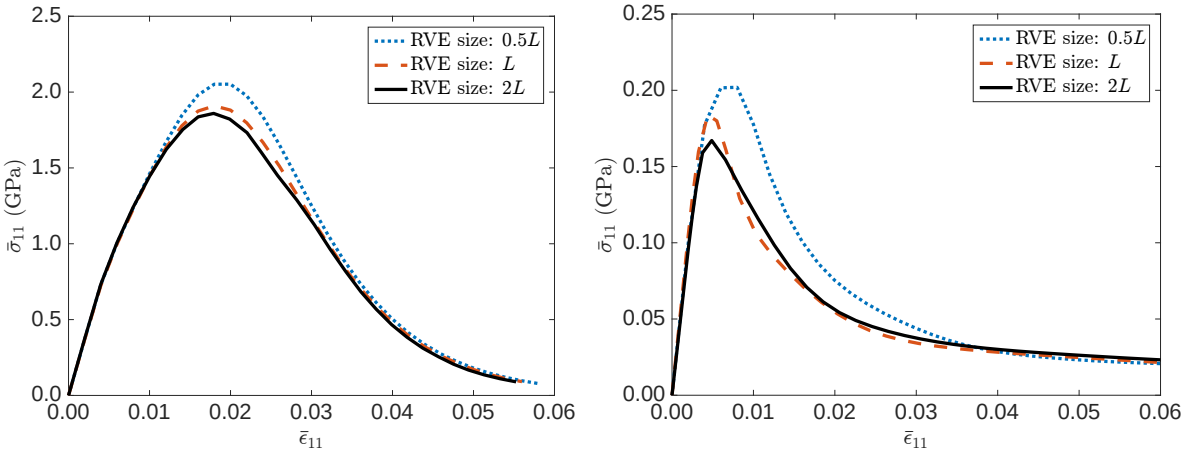

Figure 5.3. The DNS results given by the three-step homogenization for damaged RVEs with hard (left) and soft (right) inclusions under uniaxial loading.

For each step in the proposed three-step homogenization scheme, the computations are performed by a finite element model with periodic boundary conditions. Standard FEM is used for the first two steps, whereas a user-material (UMAT) is implemented to take the damage parameter into account in the third step.

The homogenized stress-strain curves $\{\sigma_M^d\}_{11}$-$\{\varepsilon_M\}_{11}$ for the damaged RVEs loaded in the uniaxial-strain condition [1 0 0] are shown in Figure 5.3. The subscript 11 indicates the tensor component in the 11 direction. For both hard and soft inclusions, it can be concluded that the macroscopic responses given by the three-step homogenization scheme are not sensitive to the RVE size.

Furthermore, the material toughness of all the RVEs under three different loading conditions are provided in Table 5.1. For RVEs with size $0.5L$ and L, the relative differences to the corresponding prediction from RVE with size $2L$ are also given within the parenthesis in the table. Specifically, the material toughness U_T is defined as the energy

Table 5.1. Comparison of the composite toughness U_T obtained from the DNS for RVE size $0.5L$, L, and $2L$. Value in parenthesis indicates relative difference to the corresponding prediction from RVE with size $2L$, toughness units are GPa.

	Hard inclusion		
	Uniaxial	Biaxial	shear
$0.5L$	0.0829(12.8%)	0.3240(5.5%)	0.0111(8.0%)
L	0.0749(1.9%)	0.3184(3.6%)	0.0104(1.1%)
$2L$	0.0735	0.3072	0.0103
	Soft inclusion		
	Uniaxial	Biaxial	shear
$0.5L$	0.0056(22.5%)	0.0060(22.0%)	0.0075(9.8%)
L	0.0044(3.0%)	0.0049(1.2%)	0.0070(2.8%)
$2L$	0.0046	0.0049	0.0068

per unit volume absorbed before material failure due to load in a fixed loading direction. In a one-dimensional case, the material toughness is simply the area under a stress-strain curve. In general, this is expressed mathematically as

$$U_T = \int_{\mathbf{0}}^{\boldsymbol{\varepsilon}_M^f} \boldsymbol{\sigma}_M^d d\boldsymbol{\varepsilon}_M, \tag{5.38}$$

where $\boldsymbol{\varepsilon}_M^f$ is the failure strain for a fully damaged material ($d_M = 0.99$ was used as the failure strain in this calculation). As we can see from the table, the relative difference of the material toughness decreases with the RVE size, and the existence of RVE is also validated. Therefore, no material length parameter needs to be defined in the microscale, and this RVE homogenization provides an effective material damage model for a macroscale material point within a concurrent simulation.

5.4. Comparison between SCA and DNS

The SCA reduced order method is first applied to an elasto-plastic RVE without considering material damage. The clustering database is determined in the offline stage

using hard inclusions, and the same material database is utilized for both hard and soft inclusions in the online stage.

Three loading directions in terms of the macroscopic strain are considered: 1) uniaxial tension, 2) biaxial tension, and 3) shear. The homogenized stress strain curves in the 11 direction ($\{\sigma_M\}_{11} - \{\varepsilon_M\}_{11}$) of the undamaged RVE with hard and soft inclusions are presented in Figure 5.4. The numbers of clusters considered in material phase 1 are 1 and 256, and the corresponding DNS results are plotted as the solid lines for comparison. Analysis of the plots for hard inclusions shows that the SCA predictions under all the

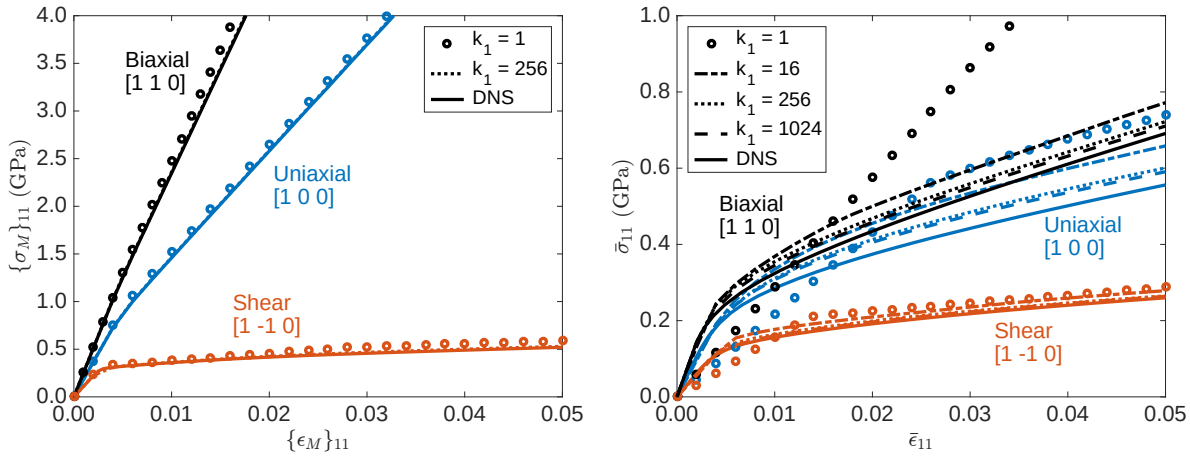

Figure 5.4. The stress-strain curves of the undamaged RVE with hard (left) and soft (right) inclusions.

three macro-strain constraints are quite accurate with only one cluster in phase 1. For soft inclusions, it is not possible to achieve the same accuracy with the same number of clusters. The right-hand side of Figure 5.4 shows that $k_1 = 1$ is not sufficient to capture the stress-strain relation in the elastic or plastic regimes, especially for the uniaxial and biaxial loading conditions. This observation is consistent with the fact that the self-consistent theory in analytical micromechanics methods tends to underestimate the stiffness of porous materials. Nevertheless, by increasing the resolution in the RVE, a good agreement with the DNS results can still be achieved, and with significantly fewer degrees of freedom than required by DNS.

The SCA reduced order method is next applied to an elasto-plastic RVE when material damage is considered. SCA predictions before the energy regularization are shown in Figure 5.5, 5.6 and 5.7, and DNS results are provided for comparison. With the same level of discretization, the SCA predictions with material damage considered do not exhibit the same level of accuracy as the SCA predictions without considering material damage. This difference is expected since material damage is a more localized process than plasticity, and more clusters are required for adequate resolution in the damaged region.

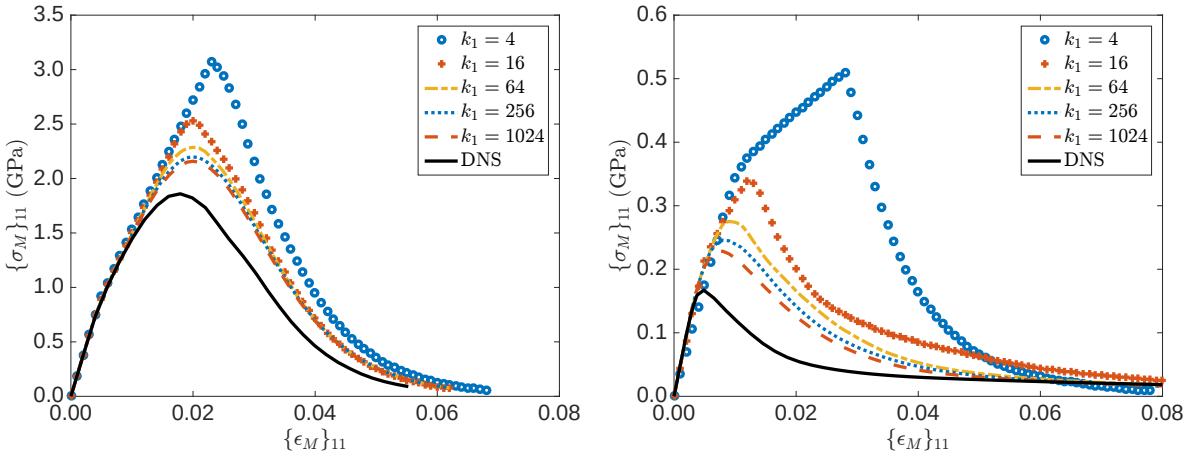

Figure 5.5. The stress-strain curves of the damaged RVE with hard (left) and soft (right) inclusions under uniaxial loading.

Furthermore, the macroscopic material damage behavior can be characterized by the material toughness U_T as a function of $\bar{\varepsilon}_{avg}/\bar{\varepsilon}_R$, where $\bar{\varepsilon}_{avg}$ and $\bar{\varepsilon}_R$ denote the macroscopic normal strain and principle shear strain, respectively. Due to the isotropy of the RVE considered in this work, the material toughness should be uniquely determined by the loading direction denoted by $\bar{\varepsilon}_{avg}/\bar{\varepsilon}_R$. For a given set of $\bar{\varepsilon}_{avg}$ and $\bar{\varepsilon}_R$, the loading condition is defined to be

$$\varepsilon_M^{11} = \bar{\varepsilon}_{avg}, \varepsilon_M^{22} = \bar{\varepsilon}_{avg}, \varepsilon_M^{12} = \bar{\varepsilon}_R. \tag{5.39}$$

The material toughness U_T is defined in Eq. (5.38). In each loading path for computing the material toughness, the loading direction or the ratio $\bar{\varepsilon}_{avg}/\bar{\varepsilon}_R$ is fixed.

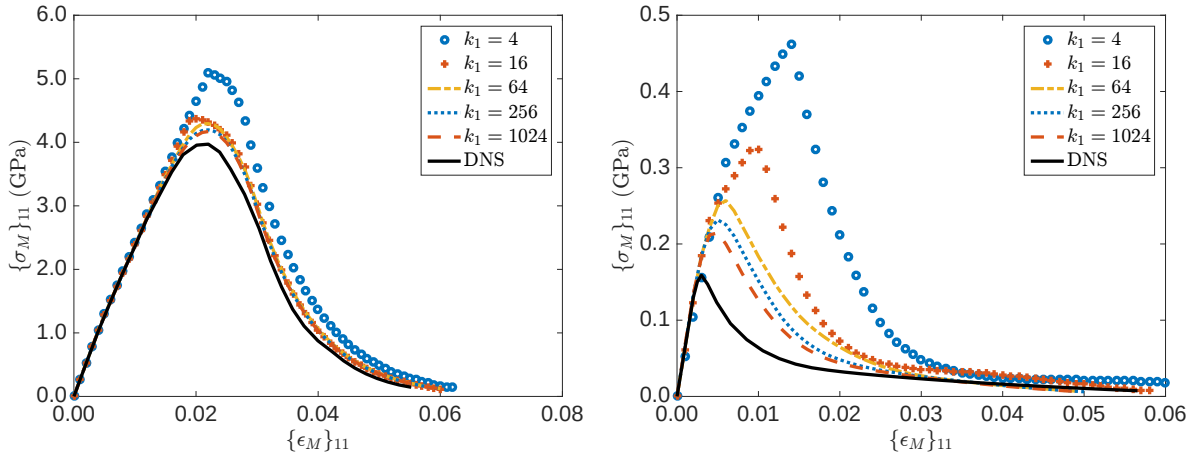

Figure 5.6. The stress-strain curves of the damaged RVE with hard (left) and soft (right) inclusions under biaxial loading.

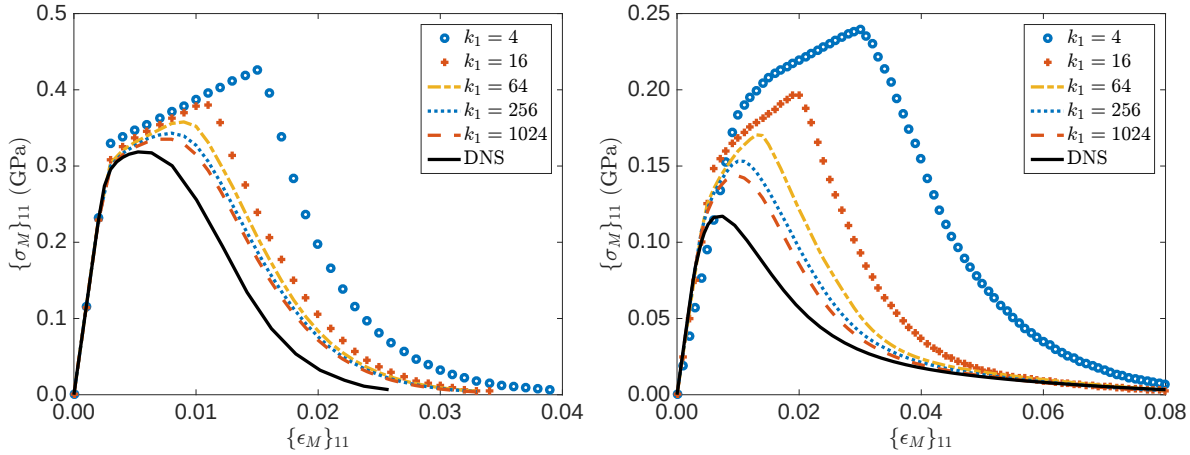

Figure 5.7. The stress-strain curves of the damaged RVE with hard (left) and soft (right) inclusions under shear loading.

Figure 5.8 shows the material toughness U_T of the RVE as a function of the ratio of $\bar{\varepsilon}_{avg}$ to $\bar{\varepsilon}_R$. For hard inclusions, the toughness decreases monotonically with $\bar{\varepsilon}_R/\bar{\varepsilon}_{avg}$, and overall effective toughness is higher under the biaxial loading than by pure shearing loading by more than one order of magnitude. Similar to the matrix material, the effective damage evolution of the RVE with hard inclusions is dominated by the deviatoric part of the average stress, resulting in a low toughness under the pure shearing loading.

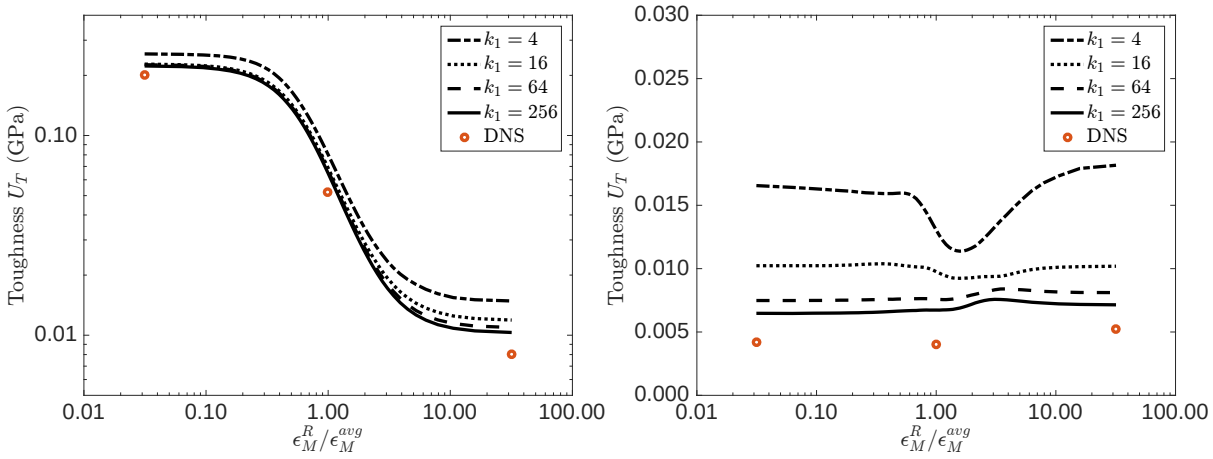

Figure 5.8. The material toughness predictions for RVEs with hard (left) and soft (right) inclusions.

Again, it should be emphasized that although the SCA database is created based on the RVEs with hard inclusions, it is valid for other RVEs with the same morphology but different combinations of material properties. As a result, the SCA database (clusters and the interaction tensor $\mathbf{D}^{IJ}$) can be regarded as a microstructural database which characterizes the geometric heterogeneity of the material and enables the online reduced-order calculation.

5.5. Energy regularization of the three-step scheme

The damage model should correctly reflect the energy dissipation in the macroscale fracture process. As a result, parameters in the damage evolution law need to be adjusted according to the measured fracture energy G_c under a given loading direction. Mathematically, it should have

$$G_c = G_c^{DNS}(\alpha_0, \varepsilon_0^{\mathrm{cr}}) = G_c^{SCA,k}(\alpha, \varepsilon^{\mathrm{cr}}), \tag{5.40}$$

where k denotes the number of clusters in the SCA reduced-order model. The fracture energy G_c represents the dissipated energy due to fracture per unit crack area in 3D (or per unit crack length in 2D) in the macroscale, which serves as a physical material constant and should not depend on the choice of numerical models. Given a length parameter l_h

from the macroscale model, G_c can be expressed as

$$G_c = l_h U_F(\alpha, \varepsilon^{\mathrm{cr}}), \tag{5.41}$$

where U_F represented the energy dissipated by fracture per unit volume at a material point. It can be calculated based on the dissipation rate Y_m defined in Eq. (5.14),

$$U_F = \int_0^\infty \left(\int_\Omega Y_m \dot{d}_m d\Omega \right) dt, \tag{5.42}$$

If there is no plasticity inside the RVE, U_F is equal to the material toughness U_T in Eq. (5.38), which indicates that all the work (density) is dissipated by fracture. Although U_F can only be strictly calculated using Eq. (5.41), I will use U_T to approximate U_F if the portion of energy dissipated by plasticity is relatively low. As a result, the fracture energy of the RVE can be approximated by

$$G_c \approx l_h U_T(\alpha, \varepsilon^{\mathrm{cr}}), \tag{5.43}$$

Although the fracture energy G_c is usually measured experimentally, for demonstration purposes, I will treat the DNS results as the reference solution, and calibrate the damage evolution rate α and the critical plastic strain $\varepsilon^{\mathrm{cr}}$ in the SCA model to satisfy the energy consistency. Since the length parameter l_h is determined by the macroscale model, one only needs to match the material toughness between SCA and DNS:

$$U_T^{SCA,k}(\alpha, \varepsilon^{\mathrm{cr}}) = U_T^{DNS}(\alpha_0, \varepsilon_0^{\mathrm{cr}}). \tag{5.44}$$

The damage parameters α_0 and $\varepsilon_0^{\mathrm{cr}}$ in DNS are listed in Eq. (5.34). On the other hand, it is also important to match the maximum stress σ_c during the loading process, which corresponds to ultimate strength of the material.

$$\sigma_c^{SCA,k}(\alpha, \varepsilon^{\mathrm{cr}}) = \sigma_c^{DNS}(\alpha_0, \varepsilon_0^{\mathrm{cr}}). \tag{5.45}$$

The damage parameters in SCA are calibrated under uniaxial loading condition. Figure 5.9, 5.10 and 5.11 show the stress-strain curves predicted by SCA after the energy

Table 5.2. Calibrated α and ε^{cr} in SCA with different numbers of clusters

	hard		soft	
	α	ε^{cr}	α	ε^{cr}
$k_1 = 4$	52	0.0092	100	0.0015
$k_1 = 8$	62	0.0112	60	0.0015
$k_1 = 16$	63	0.0120	60	0.0020
$k_1 = 32$	67	0.0128	50	0.0020
$k_1 = 64$	72	0.0134	40	0.0020
$k_1 = 128$	77	0.0140	30	0.0020
$k_1 = 256$	81	0.0146	30	0.0025
DNS	100	0.02	100	0.02

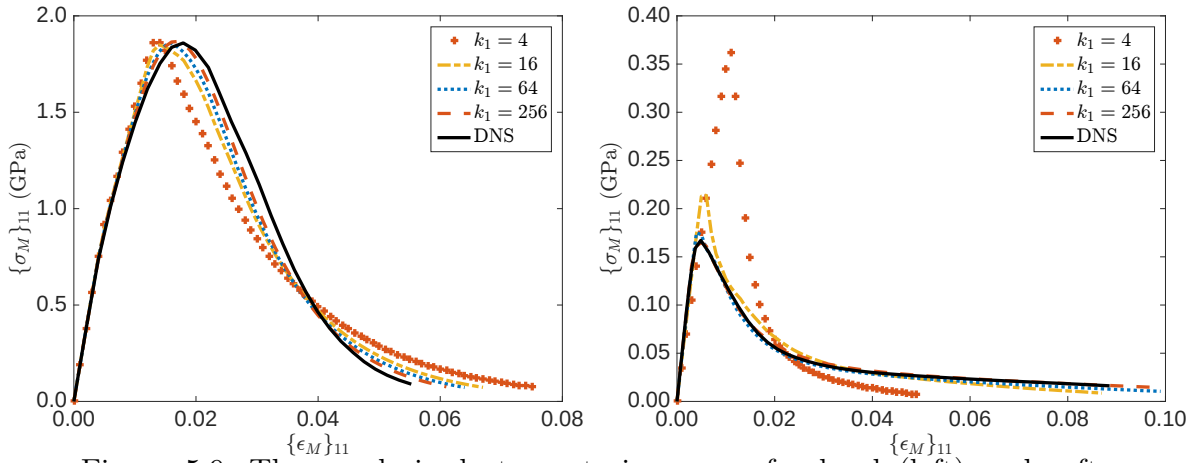

Figure 5.9. The regularized stress-strain curves for hard (left) and soft (right) inclusions under uniaxial loading.

regularization under all three loading conditions for both hard and soft inclusions. Table 5.2 lists the values for calibrated $(\alpha, \varepsilon^{\text{cr}})$. For the material with hard inclusions, it is possible to match the peak stress with very few clusters. For the material with soft inclusions, more clusters ($k_1 > 16$) are required to match both the peak stress and the damage evolution curve.

Since the damage parameters are calibrated only for uniaxial loading condition, the regularized stress-strain curves under the other two loading conditions can not be matched

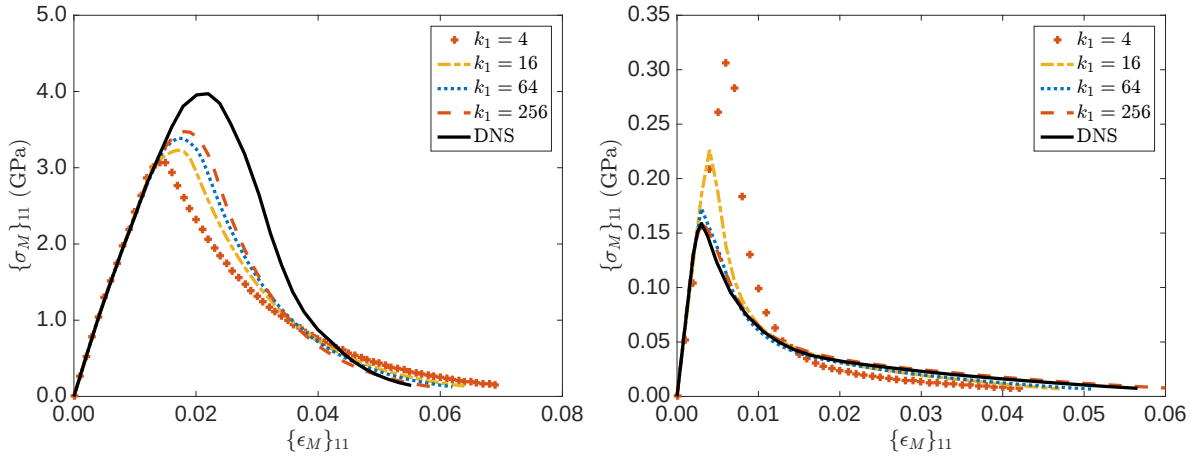

Figure 5.10. The regularized stress-strain curves for hard (left) and soft (right) inclusions under biaxial loading.

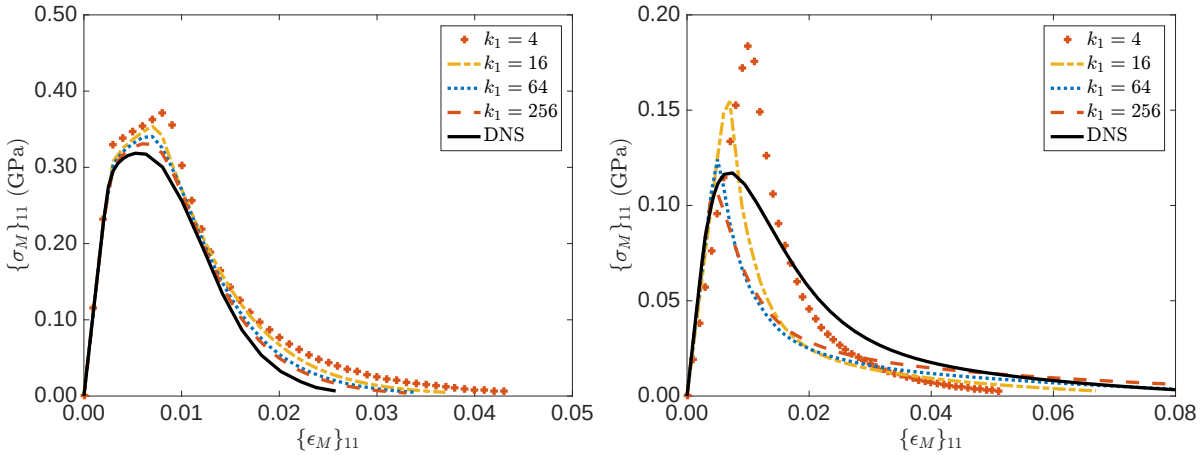

Figure 5.11. The regularized stress-strain curves for hard (left) and soft (right) inclusions under shear loading.

exactly. However, as we can see from the Figure 5.12, the agreement of the toughness between SCA and DNS results becomes much better within the whole spectrum of loading direction after the regularization, especially for RVEs with soft inclusions. Using a small number of clusters, the SCA reduced order model with calibrated damage parameters can achieve good accuracy against DNS results.

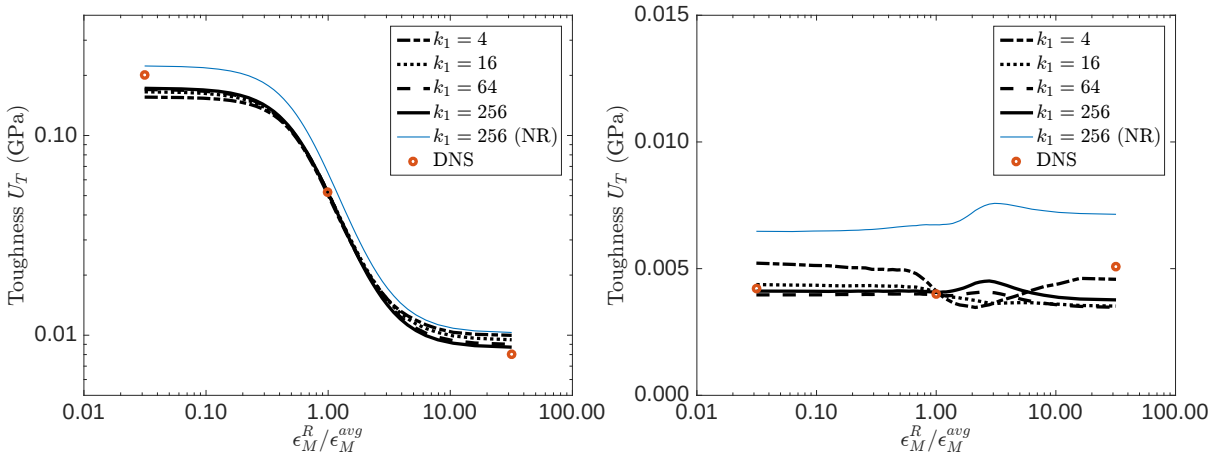

Figure 5.12. The material toughness predictions after regularization for hard (left) and soft (right) inclusions.

5.6. Nonlocal formulation in macroscale

The macroscopic damage is based on the microscale damage computed using the proposed three-step micro-damage algorithm. The algorithm captures the complex damage mechanisms due to material heterogeneities at the microstructural level without predefining the form or requiring a length scale. This is achieved at a local macroscopic point by homogenizing the damaged stress computed in the microscale RVE. Although the microscale damage model does not require a nonlocal length scale, the macroscale model is still subject to the mesh-size dependency and pathological mesh dependency when the homogenized results from the RVE are passed back to the macroscale material point. To resolve those issues, a nonlocal macroscale damage formulation is adopted in this work.

Before introducing nonlocal regularization or gradient damage approach, it is well-known that the damage band will be localized in a single layer of element after strain softening [**7**]. As a result, the length parameter l_h is related to the characteristic length of the finite elements in the macroscale. Note that if there is no energy dissipation before the strain-softening regime, l_h will be directly related to the mesh size l_e of a finite element model with square elements,

$$l_h = \frac{l_e}{\cos(\gamma)}, \tag{5.46}$$

where $|\gamma| < \pi/4$ is the angle of the mesh lines with the crack direction. Similar to the crack band theory [**7**], the material toughness in the RVE needs to be calibrated based on the choice of l_h to avoid the mesh-size dependency and retain a physical fracture energy,

$$U_T = G_c/l_h. \tag{5.47}$$

However, the local model still suffers from the pathological mesh dependence, that is, spurious sensitivity to the arrangement and shape of the mesh. That's why the nonlocal damage formulation comes into picture. A nonlocal macroscopic length scale is introduced via a convolution integral. The nonlocal effective plastic strain, $\tilde{\varepsilon}_p$, at point $\mathbf{x}$ inside the RVE is obtained as a weighted average over a spatial neighborhood of the macroscale point $\boldsymbol{\xi}$ under consideration,

$$\tilde{\varepsilon}_p(\mathbf{x}, \boldsymbol{\xi}) = \int_{\mathrm{B}} \omega(||\boldsymbol{\xi} - \boldsymbol{\xi}'||)\varepsilon_p(\mathbf{x}, \boldsymbol{\xi}')d\boldsymbol{\xi}', \tag{5.48}$$

where $\varepsilon_p(\mathbf{x}, \boldsymbol{\xi}')$ is the local effective plastic strain at a microscale point $\mathbf{x}$ inside the RVE associated with macroscale point $\boldsymbol{\xi}'$. Then, the nonlocal damage parameter can be calculated based on the effective plastic strain,

$$\tilde{d}_m = \tilde{d}_m(\tilde{\varepsilon}_p) \tag{5.49}$$

The clustering domain decomposition utilized for the reduced order self-consistent clustering method leads to a discrete form of the convolution integral. The nonlocal effective plastic strain in the I-th cluster $\tilde{d}_m^I$ at point $\boldsymbol{\xi}$ of a reduced order RVE can be written as

$$\tilde{\varepsilon}_p^I(\boldsymbol{\xi}) = \int_{\mathrm{B}} \omega(||\boldsymbol{\xi} - \boldsymbol{\xi}'||)\varepsilon_p^I(\boldsymbol{\xi}')d\boldsymbol{\xi}', \tag{5.50}$$

where $d_m^I(\boldsymbol{\xi}')$ is the local damage parameter in the I-th cluster of the reduced RVE at point $\boldsymbol{\xi}'$. Similarly, the nonlocal damage parameter in the I-th cluster can be computed,

$$\tilde{d}_m^I = \tilde{d}_m^I(\tilde{\varepsilon}_p^I). \tag{5.51}$$

The nonlocal weighting function $\omega(||\boldsymbol{\xi}-\boldsymbol{\xi}'||)$ is normalized to preserve a uniform field,

$$\omega(||\boldsymbol{\xi}-\boldsymbol{\xi}'||) = \frac{\omega_\infty(||\boldsymbol{\xi}-\boldsymbol{\xi}'||)}{\int_B \omega_\infty\left(||\boldsymbol{\xi}-\boldsymbol{\xi}'||\right) d\boldsymbol{\xi}'}, \tag{5.52}$$

where B denotes the macroscale support domain for the nonlocal integration. One possible weighting function, which was utilized for the examples in this work, is a polynomial bell function with compact support [**6**],

$$\omega_\infty(r) = \left\langle 1 - \frac{4r^2}{l_0^2} \right\rangle^2, \tag{5.53}$$

where the Macauley brackets $\langle ... \rangle$ are defined as $\langle x \rangle = \max(x, 0)$, and l_0 is the macroscale length scale parameter. Since $\omega_\infty(r)$ vanishes for $r > l_0/2$, the support domain B is circular in two-dimensions, or spherical in three-dimensions, with a radius $l_0/2$. Another possible choice of the weighting function often used in literature is a normalized Gaussian function,

$$\omega_\infty(r) = (l_0\sqrt{\pi/2})^{-N_{dim}} \exp(-\frac{2r^2}{l_0^2}), \tag{5.54}$$

where N_{dim} denotes the number of spacial dimensions.

The macroscale nonlocal length parameter, l_0, determines the width of the damage localization band, and limits localization to ensure numerical convergence to a physically meaningful solution. The nonlocal microscale damage parameter $\tilde{d}_m$ (or $\tilde{d}_m^I$) is utilized in RVE3, resulting in a microscale stress-strain relation in Eq. (5.25) of

$$\boldsymbol{\sigma}_{m3} = (1-\tilde{d}_m)\mathbf{C}_m : \boldsymbol{\varepsilon}_{m3}. \tag{5.55}$$

For the new three-step homogenization with the nonlocal formulation, the nonlocal microscale damage parameter $\tilde{d}_m$ is computed in the third step, and the effect of $\tilde{d}_m$ will propagate to macroscale through homogenization of the third RVE.

Furthermore, the length parameter l_h in the energy regularization is related to the nonlocal length parameter l_0,

$$l_h = \beta l_0 \tag{5.56}$$

where β is an empirical parameter characterizing the strain distribution within the localized damage band, which relates to the choice of the nonlocal weighting function. It usually ranges between 1.0 and 1.8 in the literature.

In the following example, the damage parameter α and ε^{cr} in the SCA model are calibrated to give the same maximum stress and fracture energy for three different length parameters $l_h = 1.0$, 2.0 and 4.0 mm. Uniaxial tension loading condition is considered. The SCA model has 32 clusters in the matrix phase ($k_1 = 32$), and hard inclusions are considered in the RVE. For all the cases, the maximum stress and fracture energy in 2D are

$$\sigma_c = 1.85 \text{ GPa}, \quad G_c = 0.104 \text{ GPa} \cdot \text{mm} \tag{5.57}$$

The calibrated $(\alpha, \varepsilon^{\text{cr}})$ are provided in Table 5.3. The stress-strain curves for different

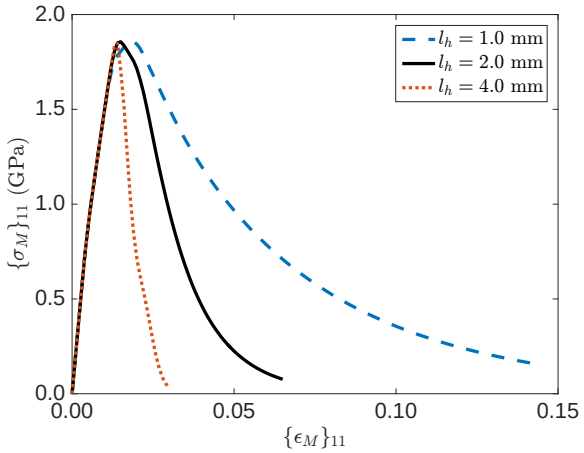

Figure 5.13. Calibrated SCA stress-strain curves under uniaxial tension for length parameter $l_h = 1.0$, 2.0, and 4.0 mm.

length parameters l_h are shown in Figure 5.13.

5.7. Concurrent multiscale simulations

Concurrent multiscale simulations involving strain softening and localization are performed under two-dimensional plane strain condition. The proposed three-step micro-damage homogenization scheme coupled with the SCA method is used. In these examples,

Table 5.3. Calibrated α and ε^{cr} for different length parameters l_h

	$l_h = 4.0$ mm	$l_h = 2.0$ mm	$l_h = 1.0$ mm
α	540	67	17
ε^{cr}	0.0147	0.0128	0.011
U_T(GPa)	0.026	0.052	0.104

the macroscale properties are determined by the microstructural morphologies and the microscale constituents. The SCA material database is compiled during the offline stage, greatly reducing the computational cost of analyzing the microscale RVE model with minimal loss of accuracy, and making the concurrent simulation computationally feasible. The homogenized material can predict the macroscale performance while capturing the physical phenomena appearing in the microscale.

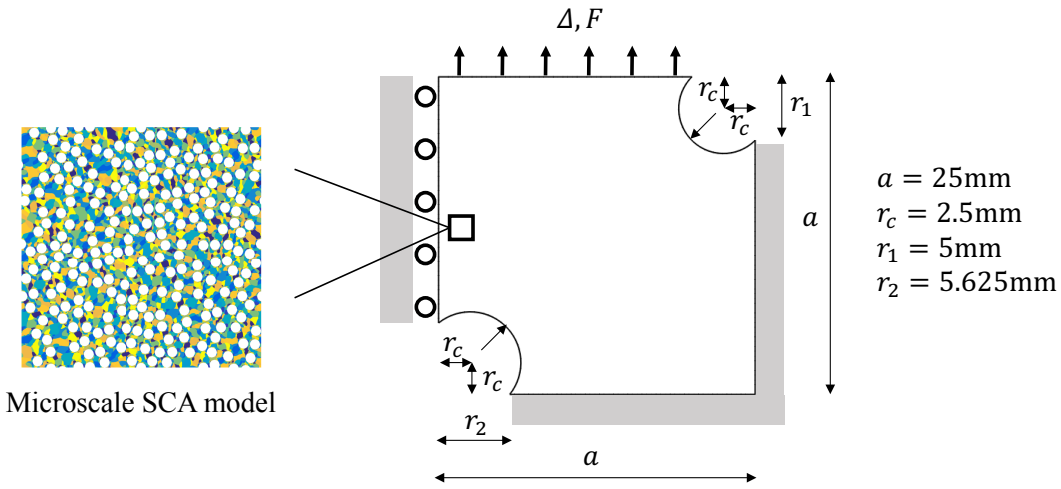

Figure 5.14. Geometry of the double-notched plate in 2D plane-strain condition.

A 2D tensile specimen with rounded notches in two corners [**81**] is depicted in Fig. 5.14. The notches in the opposite corners induces a geometric stress concentration which will induce localization as the loaded upper edge of the specimen is displaced. The material properties used for the matrix and the inclusion material are given in Section 5.3; both hard and soft inclusions are analyzed. The simulations are conducted using the explicit finite element method in ABAQUS/Explicit and the 2D plane strain element with reduced

integration (one integration point per element), and the micro-damage algorithm with the SCA model is implemented as a user-defined material (VUMAT). Specifically, LU decomposition in the Intel ® Math Kernel Library (MKL) is utilized for solving the linear systems in the SCA model. The macroscopic element will be deleted when the effective damage parameter d_M of its associated RVE reaches 0.99.

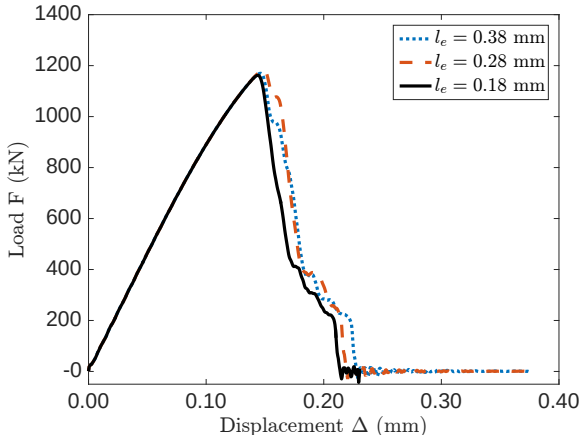

Figure 5.15. Load-displacement curves with different mesh size l_e for hard inclusions. The nonlocal length parameter is $l_0 = 2$ mm.

The effectiveness of the nonlocal formulation is first investigated. The energy regularization is not considered. RVE with hard inclusions is considered in the microscale, and the SCA database has 32 clusters in the matrix phase. Figure 5.15 presents the load-displacement curves from the concurrent simulations for three different FE mesh sizes in the macroscale $l_e = 0.18, 0.28, 0.38$ mm (illustrated in Figure 5.16), and the nonlocal length parameter is $l_0 = 2$ mm. Moreover, the crack patterns after the coupon failure for all three mesh sizes are also shown in Figure 5.16. It can be concluded that given $l_0 > 4l_e$, the nonlocal formulation can effectively diminish the mesh-size dependency, as well as the pathological mesh-shape dependency.

Figure 5.17 shows the load-displacement curves of RVEs with hard or soft inclusions predicted by the concurrent simulation before the energy regularization. The numbers of clusters in phase 1 in the microscale reduced-order model ranges from 4 to 64. Since

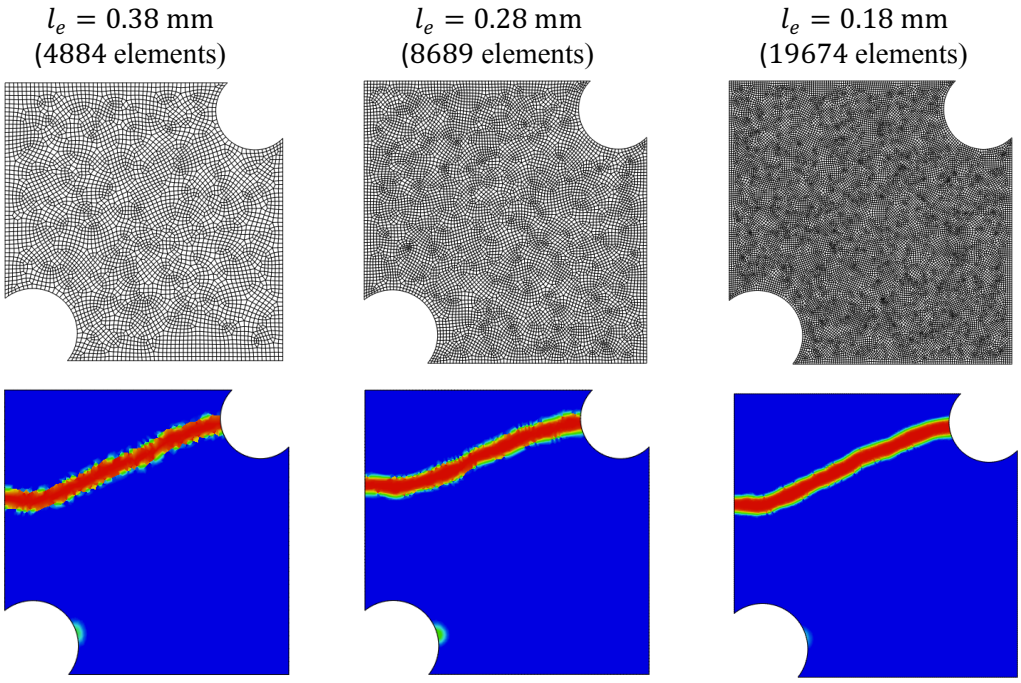

Figure 5.16. Crack patterns with different mesh size l_e for hard inclusions. The nonlocal length parameter is $l_0 = 2$ mm. The SCA model has 32 clusters in the matrix phase ($k_1 = 32$).

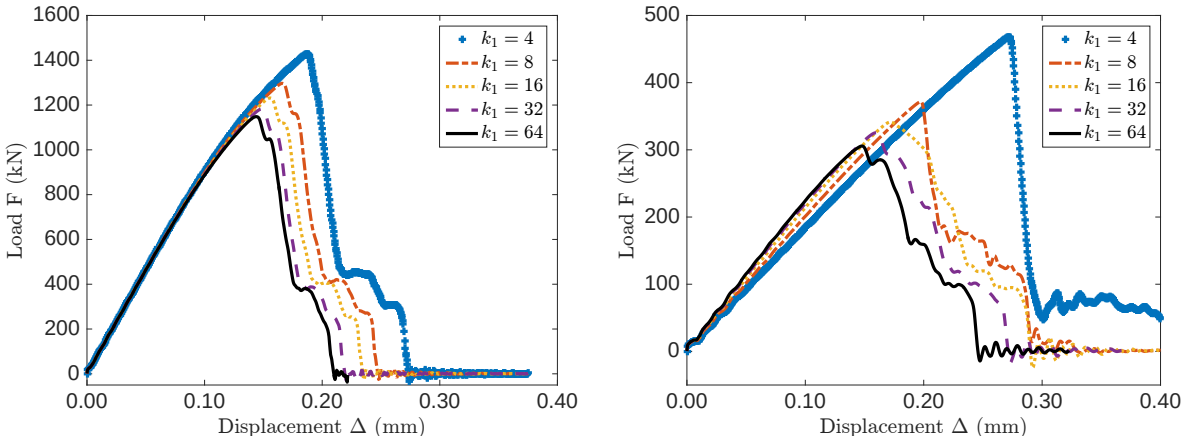

(a) Hard inclusions before regularization

(b) Soft inclusions before regularization

Figure 5.17. Load-displacement curves predicted by SCA databases with different number clusters k_1 before the energy regularization.

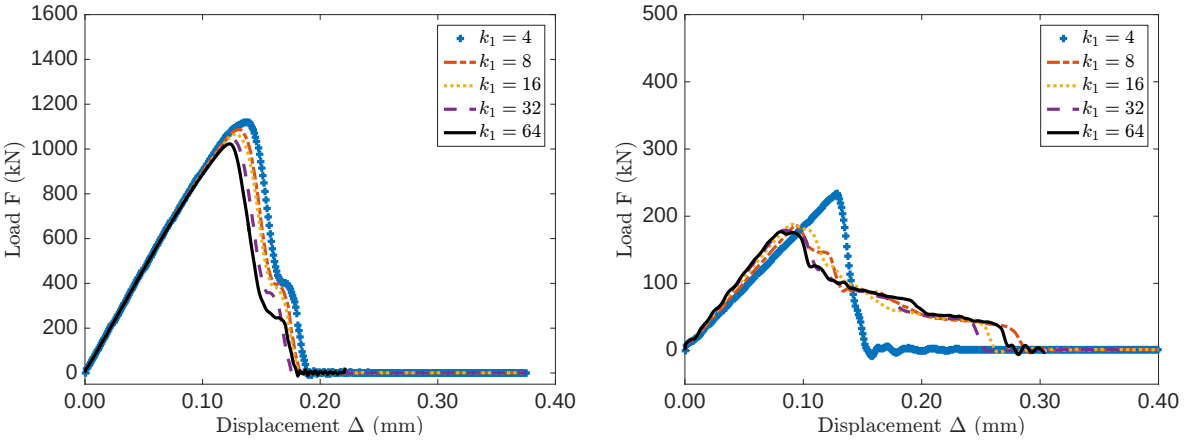

(a) Hard inclusions after regularization

(b) Soft inclusions after regularization

Figure 5.18. Load-displacement curves predicted by SCA databases with different number clusters k_1 after the energy regularization.

the concurrent simulation with microscale RVE modeled by DNS is extremely time-consuming, the multiscale DNS results are not provided for comparison. A better convergence is observed in models with hard inclusions than those with soft inclusions, and the prediction has a higher fidelity in the elasto-plastic regime than in the strain-softening regime. Increasing the number of clusters in the microscale clearly improves the prediction, but the convergence rate is not satisfactory, similarly to the observations in the RVE homogenization.

Therefore, energy regularization needs to be introduced. The calibrated damage parameters for different numbers of clusters have been provided in Table 5.2. The Load-displacement curves from the concurrent simulations after regularization are shown in Figure 5.18, and we can see that the accuracy and convergence rate with respect to the cluster number have been improved, for both hard and soft inclusions. Meanwhile, Figure 5.19 presents the crack patterns from concurrent simulations after regularization, and they become consistent as the number of cluster is increased. Although the same microstructure and SCA database have been used, the crack patterns for hard and soft inclusions are quite different. The influence of micro-constituent on the macro-responses is captured by the concurrent simulation driven by the SCA database.

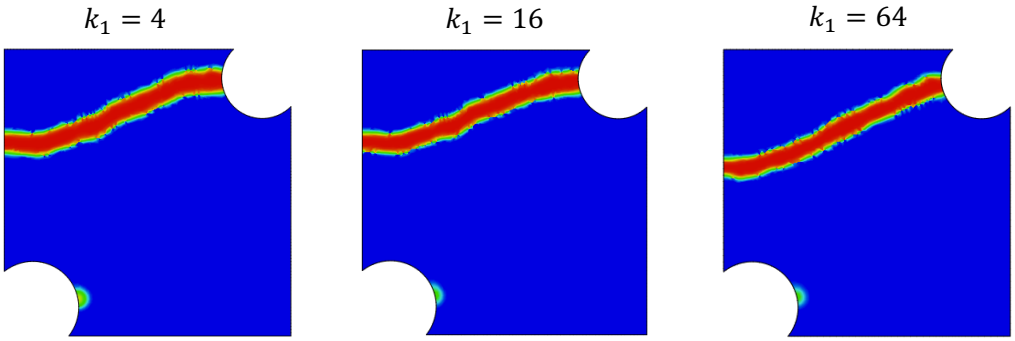

(a) Hard inclusions after regularization

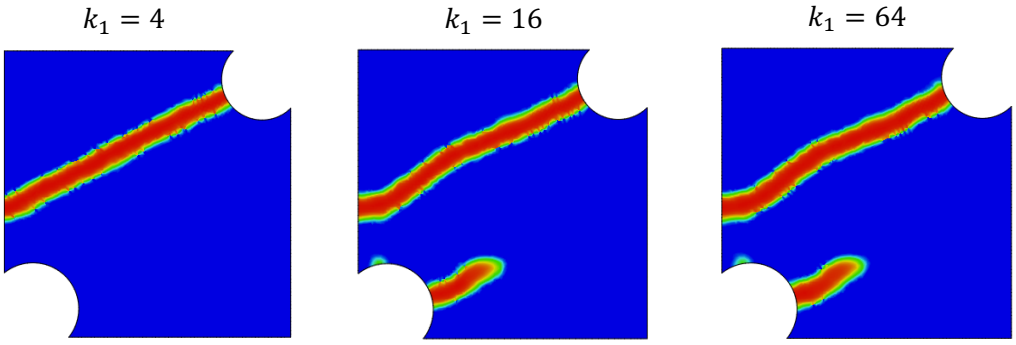

(b) Soft inclusions after regularization

Figure 5.19. Crack patterns predicted by SCA databases with different number clusters k_1 after the energy regularization.

In the next example, the effectiveness of the energy regularization for different nonlocal length parameter l_0 is demonstrated in a set of concurrent simulations, with $l_e = 0.28$ mm and $k_1 = 32$. Two nonlocal length parameters are considered: $l_0 = 2$ mm and $l_0 = 4$ mm. The calibrated damage parameters after the energy regularization can be found in Table 5.3, by assuming $\beta = 1$ and $l_0 = l_h$. Ideally, the simulations with the two length parameters should give the same results. It can be concluded from Figure 5.20 and 5.21 that the energy regularization effectively reduces the dependence on the length parameter, and yields consistent results for both load-displacement curves and crack patterns.

The computational times for the 2D concurrent simulations and k_1 ranging from 4 to 64 are listed in Table 5.4. The macroscale mesh size is $l_e = 0.28$ mm, and there are in total

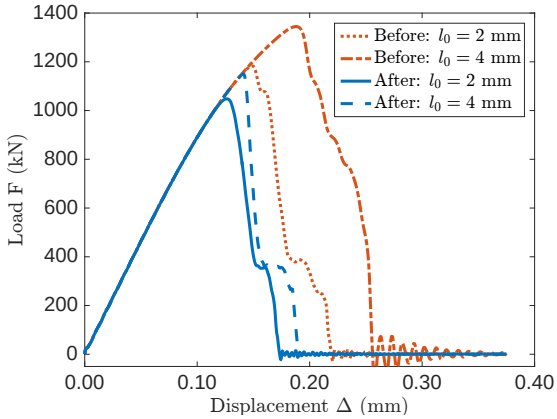

Figure 5.20. Load-displacement curves with different nonlocal length parameter l_0 for hard inclusions, before and after the energy regularization. The mesh size is $l_e = 0.28$ mm.

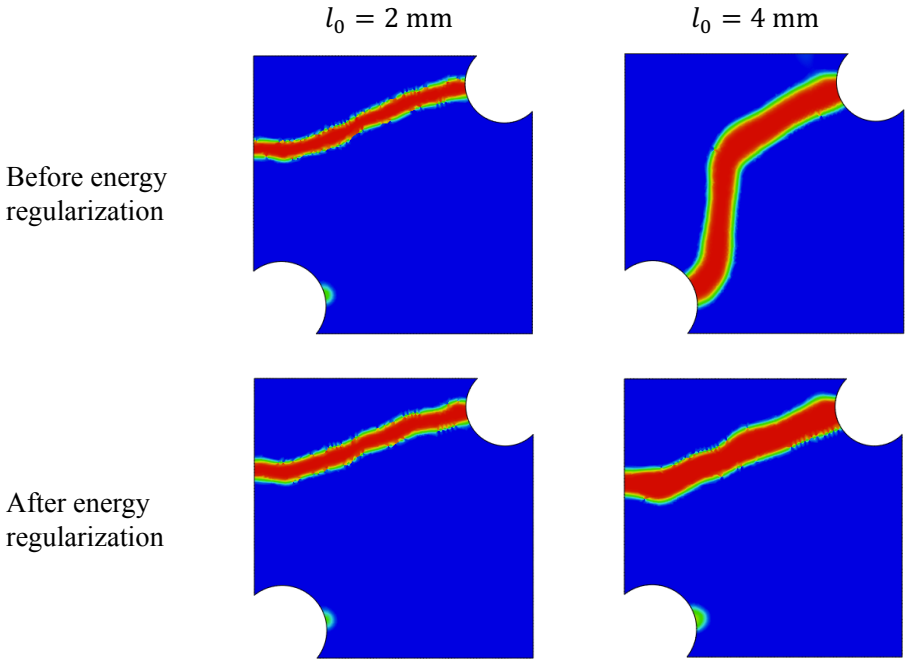

Figure 5.21. The crack patterns under different nonlocal length parameter parameter l_0 for hard inclusions, before and after the energy regularization. The mesh size is $l_e = 0.28$ mm. The SCA model has 32 clusters in the matrix phase ($k_1 = 32$).

Table 5.4. Computational time of the concurrent simulations of various numbers of clusters in phase 1 on 24 cores.

k_1	4	8	16	32	64
Wall clock time (min)	28	93	428	2662	20021
Wall clock time with MKL (min)	19	44	117	416	1948

8689 elements in the model. All the simulations are conducted on 24 cores (in a state-of-the art high performance computing cluster with the following compute nodes: Intel Haswell E5-2680v3 2.5 GHz 12-cores). By using the Intel ® Math Kernel Library (MKL), instead of the home-made matrix-inversion code, the efficiency of the computation can be greatly improved, especially for large number of clusters. This is also important in the 3D simulations, since the number of degrees of freedom (strain components) in each cluster increase from 3 to 6.

For the simulations with MKL, a linear scalability with the number of cores is observed for small number of clusters. When $k_1 > 16$, the computational time of the concurrent simulation increases approximately as the square of k_1. This is different from the observation in Figure 4.10 where the computational time for single-scale RVE homogenization (in MATLAB) is almost proportional to k_1. The reason is that the matrix inversion part in SCA online stage is implemented in FORTRAN using a LU decomposition from MKL library , while the intrinsic inversion operation in MATLAB has already been well optimized. In the future, other iterative inversion algorithms, such as conjugate gradient and generalized minimal residual method (GMRES), can be adopted to improve the efficiency of the concurrent code.

The three-step homogenization scheme and SCA method is further applied to 3D concurrent simulations for a thick double-notched coupon shown in Figure 5.22. The cross-section of the 3D coupon is same as the 2D one shown in Figure 5.14, and its boundary conditions are also same as the 2D ones. The thickness of the FE model is 10 mm. Since symmetric boundary conditions are applied on the back face on the X-Y plane (no displacement in the Z-direction), the total thickness of the simulated coupon is 20 mm. The characteristic mesh size of the macroscale model is $l_e = 0.38$ mm, and the

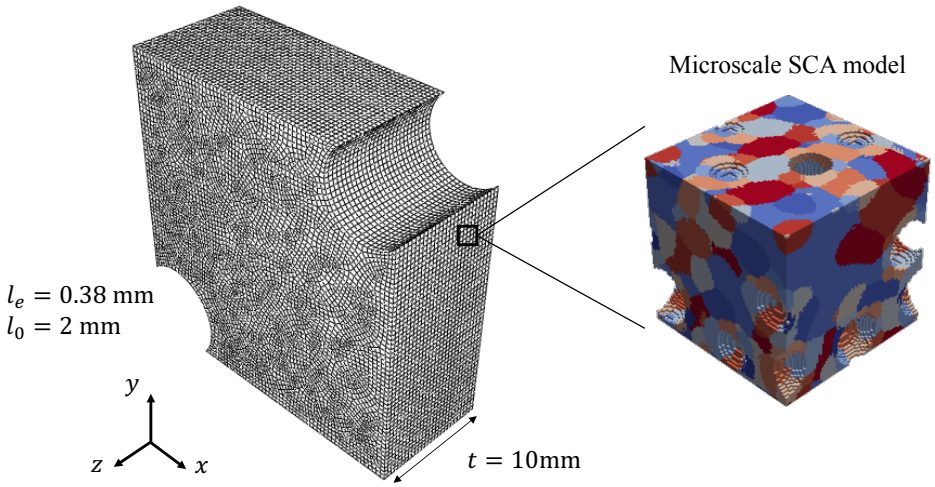

Figure 5.22. Geometry of the 3D thick double-notched coupon and microscale SCA model with 8 clusters in the matrix phase.

nonlocal length parameter is $l_0 = 2$ mm. In the macroscale FE model, there are in total 131625 3D hex elements with reduced integration. In the microscale SCA model, there are 8 clusters in the matrix phase and 2 clusters in the inclusion phase. Both RVEs with hard and soft inclusions are considered. All the material parameters are same as before. Specifically, the non-regularized damage parameters are used, which are provided in Eq. (5.34).

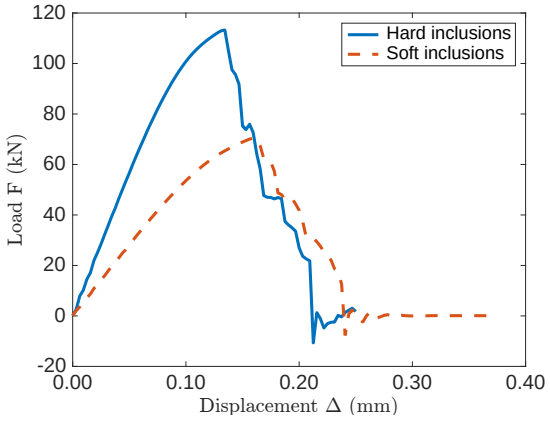

Figure 5.23. Load-displacement curves of the 3D concurrent simulations with hard and soft inclusions within the microscale RVE.

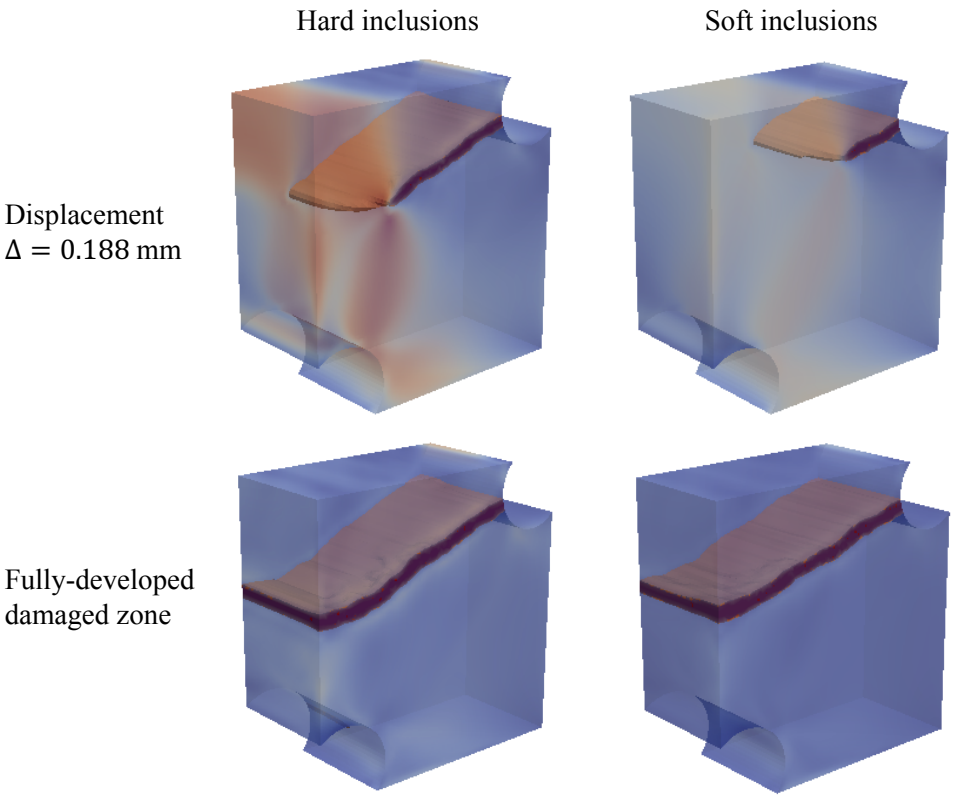

Figure 5.24. The crack patterns of the 3D concurrent simulations with hard and soft inclusions within the microscale RVE.

The load-displacement curves from the concurrent simulations with hard and soft inclusions are shown in Figure 5.23, and the crack patterns at different loading states are also provided in Figure 5.24. It can be observed that the concurrent simulations can capture the shear lip towards the outside edge, due to the constraint effects of a thick coupon. Due to the limitation of computational resources, convergence test and energy regularization have not been performed for the 3D problems yet, but these preliminary concurrent simulations demonstrate the capability of the SCA multiscale modeling framework for capturing the microstructural effect. By using 72 cores (Intel Haswell E5-2680v3 2.5 GHz 12-cores), the concurrent simulation with the Intel MKL library typically took around 24 hours. The same 3D concurrent modeling framework will be applied to unidirectional fiber composite in Section 6.2.

CHAPTER 6

Applications of Self-consistent Clustering Analysis to Nonlinear Material Systems

6.1. Polycrystal material with crystal plasticity

6.1.1. Background

This section will present a grain-level crystal plasticity model to capture local microstructures such as those that occur in additively manufactured material – e.g. columnar grains; the self-consistent clustering analysis (SCA) [**72**] will be used to vastly increase the speed of these simulations. This will allow for higher detail or larger regions of interest, both of which are desirable for predicting damage and fatigue initiation within a part.

Crystal plasticity in conjunction with the finite element method (termed CPFEM) has been applied to solve both microscopic and macroscopic problems, following from the early combinations of classical plasticity and the finite element method. It has two primary variants: polycrystal and single crystal plasticity. In the polycrystal formulation, each material point is assumed to represent a collection of crystals such that the overall response of the point is homogeneous. In single crystal plasticity, each material point is assumed to represent a single crystal, or a point in a single crystal, the deformation of which is governed by the particularities of single crystal deformation mechanics (e.g. active slip systems and/or dislocation motion). The former approach is more commonly used for macroscopic problems, where a relatively large solution volume is desired. The latter shall be the focus of this chapter and has been used to solve microscopic problems and obtain the macroscopic properties though homogenization. There are many versions of crystal plasticity laws in both forms. Here, the basic kinematics and material law of the version of McGinty and McDowell [**77**] are applied and will be discussed in the next section.

However, the main limitation of CPFEM or DNS method based on crystal plasticity is the computational cost. As a typical crystal plasticity model needs to solve a set of nonlinear equations at each integration, it is important to reduce the number of degrees of freedom to increase the computational efficiency. Here, the SCA method is extended to be applicable to crystal plasticity (CP) based on the material microstructure to capture the deformation mechanics of crystalline solids..

6.1.2. Kinematics

The deformation gradient $\mathbf{F}$ can be multiplicatively decomposed as:

$$\mathbf{F} = \mathbf{F}^e\mathbf{F}^p \tag{6.1}$$

where the plastic part $\mathbf{F}^p$ maps points in the reference configuration onto an intermediate configuration which is then mapped to a current configuration through the elastic part $\mathbf{F}^e$. Note that physically $\mathbf{F}^p$ is associated with the dislocation motion, and $\mathbf{F}^e$ is a combination of the elastic stretch and rigid body rotation.

The effect of dislocation motion is modeled by relating the plastic velocity gradient $\tilde{\mathbf{L}}^p$ in the intermediate configuration (usually denoted by $\tilde{\square}$) to simple shear deformation $\gamma^{(\alpha)}$:

$$\tilde{\mathbf{L}}^p = \sum_{\alpha=1}^{N_{\text{slip}}} \dot{\gamma}^{(\alpha)}(\tilde{\mathbf{s}}^{(\alpha)} \otimes \tilde{\mathbf{n}}^{(\alpha)}) \tag{6.2}$$

where $\otimes$ is the dyadic product, N_{slip} is the number of slip systems, $\dot{\gamma}^{(\alpha)}$ is a shear rate, $\tilde{\mathbf{s}}^{(\alpha)}$ is the slip direction, and $\tilde{\mathbf{n}}^{(\alpha)}$ is the slip plane normal, all for a crystal slip systems (α) in the intermediate configuration. The relationship between $\tilde{\mathbf{L}}^p$ and $\mathbf{F}^p$ is given by

$$\tilde{\mathbf{L}}^p = \dot{\mathbf{F}}^p \cdot \left(\mathbf{F}^p\right)^{-1}. \tag{6.3}$$

The final task in constructing the crystal plasticity framework is defining the constitutive laws of elasto-plasticity. A basis of the Green-Lagrange strain $\mathbf{E}^e$ and Second Piola-Kirchhoff stress $\mathbf{S}^e$ is chosen from the many conjugate pairs available, which are related

by:

$$\mathbf{S}^e = \tilde{\mathbf{C}} \cdot \mathbf{E}^e = \frac{1}{2}\tilde{\mathbf{C}} \cdot \left[(\mathbf{F}^e)^{\mathrm{T}}\mathbf{F}^e - \mathbf{I}\right], \tag{6.4}$$

where the elastic stiffness tensor $\tilde{\mathbf{C}}$ is defined in the intermediate configuration.

A phenomenological power law for the plastic shear rate in each slip system given by

$$\dot{\gamma}^{(\alpha)} = \dot{\gamma}_0 \left| \frac{\tau^{(\alpha)} - a^{(\alpha)}}{\tau_0^{(\alpha)}} \right|^{(m-1)} \left(\frac{\tau^{(\alpha)} - a^{(\alpha)}}{\tau_0^{(\alpha)}} \right) \tag{6.5}$$

is used, where $\tau^{(\alpha)}$ is the resolved shear stress, $a^{(\alpha)}$ is a backstress that describes kinematic hardening, $\dot{\gamma}_0$ is a reference shear rate, $\tau_0^{(\alpha)}$ is a reference shear stress that accounts for isotropic hardening, and m is the material strain rate sensitivity. Shear stress is resolved onto the slip directions with:

$$\tau^{(\alpha)} = \boldsymbol{\sigma} : (\mathbf{s}^{(\alpha)} \otimes \mathbf{n}^{(\alpha)}), \tag{6.6}$$

where $\boldsymbol{\sigma}$, $\mathbf{s}^{(\alpha)}$ and $\mathbf{n}^{(\alpha)}$ are the Cauchy stress, slip direction and slip plane normal respectively, all of which are in the current configuration. The Cauchy stress is given by:

$$\boldsymbol{\sigma} = \frac{1}{J_e}\left[\mathbf{F}^e \cdot \mathbf{S}^e \cdot (\mathbf{F}^e)^{\mathrm{T}}\right], \tag{6.7}$$

where J_e is the determinate of $\mathbf{F}^e$. The relationship between $\mathbf{s}^{(\alpha)}$ and $\tilde{\mathbf{s}}^{(\alpha)}$ is given by

$$\mathbf{s}^{(\alpha)} = \mathbf{F}^e \cdot \tilde{\mathbf{s}}^{(\alpha)}, \tag{6.8}$$

and the relationship between $\mathbf{n}^{(\alpha)}$ and $\tilde{\mathbf{n}}^{(\alpha)}$ is given by

$$\mathbf{n}^{(\alpha)} = \tilde{\mathbf{n}}^{(\alpha)} \cdot (\mathbf{F}^e)^{-1}, \tag{6.9}$$

which ensures that the slip plane normal vector remains orthogonal to the slip direction in the current configuration.

The reference shear stress $\tau_0^{(\alpha)}$ evolves based on the expression:

$$\dot{\tau}_0^{(\alpha)} = H \sum_{\beta=1}^{N_{\text{slip}}} q^{\alpha\beta} \dot{\gamma}^{(\beta)} - R\tau_0^{(\alpha)} \sum_{\beta=1}^{N_{\text{slip}}} |\dot{\gamma}^{(\beta)}|, \tag{6.10}$$

where H is a direct hardening coefficient and R is a dynamic recovery coefficient and $q^{\alpha\beta}$ is the latent hardening ratio given by:

$$q^{\alpha\beta} = \chi + (1 - \chi)\delta_{\alpha\beta} \tag{6.11}$$

where χ is a latent hardening parameter. The backstress $a^{(\alpha)}$ evolves based on the expression:

$$\dot{a}^{(\alpha)} = h\dot{\gamma}^{(\alpha)} - ra|\dot{\gamma}^{(\alpha)}|, \tag{6.12}$$

where h and r are direct and dynamic hardening factors respectively.

A computational crystal plasticity algorithm needs to solve a set of non-linear equations from Eq. (6.1) to Eq. (6.12). Different numerical methods can be used to solve these equations. McGinty and McDowell [**77**] gave an implicit time integration algorithm for the material law with the finite element method. However, the SCA method uses Fast Fourier Transformation method, CP alorithms have been shown to be effective in this framework as well. For example, Lebensohn *et al.* [**61**] reformulated a crystal plasticity law for a Fast Fourier Transformation framework to solve micro-mechanics problems with periodic microstructures. Here, the same crystal plasticity model is implemented in the SCA and FEM calculations under small-strain assumption, where the Green-Lagrange strain is approximated by the Cauchy strain. Extension to finite strain is straightforward, as discussed in Section 2.4.

6.1.3. Examples

In this section, CPSCA is used to predict the overall response of an RVE consisting of equiaxed, randomly oriented grains with the fully developed plastic strain tensor calculated *a priori* as offline database.

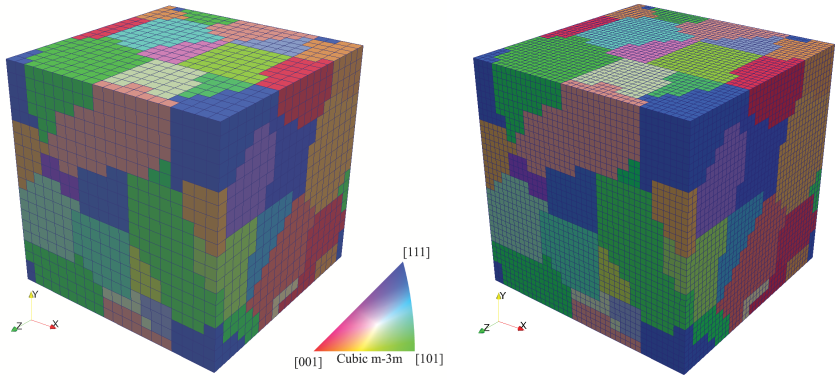

(a) (b)

Figure 6.1. RVE consisting of 35 equiaxed, randomly oriented grains with (a) $20 \times 20 \times 20$ and (b) $40 \times 40 \times 40$ voxel mesh.

A set of crystal plasticity parameters are listed in Table 6.1; the Young's modulus and Possion's ratio of the soft inclusion are 500 MPa and 0.19, respectively. These parameters match reasonably well with an FCC metal.

Table 6.1. Crystal plasticity parameters for a FCC metal.

C_{1111} (MPa)	C_{1122} (MPa)	C_{2323} (MPa)
80869	40356	20257
$\dot{\gamma}_0$ (s^{-1})	m	initial τ_0 (MPa)
0.002	10	320
H (MPa)	R (MPa)	χ
0	0	1
initial a_0 (MPa)	h (MPa)	r (MPa)
0.0	500	0

An example of such an RVE is shown in Figure 6.1. Figure 6.2 shows the comparison of overall stress-strain curves predicted by CPFEM and CPSCA respectively. One can see that the overall response for the coarser cases converge to very similar solutions when

elements or clusters are added. CPSCA results in harder response than the CPFEM solutions when very coarse clustering (e.g. 1 cluster/grain) is used. This is not an exceptional result, because SCA uses a FFT solution based on the Lippmann-Schwinger equation.

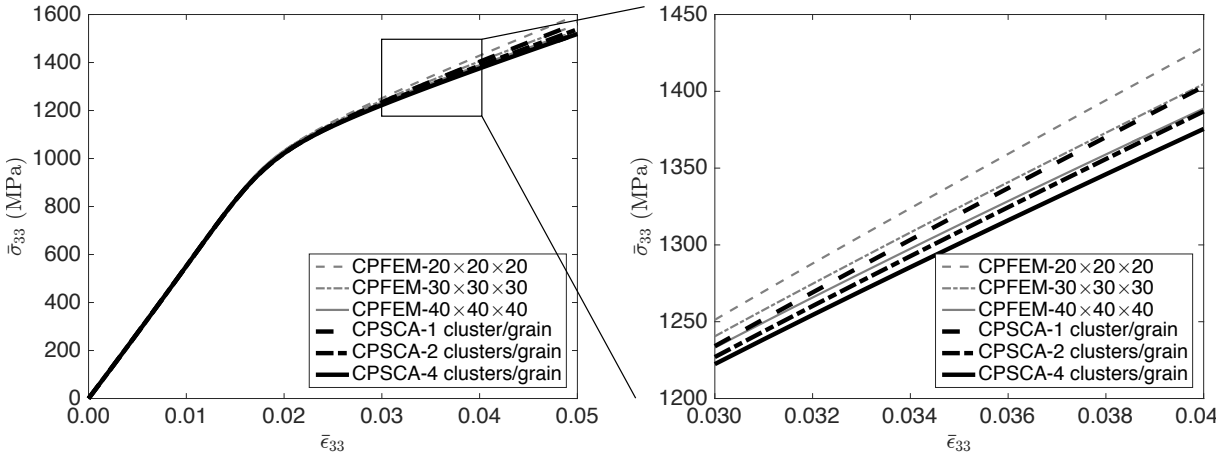

Figure 6.2. $\bar{\sigma}_{33}$ versus $\bar{\epsilon}_{33}$ using CPFEM and CPSCA respectively.

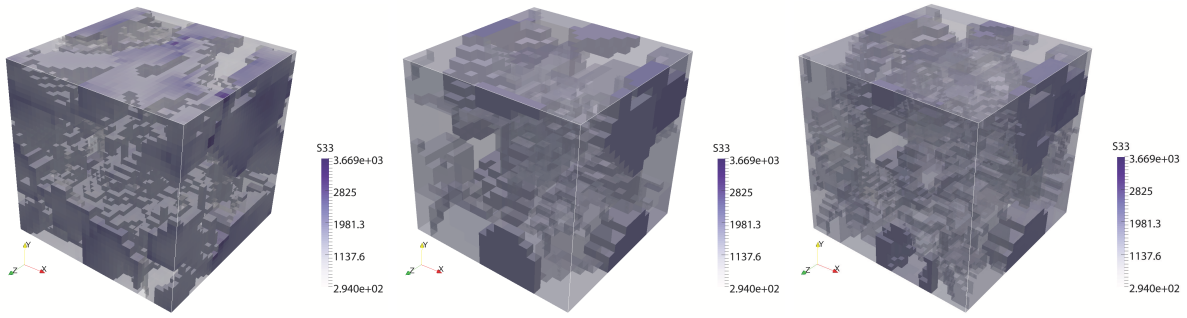

(a) CPFEM: 40^3 voxels (b) CPSCA: 35 clusters (c) CPSCA: 140 clusters

Figure 6.3. Volume plots of S_{33} for three different cases

The full 3D solution state for S_{33} at 5% averaged strain is shown in the opacity and color contour plots shown in Figure 6.3. With this visualization, some differences in the interior can be observed: in the CPSCA method, stress is generally more concentrated, and lower outside of the concentration region, when compared to the CPFEM solutions

with more distributed and generally higher levels of overall stress. In both solution methods and with all mesh sizes and number of clusters, stress concentrates in grains with high Schmid factor. The peak values for the FEM and SCA solutions are generally within 10%, while the minimum values differ by more.

Again, the DNS CPFEM implemented as a user material in Abaqus typically takes 587 seconds, 5177 seconds, and 31446 seconds for the $20\times20\times20$, $30\times30\times30$ and $40\times40\times40$ mesh respectively, on 24 cores. With the same number of loading increments, CPSCA (in FORTRAN) only takes 18 seconds, 96 seconds and 793 seconds using 1 cluster/grain, 2 clusters/grain and 4 clusters/grain respectively on one Intel i7-3632 processor.

6.2. Nonlinear polymer matrix composite with damage

6.2.1. Background

Predictive material modeling is especially challenging for composite materials due to their hierarchical structure that spans multiple length scales and necessitates the use of multi-scale analysis in simulation. Figure 6.4 demonstrates an example of polymer matrix composite (PMC) with three different scales: part (macroscale), woven composite (mesoscale) and unidirectional fiber composite (microscale). The goal is to find a macroscopic constitutive law with minimum experimental input via a bottom-up hierarchical multi-scale approach. Because for most composites the general form of the constitutive law of the microstructures assigned to the integration (aka Gauss or material) points is unknown, it is necessary to rely on direct numerical simulation (DNS) techniques (aka FE^2 [**34**]) in multiscale FEA to determine the material response at those points. While DNS is quite flexible and accurate, it is very expensive; rendering DNS-based multiscale design of materials insurmountable.

Our framework for the modeling of hierarchical composite materials is closely related to the so-called high-throughput computational materials science wherein a rich database can be generated to build structure-property maps. The basic idea of database development for material design of composite is shown in Figure 6.4. Random sampling is firstly performed in a top-down fashion. In the macro to meso sampling step, a woven lamina

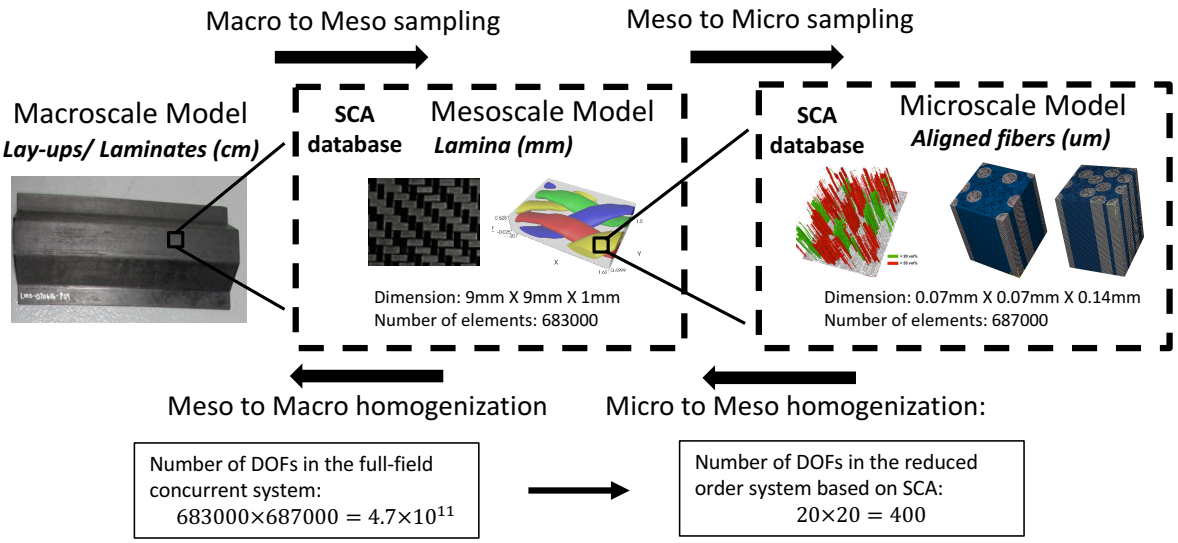

Figure 6.4. Three-scale multiscale modeling framework for PMC material based on SCA.

structure will be assigned to each integration point in the macroscale FE model. The woven lamina structure can have different statistical descriptors, such as woven angles, yarn sizes and spacing distances, which are defined as the random variables and used to construct the database. Similarly, in the meso-to-micro sampling step, one can assign UD models with different random variables such as fiber volume fractions. Since there are three scales, two homogenization steps need to be considered: the micro-to-meso and meso-to-macro homogenization. In the homogenization step, the incremental strain at each material point in the upper-scale model is input into a lower-scale RVE model, and the corresponding stress of the material point is obtained through averaging in the RVE. For each set of the random variables or structural descriptors, an RVE is constructed and an entry in the SCA database is created, where the number of clusters and interaction tensors between clusters are stored. With this multiscale database, the structure-to-property map can be built efficiently and accurately for complex material behaviors, such as plasticity and damage.

The current work will only focus on the two-scale multiscale modeling of the unidirectional (UD) fiber composite with both plasticity and damage. The SCA reduced order model will be validated experimentally at the composite level by comparing its homogenized RVE properties with experimental data. With the calibrated damage law, the concurrent simulation is able to predict the fracture patterns at the coupon level, which will be also be validated against experiments. All the experimental data is provided by Dr. Joel Fenner from Northwestern University.

6.2.2. Experimental UD characterization

For the UD composite, Dr. Joel Fenner from Northwestern University has conducted 0°, 10° and 90° off-axis tensile tests. The geometries for each of the three tensile test coupons are shown in Figure 6.5. The thickness of all the coupons are 2.3 mm, which corresponds to 12 layers of prepreg layers. During each test, the two ends of the coupon can only move in the loading directions.

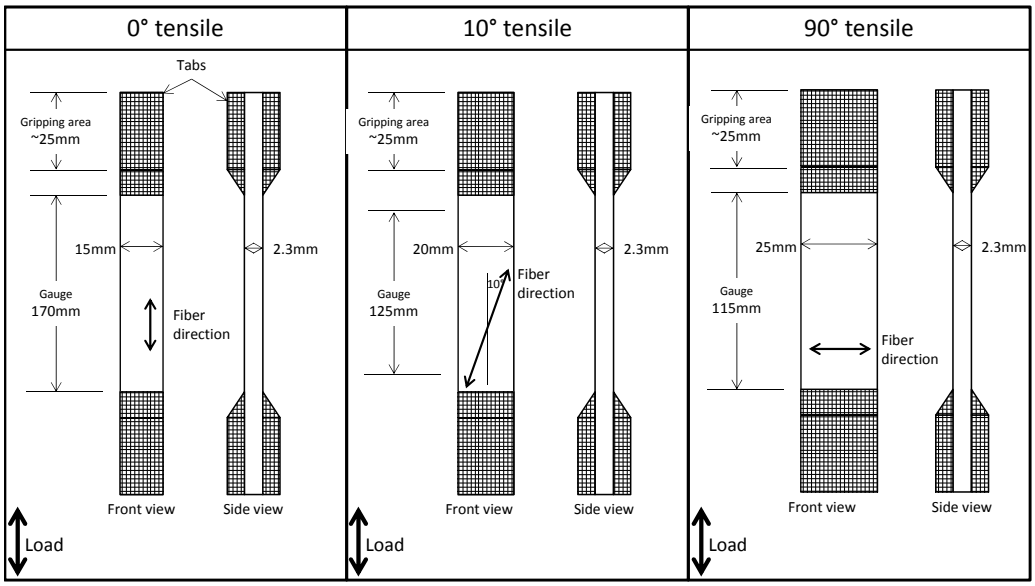

Figure 6.5. UD tensile coupon geometries with different fiber directions.

The 0° and the 90° tensile coupons are used to measure the UD behavior under longitudinal tension and transverse tension, respectively. A strain gauge is placed at the

center of the coupon to measure the strain, and the engineering stress is obtained by

$$\sigma_{11} = \frac{F}{A_0} \quad \text{or} \quad \sigma_{22} = \frac{F}{A_0} \tag{6.13}$$

where F is the total force applied on the coupon, and A_0 is the initial coupon cross-section area. Due to the symmetry, the stress is distributed uniformly inside the 0° and 90° coupons before the failure, so that coupon test data can be directly compared with the RVE homogenization results. The 10° tensile coupon is intended to measure the UD properties under longitudinal shear. The shear stress is calculated as

$$\sigma_{12} = \frac{F}{A_0} \sin(10^\circ) \cos(10^\circ). \tag{6.14}$$

As will be shown later in Section 6.2.4, the stress distribution is actually non-uniform inside the 10° coupon, especially when the material undergoes plasticity or damage. Therefore, the stress derived from the total force in Eq. (6.14) will be different from the one obtained from the RVE homogenization.

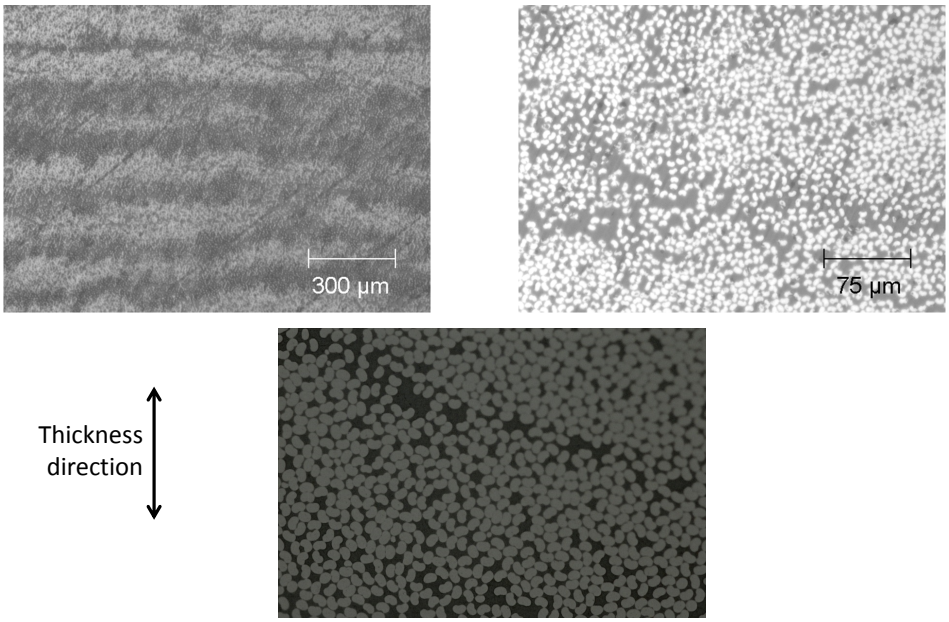

Figure 6.6. UD microstructure images along the thickness direction at various length scales.

Figure 6.6 presents the microstructure images of the UD coupon along the thickness direction. From the images, it can be clearly seen that the cross-section of the individual fibers is bean-shaped instead of circular. This irregular shape may introduce more strain concentration into the system, and have an influence on mechanical properties, such as failure strength. In the current study, however, each individual fiber is still considered to have a circular cross-section. Nevertheless, it should be sufficient to capture the elastic and plastic behaviors, as well as essential failure mechanisms of the UD composite.

6.2.3. Results for UD RVE homogenization

For the UD composite, elastic constants of the pure epoxy and the carbon fiber are obtained from experiment. Before damage, the carbon fiber is assumed to be orthotropic elastic, and the epoxy is assumed to be an isotropic elasto-plastic material with von Mises (J2) plasticity. Although it has been observed in experiment that the epoxy has different plastic behaviors under tension and compression [**82, 121**], von Mises plasticity should be sufficient for the current investigation as only tension and shear loadings are considered. The hardening curve of the epoxy is measured from tensile test with the effective plastic strain ε_p up to 0.005, after which it is first assumed to be almost perfectly plastic (see Figure 6.9).

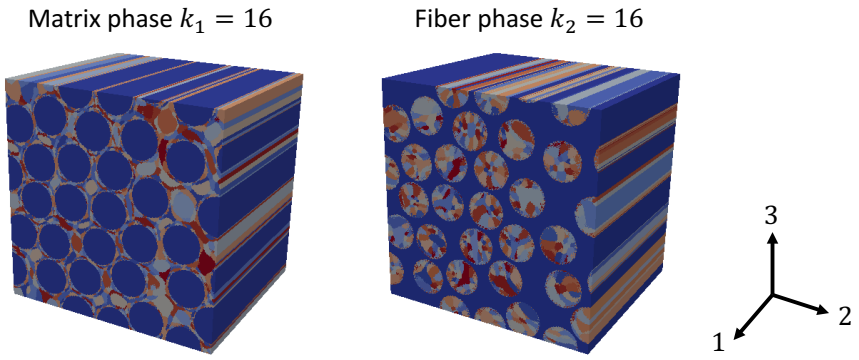

Figure 6.7. UD RVE geometry and SCA clustering results with 16 clusters in the matrix and fiber phases.

The UD RVE model is generated by randomly placing non-overlapping fibers into the matrix. The volume fraction of the carbon fiber is measured to be around 51%. The mesh size of the DNS model is $10 \times 300 \times 300$. Due to symmetry, the results from first-order homogenization should be independent of the RVE length in the fiber direction. In the SCA offline stage, the strain concentration tensor is used for the clustering analysis. Figure 6.7 shows the clustering results with 16 clusters in both the matrix and fiber phases. In the SCA online stage, the reference material is approximated as the effective stiffness tensor $\bar{\mathbf{C}}^*$ in the matrix phase (see Eq. (4.20)).

As we can see from Figure 6.8, the SCA predictions converge to the DNS results under all the loading conditions. By using 16 clusters in both phases, its accuracy with respect to DNS is within 10%, which is satisfactory for the current application. In terms of the computational cost, the SCA model with 16 clusters take 0.08s for each loading increment on one Intel i7-3632 processor, while a DNS with a 300x300x10 mesh typically takes 1 hour on 24 cores (in a state-of-the art high performance computing cluster with the following compute nodes: Intel Haswell E5-2680v3 2.5GHz 12-cores). However, the predicted stress-strain curves (from both SCA and DNS) under longitudinal shear does not match the experimental data very well. This is because the hardening curve of the epoxy has been assumed to be almost perfectly plastic outside the available experimental data (see Figure 6.9), which underestimates the yield stress for larger effective plastic strain ($\varepsilon_p > 0.005$). To better approximate the hardening curve, an exponential form is proposed,

$$\sigma_Y = -a_2 \exp(-a_1 \varepsilon_p) + a_3 \quad \text{(MPa)} \tag{6.15}$$

After the calibration, the parameters are determined to be

$$a_1 = 140, \quad a_2 = 90 \text{ MPa}, \quad a_3 = 120 \text{ MPa} \tag{6.16}$$

Note that the exponential hardening law performs close to perfect plasticity for large ε^p, so that shear band/localization will form within the 10° off-axis tensile coupon.

Another interesting feature about the UD composite is that its failure behavior is totally different under tension and shear. It is brittle under longitudinal and transverse

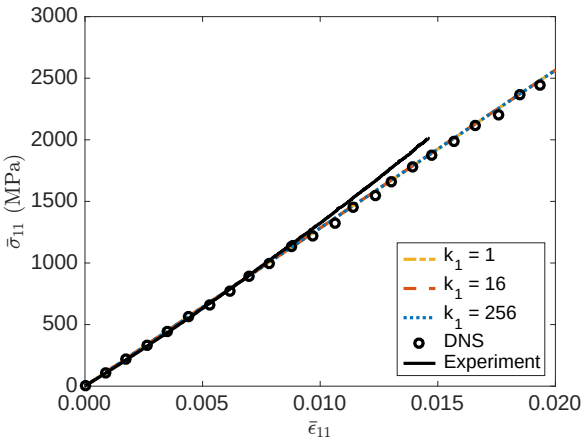

(a) Longitudinal tension

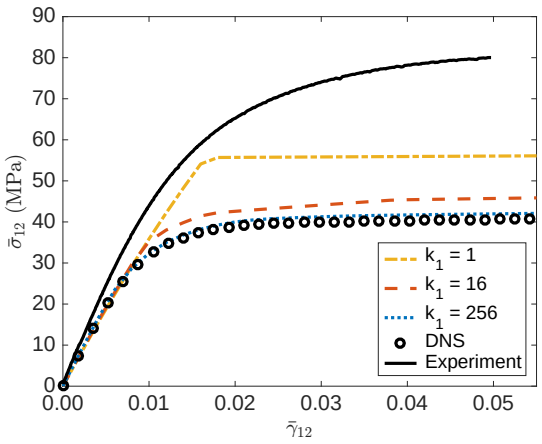

(b) Longitudinal shear

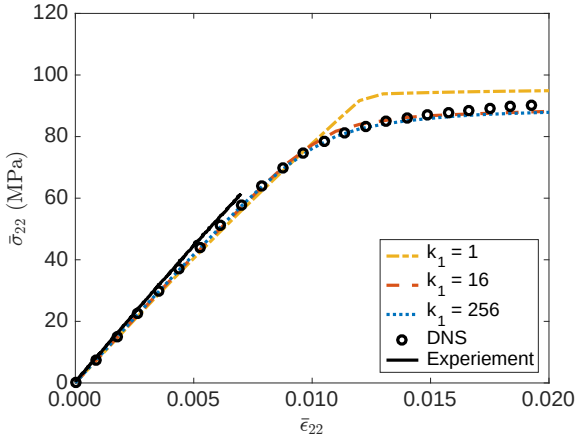

(c) Transverse tension

Figure 6.8. Stress-strain curves given by the SCA model. The hardening curves are assumed to be perfectly plastic after the available experimental data. Damage is not considered.

tension, while a large plastic deformation can be achieved before failure under longitudinal shear. This is generally hard to be captured by a macroscopic empirical constitutive law. However, under the multiscale modeling framework, it becomes much more natural since different mechanisms can be considered separately in each individual phase. First, the failure under longitudinal tension is due to the fiber breakage. The fiber phase is assumed to be fully damaged if its normal stress in the fiber direction reaches a critical stress

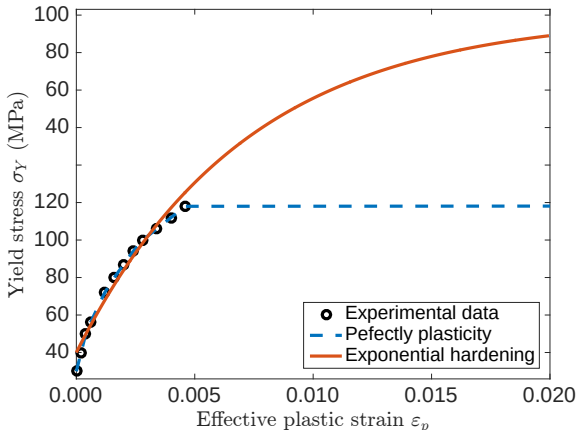

Figure 6.9. Hardening curves of the epoxy in the UD composite.

X^{fiber},

$$d_m^{fiber} = 1 \quad \text{if } \{\sigma_m^{fiber}\}_{11} > X^{fiber}, \tag{6.17}$$

where d_m^f is the microscopic damage parameter in the fiber phase. Under transverse tension, the material damage is dominated by the debonding on the fiber-epoxy interface and void growth in the epoxy. Here, a maximum hydrostatic stress law is adopted for the epoxy phase,

$$d_m^{epoxy} = 1 \quad \text{if } p_m^{epoxy} > X^{epoxy}, \tag{6.18}$$

where p denotes the pressure stress,

$$p = -\frac{1}{3}(\sigma_{11} + \sigma_{22} + \sigma_{33}) \tag{6.19}$$

In the three-step algorithm introduced in Section 5.2, the microscopic stress in the first step is used to evaluate this damage law. On the other hand, the UD composite behaves like a ductile material under longitudinal shear. In addition to the critical failure defined in Eq.(6.18), the damage parameter can also evolve with the effective plastic strain,

$$d_m^{epoxy}(\varepsilon_p) = \begin{cases} 0 & \text{if } \varepsilon_p \le \varepsilon^{\text{cr}} \\ 1 - \dfrac{\varepsilon^{\text{cr}}}{\varepsilon_p} \exp(-\alpha(\varepsilon_p - \varepsilon^{\text{cr}})) & \text{if } \varepsilon_p > \varepsilon^{\text{cr}} \end{cases} \tag{6.20}$$

Finally, all material parameters of the carbon fiber and epoxy are listed in Table 6.2. It should be noted that all the damage parameters (X^{fiber},ε_{cr}, α and X^{epoxy}) are calibrated for the SCA RVE model with $k_1 = 16$.

Table 6.2. Material parameters for the UD composite.

Carbon fiber				
E_1 (GPa)	E_2 (GPa)	E_3 (GPa)	G_{12} (GPa)	G_{13} (GPa)
245.0	19.8	19.8	29.2	29.2
G_{23} (GPa)	ν_{12}	ν_{13}	ν_{23}	X^{fiber} (MPa)
5.9	0.28	0.28	0.67	3675
Epoxy				
E_m (GPa)	ν_m	a_1	a_2 (MPa)	a_3 (MPa)
3.8	0.387	140	90	120
ε_{cr}	α	X^{epoxy} (MPa)		
0.2	100	38		

As we can see from Figure 6.10, the predicted properties of the UD composite agree with the experimental data very well in both the elastic and plastic regime. The same parameters will be used in the concurrent framework to predict the failure behavior at the part level.

6.2.4. Results for concurrent modeling of UD coupons

For the concurrent simulation, the average mechanical response of the UD RVE is transferred back to the coupon-scale model, which avoids using a empirical constitutive law for the UD composite. At each integration point in the coupon scale model, a microscale UD RVE is associated and analyzed on the fly during the simulation, which can be very time consuming if DNS is used [**34**]. To expedite the RVE analysis, the SCA method is proposed to compress the number of degrees of freedom. It has been implemented as a user-defined material (VUMAT) inside a commercial FEA software (ABAQUS).

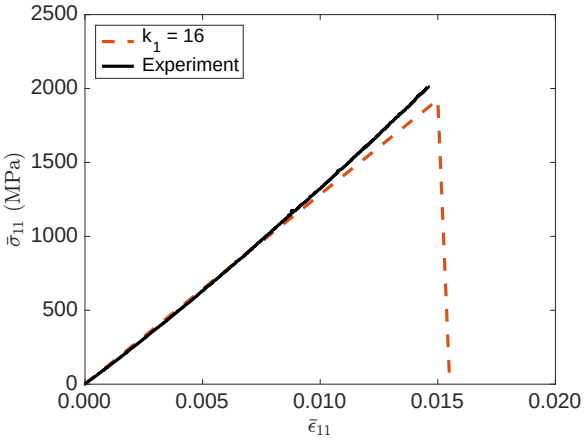

(a) Longitudinal tension

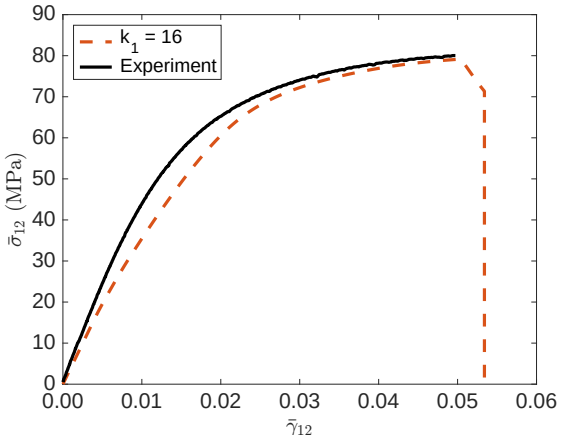

(b) Longitudinal shear

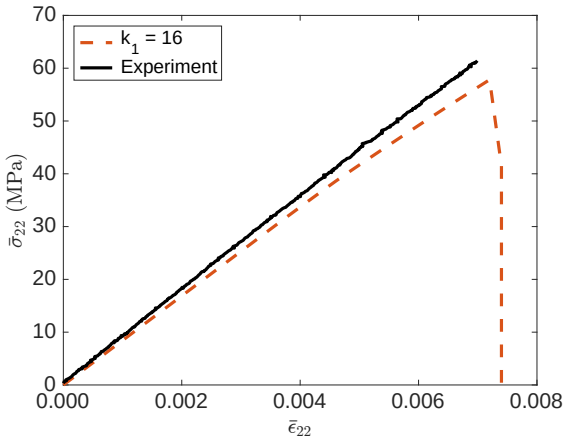

(c) Transverse tension

Figure 6.10. Stress-strain curves given by the SCA model with the exponential hardening law and calibrated damage law.

The coupon for the 10° off-axis tension test is modeled with a reduced integration hex element. The geometry is given in Figure 6.5 , and the FE mesh size is $100 \times 16 \times 2$ as shown in Figure 6.12(a). The nonlocal damage formulation (see Section 5.6) is used to avoid pathological mesh dependency, and the length parameter l_0 is chosen as 4 mm. The microscale SCA database has in total 32 clusters (16 in matrix phase and 16 in fiber phase). All the material parameters are provided in Table 6.2. From the simulation, the reaction forces at all nodes on each end are gathered and integrated on the surface to

determine the total reaction force. The shear strain is averaged at a middle region of the coupon, similar to how the strain is measured using strain gauge in experiments.

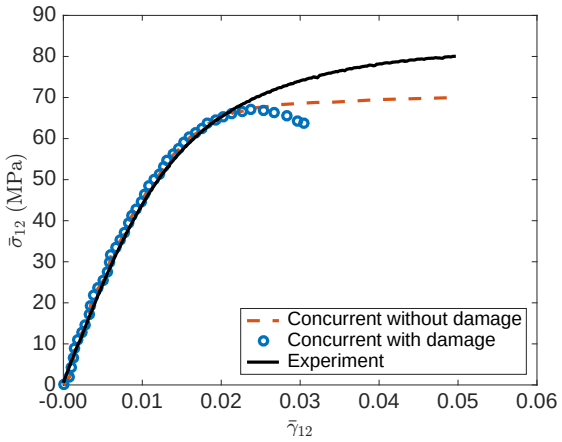

Figure 6.11. Stress-strain curves of the 10° off-axis tensile coupon from concurrent simulations and experiment.

The predicted stress-strain curves are presented in Figure 6.11. In the concurrent simulation without damage, the predicted curve agrees very well with the experimental data when the longitudinal shear strain $\bar{\gamma}_{12}$ is less than 0.02. After that, shear bands with high strain concentration started to propagate from the two ends, and results in a plateau in the stress-strain curve, which is less than the experimental value. Due to the strain localization, damage will also initiate in the shear band, and the coupon in the concurrent simulation with damage fails around $\bar{\gamma}_{12} = 0.03$. It can be concluded that the RVE homogenization is not comparable to the 10° off-axis coupon test for relatively large strain, since it can not capture the localization effect in the coupon test. On the other hand, concurrent simulations for the 0° and the 90° tensile coupons have also been performed. Due to the homogeneous strain distribution within the coupon in either case, the predicted responses from the concurrent simulation were same as the those from the RVE homogenization. Further calibration for the shear properties in the UD composite will be performed.

Figure 6.12(b) shows the crack pattern in the 10° off-axis coupon predicted by the concurrent simulation with SCA database. In the experiment, the crack patterns in 6

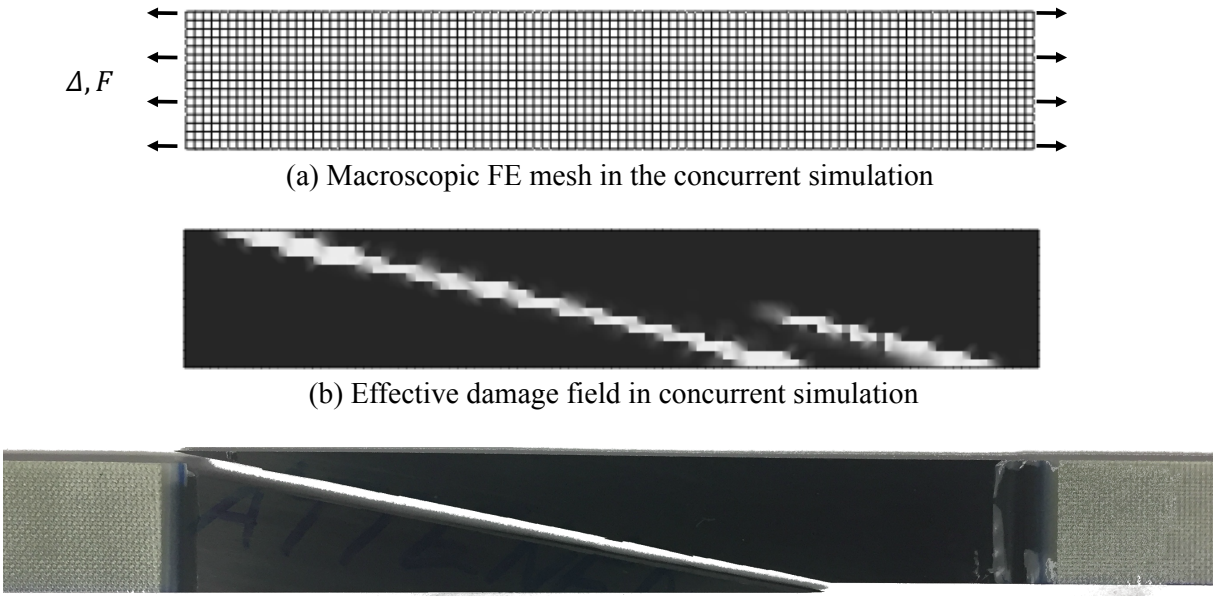

(a) Macroscopic FE mesh in the concurrent simulation

(b) Effective damage field in concurrent simulation

(c) Experimental image of damaged coupon

Figure 6.12. Comparisons between concurrent simulations and experiment.

samples were consistently same as one shown in Figure 6.12(c). The angle between the crack and the loading direction was always around 10° for each sample which makes sense because the break goes along the direction of the fibers. Since no defect has been introduced, there are two damage initiation sites due to symmetry in the concurrent simulation. In the end, a single crack dominated the damage process and propagated through the specimen. It can be observed that the predicted crack pattern agrees with the experiment very well, showing the capability of the multiscale concurrent framework based on the SCA method.

CHAPTER 7

Conclusions and Future Work

7.1. Achievements

This dissertation presents a comprehensive suite of analytical and data-driven reduced-order homogenization methods with applications to various heterogeneous material systems, including viscoelastic polymer nanocomposite, generic elasto-plastic material with and without damage, polycrystal material with crystal plasticity and unidirectional fiber composite. The contributions of this dissertation are concluded hereafter.

The Lippmann-Schwinger integral equation has been derived based on the concept of the reference material and its Green's function in Chapter 2. The equilibrium condition was transformed from a partial differential equation into the integral equation, and the resulting formulation is general and independent of the constitutive law of the real material. It was first formulated under small-strain assumption, and further extended to consider finite-strain problems. The Lippmann-Schwinger equation is the basis for both the analytical and data-driven reduced-order homogenization method in this dissertation.

In Chapter 3, a new mathematical framework of overlapping geometries that allows for the study of dilute particles, clustered particles or interacting particles was proposed. Weighted-mean and additive overlapping conditions were introduced to consider various physical phenomena in the overlapping regions. The corresponding Lippmann-Schwinger integral equations were derived. The method was capable of capturing the effect of various distributions of inclusions, while the Mori-Tanaka and self-consistent methods depend only on volume fraction of the overall inclusion phase. Finally, the proposed method was applied to a viscoelastic polymer nanocomposite with an interphase region. The inversely predicted interphase properties, including interphase thickness and complex modulus,were further validated by experimental data.

To consider nonlinear history-dependent material behaviors and more complex microstructural morphologies, a data-driven reduced-order homogenization method called self-consistent clustering analysis (SCA) was introduced in Chapter 4. A good trade-off between efficiency and accuracy is possible with SCA through the domain decomposition based on k-means clustering of high-fidelity data in the offline stage and the micromechanics-based self-consistent schemes in the online stage. With numerical examples on 2D and 3D nonlinear elasto-plastic material, the SCA method was shown to have several attractive features: accurate, good convergence under refinement, computationally efficiency, and involving a minimum amount of effort for both the offline and online stages. Moreover, another major contribution of this dissertation is the construction of a consistent multiscale framework for softening material. In Chapter 5, a three-step homogenization scheme was proposed and formulated based on the complementary free energy. By matching the effective elastic strains of the undamaged and damaged RVE, strain localization is avoided in the microscale RVE, and the homogenized behavior in the strain-softening regime is independent of the RVE size. Enabled by the SCA method, as well as the energy regularization and nonlocal formulation, several concurrent multiscale simulations have been performed to show the capability of proposed framework. Finally, the applications to two complex nonlinear material systems, polycrystalline and polymer matrix composite, have been demonstrated in the Chapter 6.

7.2. Suggestions for future work

There are many promising research directions based on the work in this dissertation, in terms of both theory development and application. Suggestions are given for different future directions.

7.2.1. Analytical micromechanics method and interphase inverse modeling

The analytical micromechanics method for overlapping geometry and inverse modeling framework can be applied to a broad range of nanocomposite [**118, 66, 103**]. The methods of Pedro Ponte Castaeda (nonlinear bounds [**17**]; second- order estimation of

nonlinear phase potential [**18**]), and George J. Dvorak (transformation field analysis [**28**]) seem to be the most promising areas for extension of this work to non-linear regimes. In the transformation field analysis (TFA), all the internal variables (e.g. plastic strain and elastic strain) are assumed to be uniform in each material phase. To improve the accuracy for nonlinear materials, several corrections based on mean-field theories have also been proposed in the literature [**19, 100**].

In terms of the inverse modeling of interphase properties for viscoelastic polymer nanocomposite, the thickness of the interphase is currently found by trial-and-error, and this will be improved by incorporating the thickness into the optimization problem with a more rigorous mathematical definition. The main challenge here is that an optimum interphase moduli may not exist if the interphase is not thick enough, which would cause instability in the optimization algorithm. On the other hand, it is also possible to assume that the interphase thickness varies with the frequency, which may provide us with more physical insight into the polymer nanocomposite.

In the current homogenization scheme, the Boolean-Poisson model is assumed for the distribution of the inclusions. In future work, more realistic microstructural information can be obtained from experimental characterization. 3D microstructure directly from experiments is possible but still burdensome even with the state-of-the-art imaging techniques, especially for soft materials like polymer nanocomposite [**125, 123**]. Thus, a myriad of reconstruction techniques which computationally generate 3D microstructures based on 2D images [**110, 108, 50, 59, 123**] can be used to reduce the complexity and cost in the experimental stage. The statistical information (e.g. particle distribution) characterized from the experimental images can then be incorporated into the analytical model to provide more realistic predictions.

7.2.2. Self-consistent clustering analysis

While the data-driven SCA homogenized shows good accuracy for various material systems, the convergence of the self-consistent scheme, as well as the influence of the clustering data, need to be more rigorously investigated, which will pose some new fundamental

mathematical questions. For macroscopic anisotropic material, it will be helpful to define a anisotropic reference material in the Lippmann-Schwinger equation, which needs the Green's function to be reformulated. For a large number of clusters, the computational time of SCA with a direct solver (e.g. LU decomposition) will increase as the cube of number of clusters, which hinders the application of SCA to irregular complex microstructure, such as polycrystalline materials. Possible solutions include the adoption of advanced Krylov space solver and parallelization of the code.

In the online stage of SCA, self-consistent schemes have been proposed to improve the accuracy. However, the mechanism behind the self-consistent schemes require better understanding through rigorous mathematical investigations. On the other hand, the fixpoint iteration method for solving the self-consistent equation may encounter convergence problems, and this is currently solved by decreasing the step size of the iteration. In the future, other root-finding algorithms can be adopted to improve the convergence.

Moreover, extending SCA to finite-strain problem will also be important for materials under large deformation, such as finite-strain crystal plasticity [**29**] and hyperelasticity [**24, 54**]. There are mainly two challenges of finite-strain SCA. First, the original cluster data based on the elastic strain concentration tensor may not be sufficient for large deformation during the online stage, and this requires more information (e.g. plastic strain) input to the offline-stage. Second, for finite-strain problems with more localized deformation, as well as the small-strain material damage considered in Chapter 5, the clustering algorithm in the offline-stage needs to better designed, such as controlling the spacial distribution of each cluster or using non-uniform distance definition.

Since SCA maintains certain local deformation and stress information, it is possible to apply this method for fatigue performance evaluation. For example, the distribution of grains and precipitates determines the intrinsic fatigue resistance of precipitation hardening alloys. Statistical volume elements (SVEs) including different configuration of grains and precipitates can be sampled based on experimental observation and used to evaluate the fatigue resistance. SCA, with its efficiency, can speed up this process and is particularly suitable for statistical analysis of fatigue limit.

7.2.3. Multiscale concurrent simulation with strain softening

In the current mutliscale simulation with damage, each macroscale material point shares the same microscale RVE. However, a realistic structure-scale damage assessment through the concurrent simulation should be stochastic, and different material points in the macroscale may be associated with different microscale RVEs based on the statistics. Here, microstructural characterization and reconstruction play a key role in the database construction. The new approach will be developed to account for location dependence, microstructure heterogeneity dependence, and spatial variation of defects due to manufacturing processes, and to assess probabilistic damage performance at the macroscale. Since the initiation and evolution of material damage strongly depend on the microstructure and the loading path at each material point, it is necessary to consider the damage behavior of any possible representative microstructure under various loading paths. Various characterization and reconstruction techniques, such as correlation functions [**69, 43**], descriptor-based methods [**123**], Gaussian random process [**51**] and supervised learning-based approach [**15**], can be utilized to classify the experimental images (including abnormal detection) and to further generate the corresponding microstructural RVEs in both 2D and 3D. SCA databases will be constructed for these RVEs and assigned to the macroscale structure through a random sampling process, where spacial microstructural correlations can also be incorporated.

For large-scale concurrent simulations, it is important to improve efficiency of the SCA program (user-defined material). For example, the direct solver (LU decomposition) is currently used for the matrix inversion part. When the number of clusters increases, it will be helpful to use iterative solvers, such as generalized minimal residual method (GMRES) [**106**]. On the other hand, the SCA program needs to be optimized to decrease the memory occupation at each integration point for large-scale computation.

In terms of the energy regularization in Chapter 6, no mathematical relation between the damage parameters and length parameter has been established yet. In the future, it is promising to build an integrated framework for material damage based on the variational principle, similar to those in phase-field models for fracture [**89, 14, 13**]. I am optimistic

that the data-driven SCA method may be applied to study more intriguing material systems, like hierarchical structures created by advanced manufacturing techniques [**84**].

References

[1] Aboudi, J. A continuum theory for fiber-reinforced elastic-viscoplastic composites. *International Journal of Engineering Science 20*, 5 (1982), 605–621.

[2] Bai, X., Bessa, M., Melro, A., Camanho, P., Guo, L., and Liu, W. High-fidelity micro-scale modeling of the thermo-visco-plastic behavior of carbon fiber polymer matrix composites. *Composite Structures* (2015), –.

[3] Balazs, A. C., Emrick, T., and Russell, T. P. Nanoparticle polymer composites: where two small worlds meet. *Science 314*, 5802 (2006), 1107–1110.

[4] Barghout, L., and Sheynin, J. Real-world scene perception and perceptual organization: Lessons from computer vision. *Journal of Vision 13*, 9 (2013), 709–709.

[5] Bazant, Z. P. Can multiscale-multiphysics methods predict softening damage and structural failure? *International Journal for Multiscale Computational Engineering 8*, 1 (2010).

[6] Bazant, Z. P., and Jirásek, M. Nonlocal integral formulations of plasticity and damage: survey of progress. *Journal of Engineering Mechanics 128*, 11 (2002), 1119–1149.

[7] Bažant, Z. P., and Oh, B. H. Crack band theory for fracture of concrete. *Matériaux et construction 16*, 3 (1983), 155–177.

[8] Beese, A. M., An, Z., Sarkar, S., Nathamgari, S. S. P., Espinosa, H. D., and Nguyen, S. T. Defect-tolerant nanocomposites through bio-inspired stiffness modulation. *Advanced Functional Materials 24*, 19 (2014), 2883–2891.

[9] Belytschko, T., Liu, W. K., Moran, B., and Elkhodary, K. *Nonlinear finite elements for continua and structures*. John wiley & sons, 2013.

[10] Benveniste, Y. A new approach to the application of mori-tanaka's theory in composite materials. *Mechanics of materials 6*, 2 (1987), 147–157.

[11] Berkooz, G., Holmes, P., and Lumley, J. L. The proper orthogonal decomposition in the analysis of turbulent flows. *Annual review of fluid mechanics 25*, 1 (1993), 539–575.

[12] Bessa, M., Bostanabad, R., Liu, L., Hu, A., Apley, D., Brinson, C., Chen, W., and Liu, W. A framework for data-driven analysis of materials under uncertainty: Countering the curse of dimensionality. *Computer Methods in Applied Mechanics and Engineering 320* (2017), 633–667.

[13] Borden, M. J., Hughes, T. J. R., Landis, C. M., Anvari, A., and Lee, I. J. A phase-field formulation for fracture in ductile materials: Finite deformation balance law derivation, plastic degradation, and stress triaxiality effects. *Computer Methods in Applied Mechanics and Engineering 312* (2016), 130–166.

[14] Borden, M. J., Verhoosel, C. V., Scott, M. A., Hughes, T. J. R., and Landis, C. M. A phase-field description of dynamic brittle fracture. *Computer Methods in Applied Mechanics and Engineering 217-220*, May (2012), 77–95.

[15] Bostanabad, R., Chen, W., and Apley, D. Characterization and reconstruction of 3d stochastic microstructures via supervised learning. *Journal of microscopy 264*, 3 (2016), 282–297.

[16] Camanho, P., Bessa, M., Catalanotti, G., Vogler, M., and Rolfes, R. Modeling the inelastic deformation and fracture of polymer composites – part ii: Smeared crack model. *Mechanics of Materials 59*, 0 (2013), 36 – 49.

[17] Castañeda, P. P. The effective mechanical properties of nonlinear isotropic composites. *Journal of the Mechanics and Physics of Solids 39*, 1 (1991), 45–71.

[18] Castañeda, P. P. Second-order homogenization estimates for nonlinear composites incorporating field fluctuations: Itheory. *Journal of the Mechanics and Physics of Solids 50*, 4 (2002), 737–757.

[19] Chaboche, J., Kanouté, P., and Roos, A. On the capabilities of mean-field approaches for the description of plasticity in metal matrix composites. *International Journal of Plasticity 21*, 7 (2005), 1409 – 1434.

[20] Chaboche, J. L. Continuum Damage Mechanics: Part II – Damage Growth, Crack Initiation, and Crack Growth. *Journal of Mechanics 55*, March 1988 (1988), 65—-72.

[21] Cheng, X., Putz, K. W., Wood, C. D., and Brinson, L. C. Characterization of local elastic modulus in confined polymer films via afm indentation. *Macromolecular rapid communications 36* (2014), 391–397.

[22] Chiu, S. N., Stoyan, D., Kendall, W. S., and Mecke, J. *Stochastic geometry and its applications*. John Wiley & Sons, 2013.

[23] Christensen, R., and Lo, K. Solutions for effective shear properties in three phase sphere and cylinder models. *Journal of the Mechanics and Physics of Solids 27*, 4 (1979), 315–330.

[24] de Geus, T. W. J., Vondejc, J., Zeman, J., Peerlings, R. H. J., and Geers, M. G. D. Finite strain FFT-based non-linear solvers made simple. *Submitted 318* (2016), 1–16.

[25] de Souza Neto, E., Peric, D., and Owen, D. *Computational methods for plasticity: theory and applications*. Wiley, 2008.

[26] Diani, J., and Gilormini, P. Using a pattern-based homogenization scheme for modeling the linear viscoelasticity of nano-reinforced polymers with an interphase. *Journal of the Mechanics and Physics of Solids 63* (2014), 51–61.

[27] Diani, J., Gilormini, P., Merckel, Y., and Vion-Loisel, F. Micromechanical modeling of the linear viscoelasticity of carbon-black filled styrene butadiene rubbers: The role of the filler–rubber interphase. *Mechanics of Materials 59* (2013), 65–72.

[28] Dvorak, G. J. Transformation field analysis of inelastic composite materials. *Proceedings of the Royal Society of London A: Mathematical, Physical and Engineering Sciences 437*, 1900 (1992), 311–327.

[29] Eisenlohr, P., Diehl, M., Lebensohn, R. A., and Roters, F. A spectral method solution to crystal elasto-viscoplasticity at finite strains. *International Journal of Plasticity 46*, October (2013), 37–53.

[30] Ellison, C. J., and Torkelson, J. M. The distribution of glass-transition temperatures in nanoscopically confined glass formers. *Nature Materials 2*, 10 (2003), 695–700.

[31] Eringen, A. C. Mechanics of micromorphic continua. In *Mechanics of generalized continua*. Springer, 1968, pp. 18–35.

[32] Eshelby, J. D. The determination of the elastic field of an ellipsoidal inclusion, and related problems. 376–396.

[33] Ester, M., Kriegel, H.-P., Sander, J., and Xu, X. A density-based algorithm for discovering clusters in large spatial databases with noise. 226–231.

[34] Feyel, F. A multilevel finite element method (fe2) to describe the response of highly non-linear structures using generalized continua. *Computer Methods in Applied Mechanics and Engineering 192*, 28–30 (2003), 3233 – 3244. ¡ce:title¿Multiscale Computational Mechanics for Materials and Structures¡/ce:title¿.

[35] Feyel, F., and Chaboche, J.-L. Fe 2 multiscale approach for modelling the elastoviscoplastic behaviour of long fibre sic/ti composite materials. *Computer methods in applied mechanics and engineering 183*, 3 (2000), 309–330.

[36] Fish, J. *Practical multiscaling*. John Wiley & Sons, 2013.

[37] Forest, S. Micromorphic approach for gradient elasticity, viscoplasticity, and damage. *Journal of Engineering Mechanics 135*, 3 (2009), 117–131.

[38] Forgy, E. W. Cluster analysis of multivariate data: efficiency versus interpretability of classifications. *Biometrics 21* (1965), 768–769.

[39] Fritzen, F., and Leuschner, M. Reduced basis hybrid computational homogenization based on a mixed incremental formulation. *Computer Methods in Applied Mechanics and Engineering 260* (2013), 143–154.

[40] Geers, M., Kouznetsova, V., and Brekelmans, W. Multi-scale computational homogenization: Trends and challenges. *Journal of Computational and Applied Mathematics 234*, 7 (2010), 2175 – 2182. Fourth International Conference on Advanced {COmputational} Methods in {ENgineering} (ACOMEN 2008).

[41] Geers, M. G., Kouznetsova, V. G., and Brekelmans, W. Multi-scale computational homogenization: Trends and challenges. *Journal of computational and applied mathematics 234*, 7 (2010), 2175–2182.

[42] Ghosh, S., Lee, K., and Moorthy, S. Two scale analysis of heterogeneous elastic-plastic materials with asymptotic homogenization and voronoi cell finite element model. *Computer Methods in Applied Mechanics and Engineering 132*, 1–2 (1996), 63 – 116.

[43] Greene, M. S., Liu, Y., Chen, W., and Liu, W. K. Computational uncertainty analysis in multiresolution materials via stochastic constitutive theory. *Computer Methods in Applied Mechanics and Engineering 200*, 1 (2011), 309–325.

[44] Gurson, A. L. Continuum theory of ductile rupture by void nucleation and growth: Part i—yield criteria and flow rules for porous ductile media. *Journal of engineering materials and technology 99*, 1 (1977), 2–15.

[45] Hashin, Z., and Shtrikman, S. A variational approach to the theory of the elastic behaviour of polycrystals. *Journal of the Mechanics and Physics of Solids 10*, 4 (1962), 343–352.

[46] Hashin, Z., and Shtrikman, S. A variational approach to the theory of the elastic behaviour of multiphase materials. *Journal of the Mechanics and Physics of Solids 11*, 2 (1963), 127–140.

[47] Hill, R. Elastic properties of reinforced solids: some theoretical principles. *Journal of the Mechanics and Physics of Solids 11*, 5 (1963), 357–372.

[48] Hill, R. A self-consistent mechanics of composite materials. *Journal of the Mechanics and Physics of Solids 13*, 4 (1965), 213–222.

[49] Jakus, A. E., Secor, E. B., Rutz, A. L., Jordan, S. W., Hersam, M. C., and Shah, R. N. Three-dimensional printing of high-content graphene scaffolds for electronic and biomedical applications. *ACS nano 9*, 4 (2015), 4636–4648.

[50] Jean, A., Jeulin, D., Forest, S., Cantournet, S., and NGUYEN, F. A multiscale microstructure model of carbon black distribution in rubber. *Journal of microscopy 241*, 3 (2011), 243–260.

[51] Jiang, Z., Chen, W., and Burkhart, C. Efficient 3d porous microstructure reconstruction via gaussian random field and hybrid optimization. *Journal of microscopy 252*, 2 (2013), 135–148.

[52] Jirasek, M. Nonlocal models for damage and fracture: comparison of approaches. *International Journal of Solids and Structures 35*, 31 (1998), 4133–4145.

[53] Jolliffe, I. *Principal component analysis*. Wiley Online Library, 2002.

[54] Kabel, M., Böhlke, T., and Schneider, M. Efficient fixed point and Newton???Krylov solvers for FFT-based homogenization of elasticity at large deformations. *Computational Mechanics 54*, 6 (2014), 1497–1514.

[55] Karhunen, K. *Zur spektraltheorie stochastischer prozesse*. Suomalainen tiedeakatemia, 1946.

[56] Kerfriden, P., Goury, O., Rabczuk, T., and Bordas, S. P.-A. A partitioned model order reduction approach to rationalise computational expenses in nonlinear fracture mechanics. *Computer methods in applied mechanics and engineering 256* (2013), 169–188.

[57] Kouznetsova, V., Geers, M. G. D., and Brekelmans, W. A. M. Multi-scale constitutive modelling of heterogeneous materials with a gradient-enhanced computational homogenization scheme. *International Journal for Numerical Methods in Engineering 54*, 8 (2002), 1235–1260.

[58] Kröner, E. *Statistical continuum mechanics*. No. 92. Springer, 1972.

[59] Laiarinandrasana, L., Jean, A., Jeulin, D., and Forest, S. Modelling the effects of various contents of fillers on the relaxation rate of elastomers. *Materials & Design 33* (2012), 75–82.

[60] Le, B., Yvonnet, J., and He, Q.-C. Computational homogenization of nonlinear elastic materials using neural networks. *International Journal for Numerical Methods in Engineering 104*, 12 (2015), 1061–1084.

[61] Lebensohn, R. A., Kanjarla, A. K., and Eisenlohr, P. An elasto-viscoplastic formulation based on fast fourier transforms for the prediction of micromechanical fields in polycrystalline materials. *International Journal of Plasticity 32* (2012), 59–69.

[62] Lee, J., and Mal, A. A Volume Integral Equation Technique for Multiple Inclusion and Crack Interaction Problems. *Journal of Applied Mechanics 64*, March (1997), 23–31.

[63] Lee, J., and Mal, A. K. A volume integral equation technique for multiple scattering problems in elastodynamics. *Applied Mathematics and Computation 67*, 1-3 (1995), 135–159.

[64] Li, W., Jaroszewski, L., and Godzik, A. Clustering of highly homologous sequences to reduce the size of large protein databases. *Bioinformatics 17*, 3 (2001), 282–283.

[65] Li, Y., Kröger, M., and Liu, W. K. Nanoparticle effect on the dynamics of polymer chains and their entanglement network. *Physical review letters 109*, 11 (2012), 118001.

[66] Li, Y., Liu, Z., Jia, Z., Liu, W. K., Aldousari, S. M., Hedia, H. S., and Asiri, S. A. Modular-based multiscale modeling on viscoelasticity of polymer nanocomposites. *Computational Mechanics* (2017), 1–15.

[67] Lippmann, B. A., and Schwinger, J. Variational principles for scattering processes. i. *Phys. Rev. 79* (Aug 1950), 469–480.

[68] Liu, R., Kumar, A., Chen, Z., Agrawal, A., Sundararaghavan, V., and Choudhary, A. A predictive machine learning approach for microstructure optimization and materials design. *Scientific reports 5* (2015).

[69] Liu, Y., Greene, M. S., Chen, W., Dikin, D. A., and Liu, W. K. Computational microstructure characterization and reconstruction for stochastic multiscale material design. *Computer-Aided Design 45*, 1 (2013), 65–76.

[70] Liu, Z., Bessa, M., and Liu, W. K. Self-consistent clustering analysis: An efficient multi-scale scheme for inelastic heterogeneous materials. *Computer Methods in Applied Mechanics and Engineering 306* (2016), 319–341.

[71] Liu, Z., Moore, J. A., Aldousari, S. M., Hedia, H. S., Asiri, S. A., and Liu, W. K. A statistical descriptor based volume-integral micromechanics model of heterogeneous material with arbitrary inclusion shape. *Computational Mechanics* (2015), 1–19.

[72] Liu, Z., Moore, J. A., and Liu, W. K. An extended micromechanics method for probing interphase properties in polymer nanocomposites. *Journal of the Mechanics and Physics of Solids* (2016).

[73] Lloyd, S. P. Least squares quantization in pcm. *Information Theory, IEEE Transactions on 28*, 2 (1982), 129–137.

[74] Loève, M. *Probability Theory; Foundations, Random Sequences*. New York: D. Van Nostrand Company, 1955.

[75] MacKay, D. J. *Information theory, inference and learning algorithms*. Cambridge university press, 2003.

[76] MacQueen, J., et al. Some methods for classification and analysis of multivariate observations. 281–297.

[77] McGinty, R. D. *Multiscale Representation of Polycrystalline Inelasticity*. PhD thesis, Geogia Tech, 2001.

[78] McVeigh, C., and Liu, W. K. Linking microstructure and properties through a predictive multiresolution continuum. *Computer Methods in Applied Mechanics and Engineering 197*, 41-42 (2008), 3268–3290.

[79] McVeigh, C., and Liu, W. K. Linking microstructure and properties through a predictive multiresolution continuum. *Computer Methods in Applied Mechanics and Engineering 197*, 41 (2008), 3268–3290.

[80] McVeigh, C., Vernerey, F., Liu, W. K., and Brinson, L. C. Multiresolution analysis for material design. *Computer Methods in Applied Mechanics and Engineering 195*, 37 (2006), 5053–5076.

[81] Mediavilla Varas, J. *Continuous and discontinuous modelling of ductile fracture*. PhD thesis, Eindhoven University of Technology, 2005.

[82] Melro, A. R., Camanho, P. P., Andrade Pires, F. M., and Pinho, S. T. Micromechanical analysis of polymer composites reinforced by unidirectional fibres: Part I-Constitutive modelling. *International Journal of Solids and Structures 50*, 11-12 (2013), 1897–1905.

[83] Melro, A. R., Camanho, P. P., and Pinho, S. T. Generation of random distribution of fibres in long-fibre reinforced composites. *Composites Science and Technology 68*, 9 (2008), 2092–2102.

[84] Meza, L. R., Das, S., and Greer, J. R. Strong, lightweight, and recoverable three-dimensional ceramic nanolattices. *Science 345*, 6202 (2014), 1322–1326.

[85] Meza, L. R., Zelhofer, A. J., Clarke, N., Mateos, A. J., Kochmann, D. M., and Greer, J. R. Resilient 3D hierarchical architected metamaterials. *Proceedings of the National Academy of Sciences of the United States of America 112*, 37 (2015), 11502–7.

[86] Michel, J., and Suquet, P. Nonuniform transformation field analysis. *International Journal of Solids and Structures 40*, 25 (2003), 6937 – 6955. Special issue in Honor of George J. Dvorak.

[87] Miehe, C. *IUTAM Symposium on Computational Mechanics of Solid Materials at Large Strains: Proceedings of the IUTAM Symposium held in Stuttgart, Germany, 20–24 August 2001*, vol. 108. Springer Science & Business Media, 2013.

[88] Miehe, C., Hofacker, M., Schaenzel, L.-M., and Aldakheel, F. Phase field modeling of fracture in multi-physics problems. part ii. coupled brittle-to-ductile failure criteria and crack propagation in thermo-elastic–plastic solids. *Computer Methods in Applied Mechanics and Engineering 294* (2015), 486–522.

[89] Miehe, C., Welschinger, F., and Hofacker, M. Thermodynamically consistent phase-field models of fracture: Variational principles and multi-field fe implementations. *International Journal for Numerical Methods in Engineering 83*, 10 (2010), 1273–1311.

[90] Mindlin, R. D. Micro-structure in linear elasticity. *Archive for Rational Mechanics and Analysis 16*, 1 (1964), 51–78.

[91] Mochalin, V. N., Shenderova, O., Ho, D., and Gogotsi, Y. The properties and applications of nanodiamonds. *Nature nanotechnology 7*, 1 (2012), 11–23.

[92] Mori, T., and Tanaka, K. Average stress in matrix and average elastic energy of materials with misfitting inclusions. *Acta metallurgica 21*, 5 (1973), 571–574.

[93] Moulinec, H., and Suquet, P. A numerical method for computing the overall response of nonlinear composites with complex microstructure. *Computer methods in applied mechanics and engineering 157*, 1 (1998), 69–94.

[94] Moulinec, H., and Suquet, P. Comparison of fft-based methods for computing the response of composites with highly contrasted mechanical properties. *Physica B: Condensed Matter 338*, 1 (2003), 58–60.

[95] Mura, T. *Micromechanics of defects in solids*, vol. 3. Springer Science & Business Media, 1987.

[96] Nemat-Nasser, S., and Hori, M. *Micromechanics: overall properties of heterogeneous materials*. Elsevier, 2013.

[97] Paley, M., and Aboudi, J. Micromechanical analysis of composites by the generalized cells model. *Mechanics of Materials 14*, 2 (1992), 127–139.

[98] Pandolfi, A., and Ortiz, M. An eigenerosion approach to brittle fracture. *International Journal for Numerical Methods in Engineering 92*, 8 (2012), 694–714.

[99] Peerlings, R., De Borst, R., Brekelmans, W., and Geers, M. Gradient-enhanced damage modelling of concrete fracture. *Mechanics of Cohesive-frictional Materials 3*, 4 (1998), 323–342.

[100] Peng, X., Tang, S., Hu, N., and Han, J. Determination of the Eshelby tensor in mean-field schemes for evaluation of mechanical properties of elastoplastic composites. *International Journal of Plasticity 76*, April (2016), 147–165.

[101] Qiao, R., and Brinson, L. C. Simulation of interphase percolation and gradients in polymer nanocomposites. *Composites Science and Technology 69*, 3 (2009), 491–499.

[102] Ramanathan, T., Abdala, A., Stankovich, S., Dikin, D., Herrera-Alonso, M., Piner, R., Adamson, D., Schniepp, H., Chen, X., Ruoff, R., et al. Functionalized graphene sheets for polymer nanocomposites. *Nature nanotechnology 3*, 6 (2008), 327–331.

[103] Roeder, C. W., and Stanton, J. F. Elastomeric bearings: state-of-the-art. *Journal of Structural Engineering 109*, 12 (1983), 2853–2871.

[104] Rousseeuw, P. J. Silhouettes: a graphical aid to the interpretation and validation of cluster analysis. *Journal of computational and applied mathematics 20* (1987), 53–65.

[105] Roussette, S., Michel, J.-C., and Suquet, P. Nonuniform transformation field analysis of elastic–viscoplastic composites. *Composites Science and Technology 69*, 1 (2009), 22–27.

[106] Saad, Y., and Schultz, M. H. Gmres: A generalized minimal residual algorithm for solving nonsymmetric linear systems. *SIAM Journal on scientific and statistical computing 7*, 3 (1986), 856–869.

[107] Schmidt, M., and Lipson, H. Distilling free-form natural laws from experimental data. *science 324*, 5923 (2009), 81–85.

[108] Sundararaghavan, V., and Zabaras, N. Classification and reconstruction of three-dimensional microstructures using support vector machines. *Computational Materials Science 32*, 2 (2005), 223–239.

[109] Tian, R., Chan, S., Tang, S., Kopacz, A. M., Wang, J.-S., Jou, H.-J., Siad, L., Lindgren, L.-E., Olson, G. B., and Liu, W. K. A multiresolution continuum simulation of the ductile fracture process. *Journal of the Mechanics and Physics of Solids 58*, 10 (2010), 1681–1700.

[110] Torquato, S. *Random heterogeneous materials: microstructure and macroscopic properties*, vol. 16. Springer Science & Business Media, 2013.

[111] Toupin, R. A. Theories of elasticity with couple-stress. *Archive for Rational Mechanics and Analysis 17*, 2 (1964), 85–112.

[112] Tran, T.-H., Monchiet, V., and Bonnet, G. A micromechanics-based approach for the derivation of constitutive elastic coefficients of strain-gradient media. *International Journal of Solids and Structures 49*, 5 (2012), 783–792.

[113] Vernerey, F., Liu, W. K., and Moran, B. Multi-scale micromorphic theory for hierarchical materials. *Journal of the Mechanics and Physics of Solids 55*, 12 (2007), 2603–2651.

[114] Vernerey, F., Liu, W. K., and Moran, B. Multi-scale micromorphic theory for hierarchical materials. *Journal of the Mechanics and Physics of Solids 55*, 12 (2007), 2603–2651.

[115] Vernerey, F. J., Liu, W. K., Moran, B., and Olson, G. A micromorphic model for the multiple scale failure of heterogeneous materials. *Journal of the Mechanics and Physics of Solids 56*, 4 (2008), 1320–1347.

[116] Vondejc, J., Zeman, J., and Marek, I. An FFT-based Galerkin method for homogenization of periodic media. *Computers and Mathematics with Applications 68*, 3 (2014), 156–173.

[117] Vu-Bac, N., Bessa, M., Rabczuk, T., and Liu, W. A multiscale model for the quasi-static thermo-plastic behavior of highly cross-linked glassy polymers. *Submitted to publication* (2015).

[118] Wang, M.-J. Effect of polymer-filler and filler-filler interactions on dynamic properties of filled vulcanizates. *Rubber Chemistry and Technology 71*, 3 (1998), 520–589.

[119] Watcharotone, S., Wood, C. D., Friedrich, R., Chen, X., Qiao, R., Putz, K., and Brinson, L. C. Interfacial and substrate effects on local elastic properties of polymers using coupled experiments and modeling of nanoindentation. *Advanced Engineering Materials 13*, 5 (2011), 400–404.

[120] Wei, X., Ford, M., Soler-Crespo, R. A., and Espinosa, H. D. A new monte carlo model for predicting the mechanical properties of fiber yarns. *Journal of the Mechanics and Physics of Solids 84* (2015), 325–335.

[121] Werner, B. T., and Daniel, I. M. Characterization and modeling of polymeric matrix under multi-axial static and dynamic loading. *Composites Science and Technology 102* (2014), 113–119.

[122] Witten, I. H., and Frank, E. *Data Mining: Practical machine learning tools and techniques*. Morgan Kaufmann, 2005.

[123] Xu, H., Dikin, D. A., Burkhart, C., and Chen, W. Descriptor-based methodology for statistical characterization and 3d reconstruction of microstructural materials. *Computational Materials Science 85* (2014), 206–216.

[124] Xu, H., Liu, R., Choudhary, A., and Chen, W. A machine learning-based design representation method for designing heterogeneous microstructures. *Journal of Mechanical Design 137*, 5 (2015), 051403.

[125] Yeong, C., and Torquato, S. Reconstructing random media. ii. three-dimensional media from two-dimensional cuts. *Physical Review E 58*, 1 (1998), 224.

[126] Yvonnet, J., and He, Q.-C. The reduced model multiscale method (r3m) for the non-linear homogenization of hyperelastic media at finite strains. *Journal of Computational Physics 223*, 1 (2007), 341–368.

[127] Yvonnet, J., Monteiro, E., and He, Q.-C. Computational homogenization method and reduced database model for hyperelastic heterogeneous structures. *International Journal for Multiscale Computational Engineering 11*, 3 (2013).

APPENDIX A

Basics of Boolean-Poisson model

In stochastic geometry, the Boolean-Poisson model (or Boolean model) is a simple and commonly used method to generate overlapping geometries [**22**]. In the current work, all the N inclusions are identical and chosen to be spherical in 3-D (or circular in 2-D) with same radius R^c and volume V^c. The center of each inclusion is randomly and independently inserted into the RVE domain Ω obeying a uniform distribution, and the resulting union of the overlapping inclusion is a realization of the Boolean-Poisson model. The procedure also refers to a stationary Poisson point process in Ω with a rate λ, which is defined as

$$\lambda = N/|\Omega|. \tag{A.1}$$

The number of inclusion centers K at any point in Ω is a Poisson random variable whose probability function is

$$p(K = k) = \frac{\lambda^k}{k!} e^{-\lambda}, \tag{A.2}$$

where $k!$ denotes the k factorial. The expected value of K is equal to the rate λ.

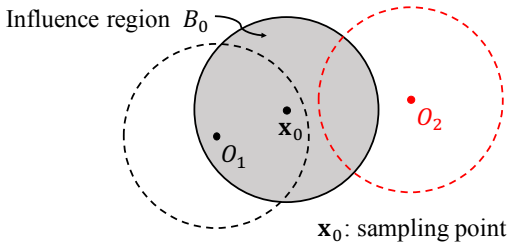

Figure A.1. Illustration of the influence region B_0 centering at the sampling point $\mathbf{x}_0$.

Due to the simplicity of the Boolean-Poisson model, one can define ξ_i as the state where there are i inclusions overlapping at a sampling point $\mathbf{x}_0$,

$$\sum_{r=1}^{N} \chi_r(\mathbf{x}_0) = i \quad \text{at state } \xi_i. \tag{A.3}$$

In order to calculate the probability function of ξ_i, we will first draw a sphere with radius R^c centering at $\mathbf{x}_0$, called the influence region B_0. As we can see from Figure A.1, if the center of any inclusion is inserted into the influence region, the inclusion will contribute to the overlapping at $\mathbf{x}_0$. Since the random processes at different points in the Boolean-Poisson model are independent from each other, the total number of inclusion whose centers are in the influence region B_0 also follows a Poisson distribution with a rate λV^c. Finally, the probability function of the overlapping states is obtained:

$$p(\xi_i) = \frac{(\lambda V^c)^i}{i!} e^{-\lambda V^c}. \tag{A.4}$$

Another important quantity in the Boolean-Poisson model is the volume fraction of the inclusion phase f_c, defined in Eq. (3.3). A phase density function $\rho(\mathbf{x}) \in [0, 1]$ is introduced for the analysis. The value of $\rho(\mathbf{x})$ is equal to 0 if $\mathbf{x}$ is in the matrix phase, or 1 if $\mathbf{x}$ is in the inclusion phase. Since the phase density function needs be kept at 1 in the inclusion phase after overlapping (analogous to weighted-mean overlapping condition for the relative stiffness tensor), the phase density function in the r-the inclusion $\rho^r(x)$ can be determined by

$$\left(\sum_{s=1}^{N} \chi_s(\mathbf{x}) \right) \rho^r(\mathbf{x}) = 1 \quad \text{in } \Omega^r. \tag{A.5}$$

As in the general scheme discussed in Section 3.2, a *test* inclusion is inserted at the sampling point $\mathbf{x}_0$ in the Boolean-Poisson model. Based on equation (A.3), the expected value of the phase density function $\langle \rho^c \rangle$ in the *test* inclusion can be derived as

$$\langle \rho^c \rangle = \sum_{\xi_i \in \Xi} p(\xi_i) \rho^c_{(\xi_i)} = \sum_{i=0}^{\infty} \frac{1}{i+1} p(\xi_i) = (\lambda V^c)^{-1} (1 - e^{-\lambda V^c}) \tag{A.6}$$

Then, the volume fractions of the inclusion phase and matrix phase are

$$f_c = \frac{N}{|\Omega|}\langle \rho^c \rangle V^c = 1 - e^{-\lambda V^c} \quad \text{and } f_m = 1 - f_c = e^{-\lambda V^c}. \tag{A.7}$$

These values are consistent with the theoretical volume fractions obtained through other methods for the Boolean-Poisson's model [**22**], which indicates that the scheme of introducing a *test* inclusion is capable of capturing essential features of overlapping.

APPENDIX B

Eshelby's tensor of spherical inclusion

Many micromechanics methods dates back to the work of Eshelby (1957), which gave the exact solution of the stress or strain field for one ellipsoidal inclusion embedded in an infinite matrix. It was found that in a isotropic linear elastic medium (or reference material in the Lippmann-Schwinger equation), if the imposed eigenstrain $\boldsymbol{\varepsilon}^*$ is homogeneous inside a ellipsoidal inclusion domain Ω_r in 3D, the resulting strain $\boldsymbol{\varepsilon}^r$ upon equilibrium in Ω_r is also homogeneous. The same statement also holds for a 2D elliptic inclusion. The fourth-order tensor projecting $\boldsymbol{\varepsilon}^*$ to $\boldsymbol{\varepsilon}^r$ is defined as the Eshelby's tensor $\mathbf{S}^0$, named after J.D. Eshelby (1916-1981),

$$\boldsymbol{\varepsilon}^r = \mathbf{S}^0 : \boldsymbol{\varepsilon}^*. \tag{B.1}$$

As discussed in Chapter 2, the concept of eigenstrain is similar to that of the polarization stress in the Lippmann-Schwinger equation, in fact, we have

$$\mathbf{p} = \mathbf{C}^0 : \boldsymbol{\varepsilon}^*. \tag{B.2}$$

Based on the Lippmann Schwinger equation (2.4) and Eq. (B.2), the following relation can be derived for the reference material,

$$\left[\int_{\Omega_r} \boldsymbol{\Phi}^0(\mathbf{x}, \mathbf{x}')d\mathbf{x}'\right] : \mathbf{C}^0 = \mathbf{S}^0, \tag{B.3}$$

Which indicates that the integral of the Green's function $\boldsymbol{\Phi}^0(\mathbf{x}, \mathbf{x}')$ inside a elliptical domain results in a constant tensor.

The derivation of the Eshelby tensor in isotropic materials can be found in [**32, 95**]. The Eshelbys tensor for an ellipsoidal inclusion can be expressed in terms of elliptic

integrals. However, for a spherical inclusion in 3D, it takes the following compact form,

$$S^0_{ijkl} = \frac{5\nu^0 - 1}{15(1-\nu^0)}\delta_{ij}\delta_{kl} + \frac{4 - 5\nu^0}{15(1-\nu^0)}\left(\delta_{ik}\delta_{jl} + \delta_{il}\delta_{jk}\right). \tag{B.4}$$

Moreover, the Eshelby's tensor for a circular inclusion in 2D can be expressed as

$$S^0_{ijkl} = \frac{4\nu^0 - 1}{8(1-\nu^0)}\delta_{ij}\delta_{kl} + \frac{3 - 4\nu^0}{8(1-\nu^0)}\left(\delta_{ik}\delta_{jl} + \delta_{il}\delta_{jk}\right). \tag{B.5}$$

Note that the Eshelby's tensors in both 2D and 3D only depend on the Poisson's ratio ν^0 of the reference material.

APPENDIX C

Strain expectation for two-phase inclusions

By taking all overlapping states shown in Figure 3.6 into account and using equation 3.53 of volume fraction f_{np} and f_{ip}, one can calculate the expected values of the strain $\langle \boldsymbol{\varepsilon}_{np}^{\text{test}} \rangle$ in the nanoparticle phase and $\langle \boldsymbol{\varepsilon}_{ip}^{\text{test}} \rangle$ in the interphase of the test inclusion as

$$\langle \boldsymbol{\varepsilon}_{np}^{\text{test}} \rangle = (1 - f_{np} - f_{ip}) \mathbf{T}_{(\xi_0)}^{np} : \bar{\boldsymbol{\varepsilon}}^m + f_{ip} \mathbf{T}_{(\xi_i)}^{np} : \mathbf{A}^{ip} : \bar{\boldsymbol{\varepsilon}} + \left(\frac{f_{np}}{\lambda V^{np}} - e^{\lambda V^{np}} \right) \mathbf{A}^{np} : \bar{\boldsymbol{\varepsilon}} \tag{C.1}$$

and

$$\langle \boldsymbol{\varepsilon}_{ip}^{\text{test}} \rangle = (1 - f_{np} - f_{ip}) \mathbf{T}_{(\xi_0)}^{ip} : \bar{\boldsymbol{\varepsilon}}^m + \left(\frac{f_{ip}}{\lambda V^{ip}} - e^{\lambda (V^{np} + V^{ip})} \right) : \mathbf{A}^{ip} : \bar{\boldsymbol{\varepsilon}}, \tag{C.2}$$

where λ is the rate of the stationary Poisson point process in the Boolean-Poisson model (see Appendix A). Also, V^{np} and V^{ip} denote the volumes of the nanoparticle phase and the interphase in each inclusion. The concentration tensors $\mathbf{T}$ in the *test* inclusion are

$$\mathbf{T}_{(\xi_0)}^{np} = \left[\mathbf{I} + \mathbf{S}^0 : (\mathbf{C}^0)^{-1} : (\mathbf{C}^{np} - \mathbf{C}^0) \right]^{-1}, \quad \mathbf{T}_{(\xi_i)}^{np} = \left[\mathbf{I} + \mathbf{S}^{ip} : (\mathbf{C}^{ip})^{-1} : (\mathbf{C}^{np} - \mathbf{C}^{ip}) \right]^{-1} \tag{C.3}$$

and

$$\mathbf{T}_{(\xi_0)}^{ip} = \left[\mathbf{I} + \mathbf{S}^0 : (\mathbf{C}^0)^{-1} : (\mathbf{C}^{ip} - \mathbf{C}^0) \right]^{-1}. \tag{C.4}$$

The strain concentration tensors $\mathbf{A}$ of the nanoparticle and interphase materials are related to the properties of the effective medium,

$$\mathbf{A}^{np} = \left[\mathbf{I} + \bar{\mathbf{S}} : (\bar{\mathbf{C}}^{-1} : (\mathbf{C}^{np} - \bar{\mathbf{C}}) \right]^{-1} \quad \text{and} \quad \mathbf{A}^{ip} = \left[\mathbf{I} + \bar{\mathbf{S}} : (\bar{\mathbf{C}}^{-1} : (\mathbf{C}^{ip} - \bar{\mathbf{C}}) \right]^{-1}. \tag{C.5}$$

According to the consistent equation (3.54), the average strain in the matrix can be written as

$$(1 - f_{np} - f_{ip})\bar{\boldsymbol{\varepsilon}}^m = \bar{\boldsymbol{\varepsilon}} - \lambda \left(V^{np} \langle \boldsymbol{\varepsilon}_{np}^{\text{test}} \rangle + V^{ip} \langle \boldsymbol{\varepsilon}_{ip}^{\text{test}} \rangle \right), \tag{C.6}$$

By substituting Eq. (C.1) into (C.2) and (C.6) and rearranging the fomulation, the system of equations is obtained for solving $\langle \boldsymbol{\varepsilon}_{np}^{\text{test}} \rangle$ and $\langle \boldsymbol{\varepsilon}_{ip}^{\text{test}} \rangle$,

$$\begin{aligned} &\begin{bmatrix} \mathbf{I} + \lambda V^{np} \mathbf{T}_{(\xi_0)}^{np} & \lambda V^{ip} \mathbf{T}_{(\xi_0)}^{np} \\ \lambda V^{np} \mathbf{T}_{(\xi_0)}^{ip} & \mathbf{I} + \lambda V^{ip} \mathbf{T}_{(\xi_0)}^{ip} \end{bmatrix} \begin{bmatrix} \langle \boldsymbol{\varepsilon}_{np}^{\text{test}} \rangle \\ \langle \boldsymbol{\varepsilon}_{ip}^{\text{test}} \rangle \end{bmatrix} \\ &= \begin{bmatrix} \mathbf{T}_{(\xi_0)}^{np} + f_{ip} \mathbf{T}_{(\xi_i)}^{np} : \mathbf{A}^{ip} + \left(\dfrac{f_{np}}{\lambda V^{np}} - e^{\lambda V^{np}} \right) \mathbf{A}^{np} \\ \mathbf{T}_{(\xi_0)}^{ip} + \left(\dfrac{f_{ip}}{\lambda V^{ip}} - e^{\lambda (V^{np} + V^{ip})} \right) : \mathbf{A}^{ip} \end{bmatrix} \bar{\boldsymbol{\varepsilon}} \end{aligned} \tag{C.7}$$

Finally, the expected values of strain in the *test* inclusioin can be solved as a function of the average strain $\bar{\boldsymbol{\varepsilon}}$ based on Eq. (C.7),

$$\langle \boldsymbol{\varepsilon}_{np}^{\text{test}} \rangle = \langle \mathbf{A}^{np} \rangle : \bar{\boldsymbol{\varepsilon}} \quad \text{and} \quad \langle \boldsymbol{\varepsilon}_{ip}^{\text{test}} \rangle = \langle \mathbf{A}^{ip} \rangle : \bar{\boldsymbol{\varepsilon}} \tag{C.8}$$

APPENDIX D

Clustering of the strain concentration tensor

After computing the strain concentration tensor in the offline stage, the next step is to perform the domain decomposition by clustering similar data points into groups. Clustering methods have been widely applied to different fields, from pattern recognition and image segmentation to bioinformatics [**4, 64**]. Recently, a large spectrum of clustering algorithms has been developed, such as hierarchical clustering, k-means clustering and distribution-based clustering [**122**]. In this work, a particular kind of centroid-based clustering named k-means clustering [**76**] is applied to compress the data.

Mathematically, given a set of strain concentration tensors the objective of k-means clustering is to minimize the within-cluster least square sum for the k sets $\mathbf{S} = \{S^1, ..., S^k\}$ to obtain the shape of the clusters:

$$\mathbf{S} = \underset{\mathbf{S}'}{\operatorname{argmin}} \sum_{J=1}^{k} \sum_{n \in S^J} ||\mathbf{A}_n - \bar{\mathbf{A}}_J||^2, \tag{D.1}$$

where $\mathbf{A}_n$ is the strain concentration tensor of the n-th data point, and $\bar{\mathbf{A}}_J$ is the mean of all the strain concentration tensors at the points within the cluster S_J. The above norm is defined as usual, e.g. for a general second-order matrix $\mathbf{Z}$ of dimension $m \times m$

$$||\mathbf{Z}|| = \sqrt{\sum_{i=1}^{m} \sum_{j=1}^{m} z_{ij}^2} = \sqrt{\operatorname{trace}(\mathbf{Z}^T \mathbf{Z})}, \tag{D.2}$$

and is called the Frobenius norm of matrix $\mathbf{Z}$. The standard algorithm (Lloyd's algorithm) [**73**] is used to solve the k-means clustering problem which is essentially an optimization process of minimizing the sum in Eq. (D.1).

At the initialization step, k data points are randomly selected from the data set and served as the initial means (Forgy method [**38**]). Then the algorithm iterates between the following two steps,

(1) Assignment step: Each data point is assigned to the cluster whose mean is nearest to the data point. In other words, within the t-th iteration, $\forall\{\mathbf{A}_n\} \in S_I^{(t)}$, one have

$$||\{\mathbf{A}_n\} - \bar{\mathbf{A}}_I^{(t)}||^2 \leqslant ||\{\mathbf{A}_n\} - \bar{\mathbf{A}}_J^{(t)}||^2 \quad \forall J,\ J \neq I \tag{D.3}$$

(2) Update step: The mean values of the data points in the new cluster are recalculated for iteration $t+1$,

$$\bar{\mathbf{A}}_I^{(t)} = \frac{1}{N_I^{(t)}} \sum_{\{\mathbf{A}_n\} \in S_I^{(t)}} \{\mathbf{A}_n\} \tag{D.4}$$

where $N_i^{(t)}$ is the number of data points in cluster $S_I^{(t)}$.

When the assignment of data points no longer changes, the algorithm is said to converge to a local optimum. Finally, it should be noted that other clustering methods can also be applied for this problem, such as the density-based spatial clustering of applications with noise (DBSCAN) method [**33**].

Mathematically, the "Silhouette Index" [**104**] can be used to measure the quality of clustering; however, this may not be sufficient when considering the predictions of the mechanical behavior. Typically, a larger number of clusters (larger k) used in the offline stage leads to more accurate predictions in the online stage since more information was stored, but the number of degrees of freedom increases correspondingly. The computational cost associated with this increase is discussed in later sections. As a result, the choice for the number of clusters should keep a balance between the compression ratio of the data set and the accuracy of the prediction.

APPENDIX E

Newton's iteration in the SCA online stage

In the implicit scheme, the residual $\{\mathbf{r}\} = \{\mathbf{r}^1; ...; \mathbf{r}^k; \mathbf{r}^{k+1}\}$ is linearized with respect to $\{\Delta\boldsymbol{\varepsilon}\}$. Dropping terms of higher order than linear gives

$$\{\mathbf{r}\} + \{\mathbf{M}\}\{d\boldsymbol{\varepsilon}\} = \mathbf{0} \quad \text{with } \{\mathbf{M}\} = \frac{\partial\{\mathbf{r}\}}{\partial\{\Delta\boldsymbol{\varepsilon}\}}, \tag{E.1}$$

where $\{\mathbf{M}\}$ is called the system Jacobian matrix. For $I, J = 1, 2, ..., k$, we have

$$\mathbf{M}^{IJ} = \delta_{IJ}\mathbf{I} + \mathbf{D}^{IJ} : \left(\mathbf{C}^J_{alg} - \mathbf{C}^0\right) \quad \text{and} \quad \mathbf{M}^{I(k+1)} = -\mathbf{I}, \tag{E.2}$$

where δ_{IJ} is the Kronecker delta in terms of indices I and J, and $\mathbf{I}$ is the fourth-order identity tensor. $\mathbf{C}^J_{alg}$ is the so-called algorithmic stiffness tensor of the material in the J-th cluster and is an output of the local constitutive law for the current strain increment in that cluster $\Delta\boldsymbol{\varepsilon}^J_n$,

$$\mathbf{C}^J_{alg} = \frac{\partial\Delta\boldsymbol{\sigma}^J}{\partial\Delta\boldsymbol{\varepsilon}^J}. \tag{E.3}$$

Although local material damage is decoupled with the equilibrium condition to avoid material instability in the current work, it is still possible to introduce the damage into the local constitutive law and $\mathbf{C}^J_{alg}$ can be written as

$$\mathbf{C}^J_{alg} = (1 - d^J)\frac{\partial\Delta\boldsymbol{\sigma}^J_{ud}}{\partial\Delta\boldsymbol{\varepsilon}^J}, \tag{E.4}$$

where $\partial\Delta\boldsymbol{\sigma}^J_{ud}/\partial\Delta\boldsymbol{\varepsilon}^J$ represents the algorithmic stiffness tensor of the undamaged pure elasto-plastic material. Under the macro-strain constraint, the remaining components in the system Jacobian matrix are

$$\mathbf{M}^{(k+1)I} = c^I\mathbf{I} \quad \text{and} \quad \mathbf{M}^{(k+1)(k+1)} = \mathbf{0}. \tag{E.5}$$

For macro-stress constraint, we have

$$\mathbf{M}^{(k+1)I} = c^I \mathbf{C}^I_{alg} \quad \text{and} \quad \mathbf{M}^{(k+1)(k+1)} = \mathbf{0}. \tag{E.6}$$

Finally, the correction of the incremental strain can be expressed as

$$\{d\boldsymbol{\varepsilon}\} = -\{\mathbf{M}\}^{-1}\{\mathbf{r}\}. \tag{E.7}$$

Based on the updated incremental strain, one can then use the constitutive relationship in each cluster to compute the new incremental stress $\{\Delta\boldsymbol{\sigma}\} = \{\Delta\boldsymbol{\sigma}^1; ...; \Delta\boldsymbol{\sigma}^k\}$. If $\Delta\boldsymbol{\sigma}^I$ and $\Delta\boldsymbol{\varepsilon}^I$ have a nonlinear relation, several iterations are needed so that the residual $\{\mathbf{r}\}$ can vanish.

Vita

Zeliang Liu received the Bachelor of Engineering degree in Micro-Electro-Mechanical System (MEMS) Engineering from Tsinghua University in 2012. He immediately entered the Theoretical and Applied Mechanics (TAM) program at Northwestern University under the supervision of Prof. Wing Kam Liu. His graduate research work has been recognized as a finalist of the Robert J. Melosh medal from the Duke University in 2017. Upon completion of his doctoral degree, he will work as a research scientist at the Livermore Software Technology Corporation (LSTC).

This dissertation was typeset with LaTeX[1] by the author.

[1] LaTeXis a document preparation system developed by Leslie Lamport as a special version of Donald Knuths TEX Program